UNIVERSITY OF GHANA

COLLEGE OF BASIC AND APPLIED SCIENCES

# COMPARATIVE ANALYSIS OF GEO-ELECTRIC ANOMALY DEFINITION USING THREE CONVENTIONAL ARRAYS: A NEAR SUBSURFACE INVESTIGATION IN THE UNIVERSITY OF GHANA, LEGON.

SAMPSON RENNER

(10284765)

A THESIS SUBMITTED TO THE DEPARTMENT OF EARTH SCIENCE, OF THE SCHOOL OF PHYSICAL AND MATHEMATICAL SCIENCE, COLLEGE OF BASIC AND APPLIED SCIENCES, UNIVERSITY OF GHANA, LEGON IN PARTIAL FULFILLMENT OF THE REQUIREMENT FOR THE AWARD OF A MASTER OF PHILOSOPHY IN GEOLOGY

July, 2015

# DECLARATION

This is to certify that this thesis is the result of research work undertaken by Renner Sampson towards the award of Master of Philosophy in Geology in the Department of Earth Science, University of Ghana.

Sign ……..... Date: ……..

SAMPSON RENNER

(Student)

Sign …… Date: ……..

Dr. THOMAS E.K. ARMAH

(Principal Supervisor)

Sign …… Date: ……..

Dr. ISAAC A. OPPONG

(Co-Supervisor)

# ABSTRACT

Complexity in the near subsurface affects resistivity distribution such that arrays can produce different representations of the same subsurface structure. Comparison and analysis have been presented for the performance of three conventional resistivity arrays -Wenner, Schlumberger, and dipole-dipole - with respect to their ability to resolve anomaly in the 'very' near subsurface. Assessment was on the definition of naturally-occurring anomaly - resistivity lows associated with borehole positions - in varying environment, and definition of artificial anomalies of fixed and undefined geometries - buried salt unit and leachate saturated zone – in a more laterally inhomogeneous setting of a dumpsite. This was with respect to the ability of the individual arrays to successfully resolve the lateral and vertical resistivity variation in the sub-environments and in the process, delineate the related anomaly. Maximum depth of investigation was about 5 m. Profile plots for the various arrays along the same traverse showed varying similarities with no two patterns being the same. The Wenner array performed best in imaging the buried salt unit followed by the Schlumberger array, which defined the unit better in the pseudo-section. The dipole-dipole array did not image the salt unit, in both the pseudo- and true resistivity section. The Wenner and Schlumberger arrays also showed better imaging of zones with undefined geometry and showed a high level of consistency in image and profile pattern similarities. The dipole-dipole array was for most part non-conformable. These discrepancies have been attributed collectively to the individual array sensitivity, configuration and geometric factor, and profiling/sampling technique. The plots and images showed that the measure and extent of similarity between the images and the profiles of the different arrays is dependent on the simplicity of the subsurface resistivity distribution and structure.

# ACKNOWLEDGEMENT

I would like to acknowledge the varying help and support provided by the following towards the successful completion of this research work. It is in no particular order.

- The entire community of the University of Ghana, Legon, for tolerating my use of campus as a study area.
- The Head, Professor P.M. Nude and the Department of Earth Science, University of Ghana, for providing the SARIS resistivity meter used for the work.
- My Supervisors, Dr. Thomas Armah and Dr. Isaac Oppong, for proposing the topic, providing technical support and equipment used in the field, and constructive criticism of the resulting script.
- Dr. Kippo and Mr. Inusah of Heisa Engineering for the information on drilled boreholes.
- The Geophysics team, Messrs Kofi Duku, Patrick Banahene, Emmanuel Haruna, Moses Mensah, Benjamin Aidoo, Opuni Antwi—Bosiako, Sampson Ebiasah, Michael Amoo and Miss Abigail Ayikwei for research and field assistance.
- Mr. Samuel Obeng, for timely encouragement.
- My family, for the unconditional support and prayers.
- And God, who helped us all.

# DEDICATION

To God, who gave me Mary Okyere.

# TABLE OF CONTENT

DECLARATION ..... i

ABSTRACT ..... ii

ACKNOWLEDGEMENT ..... iii

DEDICATION ..... iv

LIST OF FIGURES ..... vii

LIST OF APPENDIX ..... xi

CHAPTER ONE ..... 1

INTRODUCTION ..... 1

1.1 The Concept ..... 1

1.2 Background ..... 2

1.3 Objective ..... 3

1.4 Justification of objective ..... 4

1.5 Location, Physiography and Climate of Study Site ..... 4

1.6 Geology and Soil type of Study Site ..... 5

CHAPTER TWO ..... 7

LITERATURE REVIEW ..... 7

2.1 Versatility and Applications of the Resistivity Method ..... 7

2.3 Imaging Characteristics ..... 14

2.4 Sensitivity Analysis ..... 17

2.5 Isotropy/Anisotropy and Homogeneity/Heterogeneity ..... 19

CHAPTER THREE ..... 23

METHODOLOGY ..... 23

3.1 Theory and Principles ..... 23

3.2 Arrays ..... 26

3.3 Study Area and Anomaly selection ..... 28
3.3.1 Phase One ..... 28
3.3.2 Phase Two ..... 29
3.4 Instrumentation ..... 31
3.5 Survey design and Data acquisition ..... 31
3.5.1 Phase One ..... 31
3.5.2 Phase Two ..... 33
3.6 Data Reduction and Processing ..... 35
CHAPTER FOUR ..... 37
RESULTS AND DISCUSSION ..... 37
4.1 Borehole Sites ..... 37
4.1.1 REN-01 ..... 37
4.1.2 REN-02 ..... 40
4.1.2 REN-03 ..... 43
4.1.4 REN-04 ..... 45
4.1.5 REN-05 ..... 48
4.1.6 REN-06 ..... 51
4.1.7 REN-07 ..... 53
4.1.8 REN-08 ..... 56
4.1.9 REN-09 ..... 59
4.1.10 REN-10 ..... 61
4.1.12 REN-12 ..... 67
4.1.13 REN-13 ..... 69
4.1.14 REN-14 ..... 72
4.1.15 REN-15 ..... 75

4.2 Anisotropy ..... 79
4.3 Dumpsite Model Sections ..... 80
4.3.1 Traverse A ..... 81
4.3.2 Traverse B ..... 85
4.3.3 Buried Salt Unit ..... 89
CHAPTER FIVE ..... 100
CONCLUSION ..... 100
RECOMMENDATION ..... 102
REFERENCES ..... 104
APPENDIX A ..... 114
APPENDIX B ..... 115

## LIST OF FIGURES

Figure 1.1 Sketched geological map of some parts of Accra showing the study area (after Anokwa et al., 2005) ..... 6

Figure 2.1 Collinear electrode configuration and their geometric factors (after Stummer, 2003) ..... 15

Figure 2.2 Sketched diagram of a subsurface possessing both structural and compositional heterogeneity ..... 20

Figure 3.1 Distribution of current (arrows) and potential lines (solid lines) for two current electrodes at the surface with (a) homogeneous subsurface (b) inhomogeneous two-layered subsurface (after Herman, 2001) ..... 25

Figure 3.2 A conventional four electrode array set-up to measure subsurface resistivity (After Herman, 2001) ……..…….... 28

Figure 3.3 Map of study area showing location and distribution of survey points (boreholes and dumpsites)…….…….. 30

Figure 3.4 Dimension of arrays used in profiling ……..……..….. 32

Figure 3.5 Sketched diagram of the Dump site ……..….. 34

Figure 3.6 Cross section of trench ……..……..…… 34

Figure 3.7 Dimension of arrays used in profiles targeting buried salt unit …….…...…. 34

Figure 4.1.1a Wenner Array Profiles for REN-01 ……..…..... 38

Figure 4.1.1b Schlumberger Array Profiles for REN-01 …….……..... 38

Figure 4.1.1c Dipole-Dipole Array Profiles for REN-01 ……..…… 38

Figure 4.1.2a Wenner Array Profiles for REN-02 …….…… 41

Figure 4.1.2b Schlumberger Array Profiles for REN-02 ……..……....…… 41

Figure 4.1.2c Dipole-Dipole Array Profiles for REN-02 ……...……...…… 41

Figure 4.1.3a Wenner Array Profiles for REN- 03 ……..……..…… 44

Figure 4.1.3b Schlumberger Array Profiles for REN- 03……...……...…..…… 44

Figure 4.1.3c Dipole-Dipole Array Profiles for REN- 03 …….……..…….. 44

Figure 4.1.4a Wenner Array Profiles for REN-04 ……..……..…….…… 47

Figure 4.1.4b Schlumberger Array Profiles for REN-04 ……..… 47

Figure 4.1.4c Dipole-Dipole Array Profiles for REN-04 ...…...…… 47

Figure 4.1.5a Wenner Array Profiles for REN-05 ……..……..……..…… 49

Figure 4.1.5b Schlumberger Array Profiles for REN-05 ……..……..……..…..... 49

Figure 4.1.5c Dipole-Dipole Array Profiles for REN-05 …...……...…… 49

Figure 4.1.6a Wenner Array Profiles for REN-06 ……..…… 52

Figure 4.1.6b Schlumberger Array Profiles for REN-06 …...…… 52

Figure 4.1.6c Dipole-Dipole Array Profiles for REN-06 …...…… 52

Figure 4.1.7a Wenner Array Profiles for REN-07 ……... 54

Figure 4.1.7b Schlumberger Array Profiles for REN-07 ……..... 54

Figure 4.1.7c Dipole-Dipole Array Profiles for REN-07 ..……..……..…..... 54

Figure 4.1.8a Wenner Array Profiles for REN-08 …..……..……..…… 57

Figure 4.1.8b Schlumberger Array Profiles for REN-07 ……...…… 57

Figure 4.1.8c Dipole-Dipole Array Profiles for REN-08 ..…… 57

Figure 4.1.9a Wenner Array Profiles for REN-09 ……..……..…… 60

Figure 4.1.9b Schlumberger Array Profiles for REN-09 ……...…… 60

Figure 4.1.9c Dipole-Dipole Array Profiles for REN-09 ……...…..…… 60

Figure 4.1.10a Wenner Array Profiles for REN-10 ….…… 63

Figure 4.1.10b Schlumberger Array Profiles for REN-10 ..…….. 63

Figure 4.1.10c Dipole-Dipole Array Profiles for REN-10 ….…… 63

Figure 4.1.11a Wenner Array Profiles for REN-11 …...……..……..……..... 65

Figure 4.1.11b Schlumberger Array Profiles for REN-11...……..... 65

Figure 4.1.11c Dipole-Dipole Array Profiles for REN-11..…….. 65

Figure 4.1.12a Wenner Array Profiles for REN-12 ...…… 68

Figure 4.1.12b Schlumberger Array Profiles for REN-12 ...…….. 68

Figure 4.1.12c Dipole-Dipole Array Profiles for REN-12 ..……...… 68

Figure 4.1.13a Wenner Array Profiles for REN-13 …...……..……..…… 71

Figure 4.1.13b Schlumberger Array Profiles for REN-13 ...……...… 71

Figure 4.1.13c Dipole-Dipole Array Profiles for REN-13 ...…….…….…… 71

Figure 4.1.14a Wenner Array Profiles for REN-14 …...……..... 74

Figure 4.1.14b Schlumberger Array Profiles for REN-14 ..…….. 74

Figure 4.1.14c Dipole-Dipole Array Profiles for REN-14 ..…….. 74

Figure 4.1.15a Wenner Array Profiles for REN-15 ……..……..…… 76

Figure 4.1.15b Schlumberger Array Profiles for REN-15 ...…….. 76

Figure 4.1.15c Dipole-Dipole Array Profiles for REN-15 ..... 76

Figure 4.3.1a, b and c. Pseudo- and Inverse model sections for Traverse A ..... 82

Figure 4.3.2a, b and c. Pseudo- and Inverse model sections for Traverse B ..... 86

Figure 4.3.3 VES plots for to determine array dimensions corresponding to vertical position of buried salt ..... 90

Figure 4.3.4a, b, c Pseudo- and Inverse model sections targeting the buried salt unit ..... 92

## LIST OF APPENDICES

APPENDIX A: Coordinates of survey stations and Bearing of Traverses ..... 114

APPENDIX B: Anisotropy coefficients (λ) the for various arrays, across the borehole positions ..... 115

## LIST OF TABLE

Table 1.Table showing Anisotropy coefficients for $D_1$, $D_2$ and $D_3$ for Wenner, Schlumberger and dipole-dipole array ..... 80

# CHAPTER ONE

# INTRODUCTION

## 1.1 The Concept

Imaging the subsurface has been the focus and interest of Geophysics as a discipline. The main aim has been to produce a near accurate representation of the subsurface from the distribution of certain physical properties, upon which for instance, geological structures can be deduced. The complex nature of the subsurface and its compositional material has however made this a challenge, and this challenge has inspired the development of various methods and techniques in a bid to address it.

Geo-electrical methods as one of these, utilize the electrical properties of the subsurface - inductance, capacitance, resistance and charge storage - in imaging. The geo-electrical resistivity method operates based on the contrasting resistances of materials to direct current flow. This is a property which allows material distribution, extent and abundance to be effectively mapped. This can then be used to construct a subsurface profile.

This method has proved useful in shallow subsurface investigations with application in environmental studies, engineering, agriculture, archaeology, hydrogeology and mineral exploration. It is preferred for its wide range of usage, environmental friendliness and relatively low cost. In recent times, it has become more popular paralleling development of computing power and technology. Data acquisition, processing and interpretation as a result are now less labour-intensive and complicated, and relatively easier.

Geo-electrical resistivity measurements are normally made by 'injecting current' into the ground through two current electrodes (**A** and **B**, or **C1** and **C2**), and measuring the resulting voltage difference between two potential electrodes (**M** and **N**, or **P1** and **P2**) (Loke, 2000). From the current (**I**) and voltage (**V**) values, resistance (**R**) and subsequently, apparent resistivity ($\boldsymbol{p_a}$) values are then calculated according to a particular mathematical relation.

There is a geometric factor which depends on the spatial arrangement of the four electrodes, incorporated in this relation. These arrangement, known as arrays are specific and give rise to unique surveys (Loke, 2000). The most common conventional arrays which are used in electrical resistivity imaging are Wenner array, Schlumberger array and dipole-dipole array (Samouëlian et al., 2005). These, with their different geometric factors, offer unique implication for the measured resistivity.

An important characteristic of these arrays is their imaging capabilities, which ideally should be the criterion in selecting them. While the varying applications of the resistivity method require choosing the electrode array that is best suited to resolve the subsurface situation under investigation, field practicalities such as space and terrain constraints, surveying conditions, and the kind of equipment being used usually mean a compromise trade-off of the imaging ability to accommodate ease of operation.

### 1.2 Background

Research focusing on the performance of these standard electrode arrays for various geologic situations has resulted in conventions and tables of applicability of each array (Perren, 2005). Some of these are reported in works of Reynolds (2011), Roy and Apparao (1971), Telford et al. (1990) and Ward (1990). Most of these conventions and tables were obtained through

semi-quantitative data analysis on master curve fitting, pseudo-section matching and more recently numerical modeling experiments with synthetic data of idealized real field systems. These are amply referred to as "conventional wisdom" because they are widely available and commonly are the basis of array choice for modern usage (Perren, 2005)

However, measured resistivity is a result of a unique combination of factors among which primarily, is the physical and compositional characteristic of the subsurface material (porosity, permeability, fluid content, mineral type, and compaction) and also instrument sensitivity. 'Conventional wisdom' for all its fine points lacks the ability to predict this unique combination associated with a particular subsurface volume and therefore cannot compensate for. It is finite in this sense, and therefore cannot be contingent for every possible situation. This is a limitation which without proper appreciation could be fatally misleading.

It is therefore advisable to ascertain the suitability of an array not only for the subject of interest (job or studies), but also for a particular area. This is captured in the evaluation of the performance of the various arrays to deduce which will be best suited for a particular terrain and investigation.

### 1.3 Objective

The objective of this research is to evaluate comparatively the performance of three commonly used conventional collinear 'direct current' resistivity electrode arrays, Wenner, Schlumberger and dipole-dipole, with respect to their ability to resolve and define certain subsurface anomaly in the study area.

This will be done through the following:

i. Field surveys at selected sites in varied environment, aimed at imaging a common anomaly using all three arrays
ii. Comparison and analysis of the resulting profiles and sections

This is with respect to the 'very' near subsurface, incorporating isotropy/anisotropy and homogeneity/heterogeneity.

### 1.4 Justification of objective

Evaluation of array performance aids in selection of appropriate arrays. Appropriate field arrays and proper constraint parameters in processing work will lead to good results and interpretation. Reliability and effectiveness of these arrays are important for constraining near subsurface resistivity surveys.

### 1.5 Location, Physiography and Climate of Study Site

The study was carried out on the Legon campus of the University of Ghana, Accra. It is located in the Accra metropolis of the Greater Accra region, Southern Ghana. Currently, the University campus occupies a land stretch of about 8 $km^2$ bounded between longitudes $0^0$ 10'40"W and $0^0$ 12'0"W, and latitudes $5^0$ 7'50"N and $5^0$ 40'0"N.

The topography is relatively and largely high, with elevation reaching an approximate 167m in the Western part and then sloping gently to about 45m to the North (N), East (E) and South (S).

The climate is generally hot and relatively dry, consistent with the dry equatorial region conditions in Accra. This region has a more pronounced dry season, from November to February. The mean annual rainfall is about 79.6 cm, with the major rainy season being from

March to May. The average relative humidity also ranges between 75% and 60% (Dickson and Benneh, 1998).

### 1.6 Geology and Soil type of Study Site

The Legon campus is underlain by rocks of the Togo Structural Unit. This unit is part of the northeast-southwest (NE-SW) trending Neoproterozoic Dahomeyides, the southernmost extension of the Trans-Saharan mobile belts formed during the Pan African orogeny (Selley et al., 2005). The mobile belts are interpreted to have formed from collision of exotic blocks of the westward-bearing Benin-Nigerian shield with a passive continental West African craton, after closure of an ocean basin (Selley et al., 2005).

The Togo rocks are highly deformed sedimentary succession of alternating arenaceous and argillaceous protolith metamorphosed into quarzites, phyllites and schists (Kesse, 1985). Regionally, these are sandwiched between gneiss-granitoid basement terrain of the Dahomeyan Supergroup to the East, and the least deformed and metamorphosed Buem Structural Unit to the West. Stratigraphically, the Togo Structural Unit is underlain by the Dahomeyan, and overlain by the Buem. They are in contact through thrust-faulting, both to the East and the West. The west boundary fault also contacts the Birimian Cape Coast granitoid and the Voltaian sediments.

In the study area, common outcrops are quartzites. However, some phyllites and mica schists do occur sometimes intercalated with the quartzite, but these are subordinate.

The rocks are characterized by a southeast-dipping foliation, quartz veins, multiple joints and fracture sets, folds and shear fabric. Where they occur, they are mostly weathered.

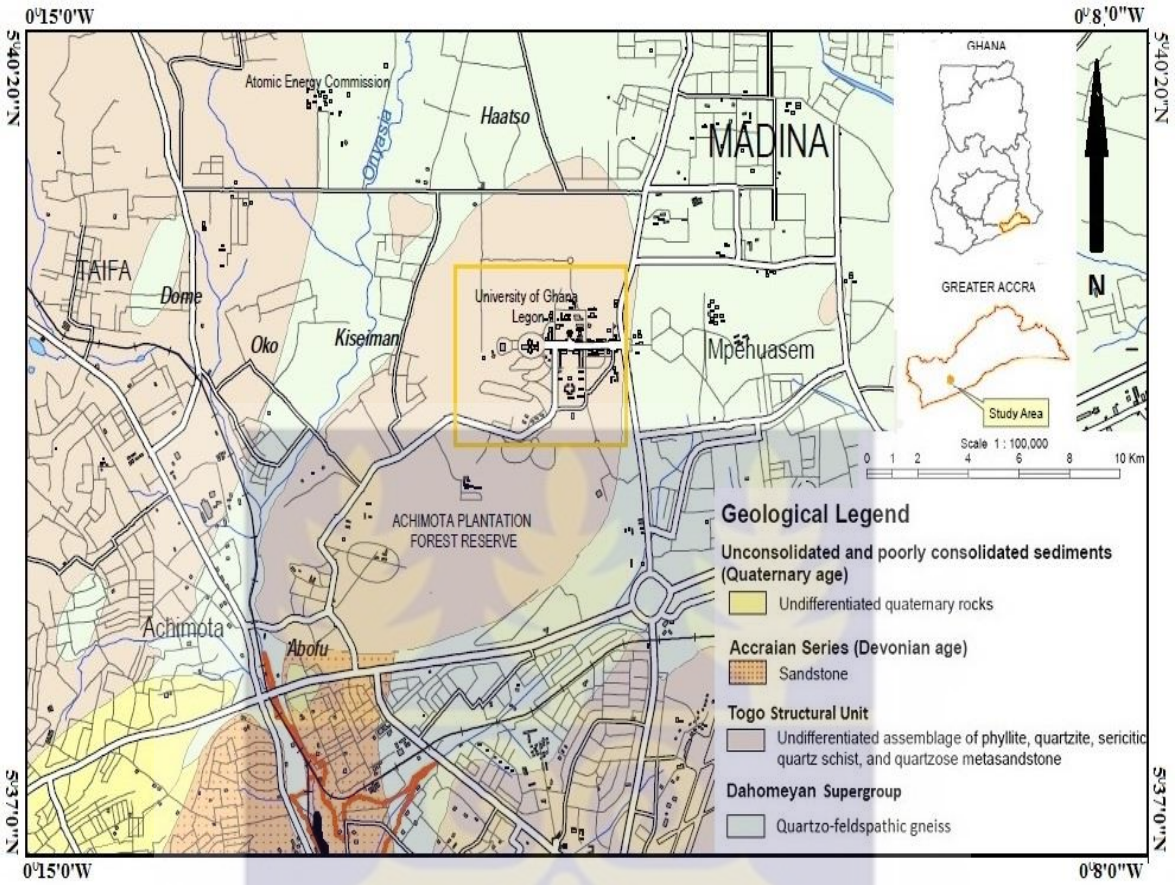


Figure 1.1 sketched geological map of some parts of Accra showing the study area ( after Anokwa et al., 2005)

The intense weathering has produced a thick overburden of lateritic soil, consistent with tropical nature of the region. Depth to bedrock usually range between 2 – 9 m but has been observed to reach about 18 m or more at certain areas (personal observation). Overburden thickness generally increase downslope – a possible indication of material deposition following slope gradient (Eze, 2008). The soil is largely sandy clay loams with high gravel content, ferruginized, with concretions and nodules as common features throughout the profile (Eze, 2008). At their thickest, the horizons are well developed and distinguishable, granular in the surface horizon to subangular and blocky with depth. The sandy clay loams in the surface horizons grade into predominantly clayey layers in subsequent horizons.

# CHAPTER TWO

# LITERATURE REVIEW

## 2.1 Versatility and Applications of the Resistivity Method

Resistivity varies from one material to another. This observed variation between materials can be used to distinguish them. Combined with reasoning along certain constraints, there is also the potential of identifying these materials. There are a large number of cases available, where this variability in resistivity of materials has been used practically in different fields and disciplines. Some of these have been examined below.

i. Resource exploration

The resistivity method has been a prominent feature in resource exploration since its development by Schlumberger brothers in 1919. More recently, it has been used successfully in mapping out shallow oil sands deposit (Bauman, 2005) and there has been focus on developing pragmatic ways of mapping out the deeper-seated conventional hydrocarbon resources (Loke et al., 2013). The resistivity method is however more famous in exploration for sulfide deposits, precious minerals and base metals. In most of these, it is not an independent method (Telford et al., 1990) but used in combination with other geo-electrical methods such as Self-Potential (S.P) and Induced polarization (I.P). I.P method is more efficient in mapping out disseminated sulfide ores. In such exercises, the resistivity method is used to highlight the contrast between the ore body and the host rock whereas I.P delineates the shape (Guo et al., 1999). Massive volcanogenic sulfide (VMS) deposits on the other hand, are associated with distinctive resistivity lows. The resistivity magnitudes of the

sulfides have been determined to be similar to that of graphite and sea water (Ford et al., 2007).

The resistivity method can also be used to map out conductive minerals associated with alteration haloes of these sulfide deposits. Most of these are conductive oxides and hydroxides of iron and certain metals, and clay minerals. Other minerals which have been successfully mapped include gold (Park et al., 2009; Guo et al., 1999), iron ore (Butt and Flis, 1997), graphite, bauxite, manganese and uranium (Loke et al., 2013). In the least, resistivity method could be used as a lead-up to other geophysical surveys such as ground gravity, in determining important parameters such as overburden thickness. This can improve results and interpretation (Morgan, 2012).

ii. Hydrogeology

The resistivity method has been a common investigative tool in hydrology and hydrogeology. Applications in these fields capitalize on the substantial influence of moisture on the bulk resistivity of earth materials. In its basic usage, it has been employed primarily in locating aquifers and underground water reserves, as well as optimum drilling points for borehole siting (Koefoed, 1979). Its use has since evolved and the resistivity method can be used to characterize the subsurface, establish hydrostratigraphy (Mastrocicco et al., 2010), and map out lithologies and geological structures controlling subterranean water flow and groundwater distribution. Advanced applications of the resistivity method seek to establish empirical relations from which certain hydraulic parameters can be determined or inferred. Combined with pumping test, some of these are hydraulic conductivity (Muhammad et al., 2013) and transmissivity (Oborie and Udom, 2014) and groundwater flow (Papadopoulou et

al., 2005). The resistivity method has been used in quantifying groundwater reserves and extractible amount (Agramakova, 2005) and monitoring groundwater extraction effect on lithologies. The latter, by extension, can also be used to monitor groundwater recovery rate. A combination of resistivity method and I.P can be used to determine how 'clean' an aquifer is, with respect to the sand and clay content. Clay is known to have high chargeability, while sands and gravels do not. Electrical measurements sensitive to variations in hydrogeological parameters do provide information with a comparatively better spatial resolution than hydrogeological methods alone (Loke, 2013).

iii. Engineering

The resistivity method is also widely used in engineering. Its application ranges from the location and mapping of bulk construction materials (Magnusson et al., 2010) to ascertaining structural compromises in artificial structures such as tunnels, dams and landfills (Tsourlos et al., 2014). It is popular in the delineation of bedrock interfaces and overburden thickness (Chambers et al., 2012), subsurface fractures and cavities (Ahmad et al., 2010) and seepages. Even though direct relationship between resistivity and the mechanical competence of materials have not been proved (Loke et al., 2013), extrapolations have been made based on observations relating certain petrophysical, hydrogeological and geotechnical parameters (Boadu and Owusu-Nimo, 2010). Andy et al. (2012) however examined empirical correlation between resistivity and the liquid limit, plastic limit, plasticity index, liquidity index, void ratio, porosity and degree of saturation of clayey sand soil samples. Other applications include landslide and slope stability studies (Andy et al., 2012), and geotechnical investigations into site suitability for certain engineering structures (Soupios et al., 2007). The resistivity method can also be used in locating buried artefacts such as tanks and pipes.

The method is commonly used in engineering with other geophysical methods such as seismic refraction and ground-penetrating radar (GPR).

iv. Environmental Investigations

Environmental investigations have the widest range of application of the resistivity method. Proof of this is the abundance of literature on the subject (Loke et al., 2013). Some common applications include delineating leachate contamination from landfill, contamination of groundwater (Akankpo and Igboekwe, 2011), sea water intrusion (Satriani et al., 2011) and acid mine drainage. Its importance is enhanced in that it is not only used in 'establishing', locating and delineating these environmental mishaps, it is also used in monitoring the phenomenon over time. In addition to monitoring, it could serve as a basis for evaluating the effectiveness of remediation exercises in comparing images taken over time. These contaminants often offer anomalously high concentration of ions which would translate into low resistivity compared to the surroundings. Sometimes the observed contrast could be as high 10 000:1 (Loke et al., 2013). This allows the plume to be effectively mapped. Some other environmental contaminants such as hydrocarbons have high resistivity, but still retain sufficient contrast to permit delineation.

Currently, this principle is being used in laboratory and field studies examining migration trends of fluids in certain environment (Slater et al., 2002). The resistivity method can also be used in delineating certain geological structures and geo-materials that control the flow of potentially toxic water. The identification and location of such structures could inform the distribution and concentration of such toxins. Mapping of contaminants aids in locating the

source; this can also be used in a more explorative sense in tracing acid mine drainage to a source, which could be a previously undiscovered, uncharted exposed ore.

v. Agriculture

The electrical property used most often in agriculture is electrical conductivity, which is the inverse of resistivity. This has been linked to how soils transmit and retain moisture, the presence and concentration of ions, and the amount and distribution of conductive clay (Loke et al., 2013). The presence of ions can also be linked to soil salinity, and its ability to store and recycle nutrients. The resistivity method has been used extensively to map soil structure horizonation (Tabbagh et al., 2000) and weathering profiles, image the tillage layer (Besson et al., 2004), monitor plant moisture uptake (Nijland et al., 2010), monitor water percolation and optimize irrigation patterns (Kelly, 2011). The resistivity method has also been used to map and quantify root biomass in soils (Rossi, 2011). Excessive salinization and possible contamination of the soil through cultural practices can also be detected. Boadu et al. (2008) used the resistivity method in mapping such contaminants, a nitrate infiltration from the overuse of fertilizers. In extrapolation, this can be an indication of plant nutrient uptake and the effectiveness of certain cultural practices.

vi. Archaeology

The resistivity method is also applied in the field of archaeology and cultural studies. This has been used over time in subsurface imaging as a guide for precision in excavation. It has been used in detection of buried artificial structures of archaeological value (Papadopoulos et al., 2012), discriminating buried artificial structures from natural subsurface structural highs and volumetric analysis of these structures (Loke et al., 2013). Other more advanced uses

involve distinguishing buried age-specific multi-layered structures and settlement within a single site and structural assessment of historical buildings put up over other pre-existing ancient structures (Apostolopoulos et al., 2014).

The method has found new application in the area of "rescue archaeology" (Loke at al., 2013), where suspected archaeological sites exposed during construction or threatened by other land developments need to be imaged swiftly, for decision-making (Apostolopoulos et al., 2012).

The resistivity method in all of its application is most often not used in isolation. Most investigations are integrated with other geophysical methods, providing a complementary data set. Geological, hydrogeological, geotechnical and geochemical data also aid in increasing certainty of results, and make for easy interpretation. Examples of such common complementary surveys and information are listed below.

- Resource exploration – Magnetic method, Gravity method, Electromagnetic (EM) method, Induced Polarisation (I.P) method, Self-Potential (S.P) method, Seismic reflection method, Geochemistry, Geology.
- Hydrogeology – Electromagnetic (EM) method, Hydrogeochemistry, Geology, ±Seismic refraction method ± Induced Polarisation (I.P) method.
- Environmental Investigations – Electromagnetic (EM) method, ± Seismic refraction method, Geochemistry, Geology.

- Engineering – Ground Penetrating Radar (GPR), Seismic (reflection and refraction) methods, Geotechnical assessment, Geology ± Electromagnetic (EM) method, ± Gravity method ± Magnetic method.

- Agriculture – Geology, Geochemistry.

- Archaeology - Ground Penetrating Radar (GPR), Seismic (reflection and refraction) methods, Geology ± Electromagnetic (EM) method, ± Gravity method ± Magnetic method.

## 2.2 Factors influencing resistivity

Movement of electric current in the shallow subsurface is mainly through ionic and electrolytic means. The electrolytic means is the more dominant, except in cases where the subsurface material contains high concentration of good conducting minerals. A number of factors have been determined to directly or indirectly influence this means of conduction with varying weights. These different weighted influences are responsible for the wide range of resistivity the subsurface exhibits in a particular environment. The most important of these are porosity (amount of pore space), the permeability (connectivity of pores), the water (or other fluid) content of the pores, and the presence and concentration of dissolved salts (Cardimona, 2002).

Current flows in the near subsurface by passage of ions through pores. If a large number of these pore spaces are interconnected, then movement is easier (less resistance) in the medium. This is then facilitated if the material has high moisture content with appreciable concentration of ions from dissolved salts. Summarily, resistivity values depend on the

effective porosity, moisture or fluid content and concentration of ions. Archie's Law relates these in

$$\rho = a\rho_w\varphi^{-m} \qquad (1)$$

where $\rho$ is the rock resistivity, $\rho_w$ is fluid resistivity, $\varphi$ is the fraction of the rock filled with the fluid, while $a$ and $m$ are two empirical parameters. For most rocks, $a$ is between 0.6 and 1 while $m$ is between 1.4 and 2.2 (Stummer, 2003).

Physical processes such as lithification and compaction are noted for increasing the resistivity of a material. Conversely, 'in situ weathering' and fracturing tend to decrease resistivity. Other factors such as clay content, volume of air, presence of conductive minerals when they occur significantly, also do affect the bulk resistivity.

### 2.3 Imaging Characteristics

Extensive work has been done and compiled on investigating the properties of arrays in order to advice their suitability for imaging anomalies with certain geometry and disposition (Szalai and Szarkai, 2008; Ward, 1990 and many others). These findings form the core character, the basis for which arrays are selected for specific tasks. Some of these have been summarized below.

i. Wenner Array

In the traditional Wenner array, potential electrodes are positioned within the current electrodes (nested configuration) with a common lateral distance between adjacent electrodes called the electrode *a*-spacing. The Wenner array generally provides for high signal-to-noise ratios, good resolution of horizontal layers, and good depth sensitivity. It has the strongest

signal strength, which is an important factor if the survey is in areas with high background noise (Loke, 2010). The Wenner array is good in resolving vertical changes (horizontal structures), but relatively poor in detecting horizontal changes (narrow vertical structures). It is not good at determining the lateral location of deep inhomogeneity (Ward, 1990) because the large *a*-spacing is known to degrade lateral resolution, and the potential electrodes are located within the spread of the current electrodes (Cardimona, 2002).

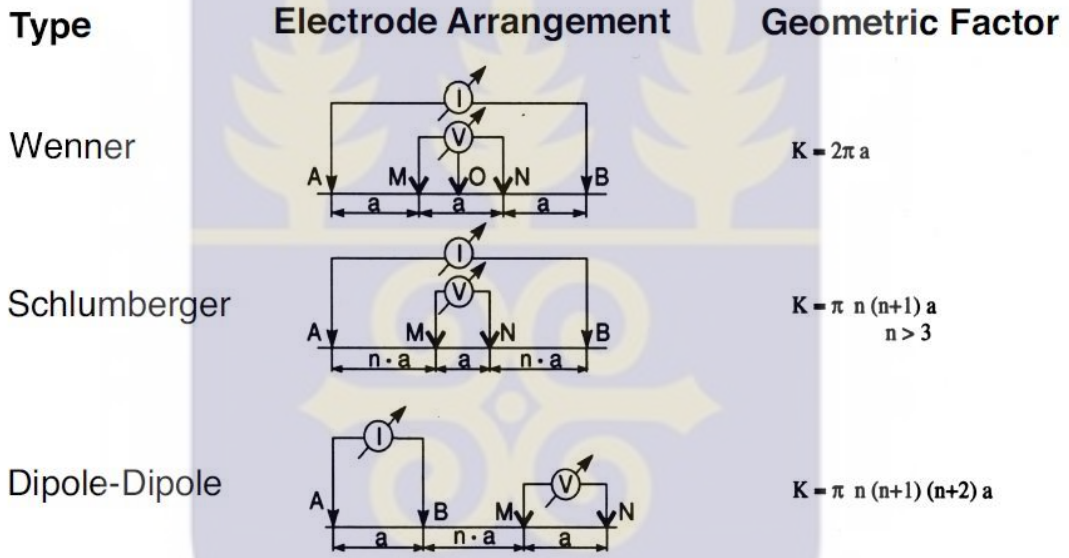


Figure 2.1 Collinear electrode configuration and their geometric factors (after Stummer, 2003).

ii. Schlumberger Array

Similarly, the Schlumberger array also has a nested potential electrode configuration. The array could be symmetric or asymmetric. Where symmetric (Wenner-Schlumberger), the potential electrodes have an inter-spacing of *a*. The current electrodes are spaced and increased a distance of *na* from the potential electrodes, where the integer value *n* varies dependent upon target size and depth. The Schlumberger array of electrodes provides for high signal-to-noise ratios, good resolution of horizontal layers, and good depth sensitivity

(Ward, 1990). In Wenner-Schlumberger array, the signal strength is weaker than that for the Wenner array, but it is higher than that of the dipole-dipole array. Wenner-Schlumberger array is moderately sensitive to both horizontal (for low "n" values) and vertical structures (for high "n" values). Wenner-Schlumberger array has been touted as a good compromise between the Wenner array and the dipole-dipole array (Alwan, 2013).

iii. Dipole-Dipole Array

The dipole-dipole array consists of a two-set electrode pair configuration of a current dipole and potential dipole. It has an intra-dipole separation of length *a* (for both current and potential) and an inter-dipole distance of *na*. It is particularly good in mapping horizontal changes (vertical structures), such as dykes and cavities, but relatively poor in mapping vertical changes (horizontal structures) such as sills or sedimentary layers. One possible disadvantage of the dipole-dipole array is the very small signal strength for large values of the "n" factor (Alwan, 2013).

For resolution of dipping layered structures, Ward (1990) also suggested the ranking of arrays from best to worse as: Schlumberger, Wenner and dipole-dipole.

Stummer (2003) proposed array selection should be based on problem definition (aim of survey). However, a number of factors deserve consideration. Some of these are depth of investigation, signal-to-noise ratio, ability to separate the anomaly by the measuring method itself (resolution), instrument sensitivity and ease of operation (simple measuring technique, equipment handling and measurement instrumentation). Others are safety, topography, communication, capital and ease of interpretation (Stummer, 2003; Summer, 1976; Szalai and Szarka, 2008) and personal preference.

Nonetheless, availability of logistics usually leads to preference of one array over the factors.

### 2.4 Sensitivity Analysis

In evaluating array performance, the optimum depth of investigation and the sensitivity to near surface inhomogeneity are quite important.

According to Stummer (2003), earlier works by Van Nostrand (1953) defined depth of detection as the depth below which a target cannot be detected with a given array assuming that the value of the minimum detectable anomaly was 10 % above the resistivity of the host rock. Muskat and Evinger (1932) also showed that the depth of current penetration was a function of separation between current electrodes but depth of investigation depended on all four electrodes. Roy and Apparao (1971) and later Roy (1972) also through experiments developed depth of investigation characteristic curves (DIC) and an associated table of depth of investigation relative to the characteristic lengths of the arrays. This was later improved by Edwards (1977). These were based on homogeneous ground and two-layer model assumptions.

Numerical approaches and inversion algorithms have been used by Dahlin and Loke (1998), Oldenburg and Li (1999) on synthetic data sets generating and comparing models. Oldenburg and Li (1999) defined a new resulting parameter 'Depth of Investigation Index' (DoI) as the depth below which subsurface data is insensitive to physical property variations.

Sensitivity defines observed changes in potential per changes in resistivity of a cell volume. An array's sensitivity function quantifies the extent to which differences in resistivity of a part of the subsurface will influence the potential measured by the array. These resulting variances in imaging capability are often expressed in the model inversion images, deviations

from the true resistivity model values, tendency of the array to produce artefacts, maximum depth of investigation attainable and spatial resolution of the arrays (Okpoli, 2013).

A number of approaches (numerical and analytical-based) have been used to investigate this systematically, using models generated from real and synthetic data.

Spitzer (1998) has showed three numerical approaches for arbitrary resistivity structures and an analytical solution for a homogeneous half-space. These techniques include forward modelling using a source at the transmitter and the receiver location; a direct current finite difference partial differential equations approach and a two direct current "forward runs" using perturbation of a resistivity block. Sensitivity functions over homogeneous and layered earth models and sensitivity patterns have also been presented and discussed by Spritzer (1998) for the various arrays.

For a given source and receiver configuration of electrodes, the sensitivity function $S$ is expressed as the inner product of the current densities $\vec{J}_S$ and $\vec{J}_R$ produced by a current source of strength $I$ at the source and receiver positions, respectively, integrated over the perturbed volume $dV$:

$$S = \frac{\Delta\Phi}{\Delta\rho} = \frac{1}{I}\int_v \vec{J}_S \cdot \vec{J}_R dV. \quad \textbf{(2)}$$

Sensitivity studies are usually carried out in conjunction with inversion techniques. Some proposed factors affecting sensitivity include data density and lateral coverage, depth of penetration, damping factor and noise contamination, and geologic conditions (Okpoli, 2013).

Sensitivity analyses are major advances made in a bid to understand electrode geometry and the associated electric field. The nature of these fields primarily determines the investigation depths and the ability of the array to near-accurately resolve features of interest. However, the propagation of these electric fields depends upon the subsurface material structure, and this for a large part remains unknown and unpredictable. Even with constraints, the prediction power of sensitivity patterns are observed to only approach reality asymptotically.

### 2.5 Isotropy/Anisotropy and Homogeneity/Heterogeneity

In a geophysical sense, a rock is said to be electrically anisotropic if the value of a vector measurement of its resistivity varies with direction (Ehirim and Essien, 2008). This is a common characteristic of most rock types exhibited on different scale. It is most notably caused by the formation layering, fracturing, joints and fault systems, grain boundary cracks and aligned mineral grain orientations which are common features of rocks. The scale varies from micro – to macro - anisotropy covering the variation of resistivity from within a given layer or lithology to alternating layers or beds of rock, respectively (Sauck and Zabik, 1992). The extent of anisotropy is quantified by the anisotropy coefficient, which is the square root of the ratio of the measured maximum to minimum resistivity (Jones, 2007). Keller and Frischknecht (1966) tabulated a range of anisotropy coefficients for some common layered rocks. Where electrical anisotropy exists, convenient assumptions fail. Effects are that actual geological depths and structures are wrongly imaged, and petrophysical parameters are wrongly estimated (Ehirim and Essien, 2008). Azimuthal surveys have been used to identify, establish and characterize the directional properties of anisotropic rock mass in the area of concern.

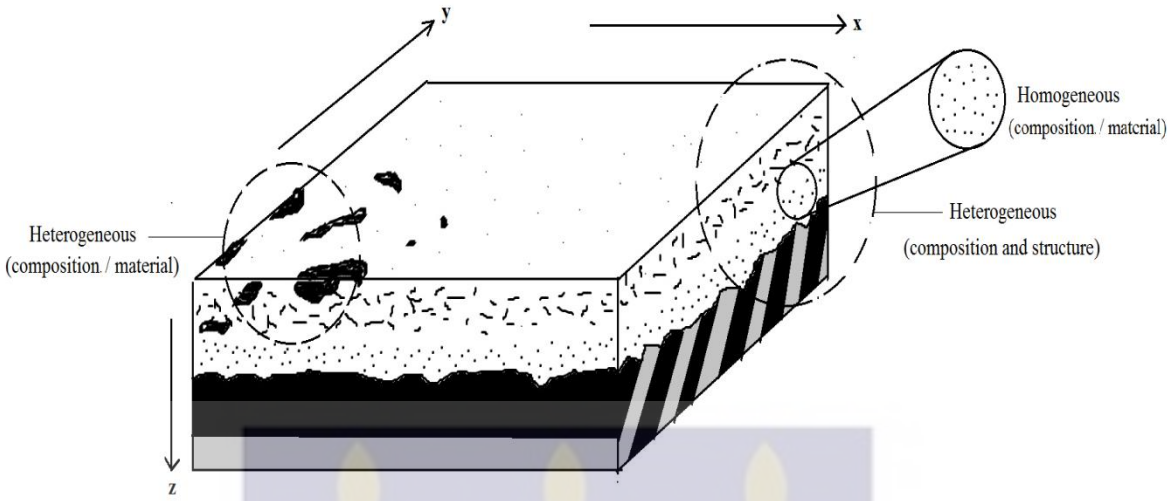


Figure 2.2 Sketched diagram of a subsurface possessing both structural and compositional heterogeneity.

In such surveys, observed changes in apparent resistivity as a function of azimuth is interpreted as an indication of structural inhomogeneity (most often fracture anisotropy). This in most cases is true, being produced by the presence of dipping beds or preferential fracture trends (Watson and Barker, 1999). This holds when the volume of subsurface being investigated is made up of bedrock, or an in-situ subsurface material still retaining structures. Such is seen in investigations of greater depth.

Where the 'very' near subsurface is involved (overburden and weathered material zone), observed electrical anisotropy cannot be attributed to structural inhomogeneity but rather compositional or material inhomogeneity. The weathering effect as rocks near the surface break down produces a somewhat distinct horizontal layering which is evidenced by disciplined horizons seen in soil profiles. This is irrespective of the structural character of the parent or country rock (whether possessing layers with a sense of dip or no). Even though these zones are 'structurally' homogeneous (horizontally layered), electrical anisotropy is still observed. A plausible explanation would be lateral changes in apparent resistivity due to

material heterogeneity within and across these layers affecting the electric field produced and redefining current paths. Figure 2.2 shows a sketched diagram of such a subsurface, with structural inhomogeneity at depth (dipping beds) and structural homogeneity in the near subsurface (orderly lateral extension and layering of material or soil profile).

The 'very' near subsurface is highly heterogeneous, incorporating natural diversities in material chemistry, physical texture, and considerable introduction of foreign material through anthropogenic activities. The variations in the electrical properties (resistivity/conductivity) of these materials alter the current density and flow path. The equipotential surfaces, perpendicular to the current flow, are modified by the deflection of the electric current near inhomogeneity. The deflections are primarily due to the subsurface material directly below the survey line (in the survey plane), and the measured apparent resistivity will represent an average of the varying resistivity along the current path through the subsurface. Hence, the more heterogeneous the subsurface, the greater its influence on the bulk resistivity measured. It would therefore be a logical arrival that the more sensitive a particular array is to this heterogeneity, the more it would reflect in the reported resistivity value.

A rock is an aggregate of minerals with different electrical properties. The electrical character of the rock as a whole can be said to be a crude average of these properties. As weathering sets in in the near surface environment, these minerals are often times seen separated into individual grains. This new material posture would differ in electric character than that expected from the regular more compact framework. Intense chemical weathering also leads to mineral alteration and with it a loss or adulteration of the original characteristic electrical properties. Mechanical breakdown of the resulting mineral grains in a preferential

manner, and to varying extents (degree of roundness/ angularity, size of crystals/clasts among others) play a prominent role in determining the texture of the material being sampled. Resistivity is affected by material texture.

The magnitude of influence of anthropogenic activities is proportional to increased human presence. With this most notably, is uneven surface compaction phenomenon. The unevenness in near subsurface compaction is an introduction of heterogeneity in itself, and the varying degree and extent has a pronounced effect in the overall phenomenon. Mention can be made of the contribution of plants and plant remains, especially in the A and B soil horizons when the 'very' near subsurface is of interest. Organic matter is notorious as highly resistive and when in relative abundance could have a telling effect on observed values. Indirectly, plant root actions affect secondary porosity which in turn affects subsurface ion mobility. Its contribution to heterogeneity is proportional to its relative abundance and extent of uneven distribution and occurrence.

Resistivity is a unique blend of a number of factors. Upsetting any of these will lead to a pronounced deviation from the expected. It is such differences which produce the observed changes from one location to the other.

# CHAPTER THREE

# METHODOLOGY

## 3.1 Theory and Principles

Ohm's law describes the electrical properties of any medium, relating voltage to the product of current and resistance. This relationship holds for simple circuits as well as earth materials.

The total resistance **R** in Ohms, of a material of length **L** and cross-sectional area **A** of uniform composition can be obtained experimentally through Ohm's law

$$R = \frac{V}{I} \qquad (3)$$

where **V** is the potential difference in Volts (V) between the ends of the material length and **I** is the total current in Amperes (A) flowing through the material.

This is then made specific by relating the resistance to its physical geometry.

$$R = \frac{\rho L}{A} \qquad (4)$$

**ρ** is the material-specific constant of proportionality for the total resistance **R,** observed. The resistivity **ρ** of a material is then an intrinsic property of that material, which can be related to measured extrinsic parameters, area **A** and length, **L**.

$$\rho = \frac{V}{I} \bullet \frac{A}{L} = RK \qquad (5)$$

Application to the earth and earth materials is more complex because current is not restricted to flow along a single path. A subsurface of uniform composition with a single current

electrode located on the surface of the ground will have current flowing in a radial pattern away from it (Herman, 2001). Equipotential surfaces are generated perpendicular to direction of current flow, with the potential being inversely proportional to distance from the current electrode. The more realistic two-current electrode system (**A** and **B**) will have current flow in the subsurface for both homogeneous and heterogeneous environment as illustrated in figures 3.1a and b respectively. The equipotential surfaces are represented as solid lines while the unit vector (arrow) shows the direction of electric field. The spacing between the two current electrodes determines the effective depth of current penetration. If the spacing is increased, current will penetrate deeper and vice-versa. The distribution of subsurface resistivity determines the path of current flow. Current density increases in conductive regions and decreases in resistive ones. Such variation in subsurface resistivity tends to cause current to refract, as it travels through these regions between the electrodes (Jones, 2007).

This alteration of current flow between the electrodes enables boundaries to be detected, based on the contrast between two materials as well as values of their resistivity.

For a two-layer subsurface system (higher resistivity above and lower, below), when the spacing between the current electrodes is lesser than the depth of the boundary between the layers, most of the current will not encounter the region of lower resistivity. This means that the total resistivity measured at the surface will be mostly due to the material that lies above the boundary. When the current electrodes are placed further apart, the current penetrates into the region of lower resistivity, and the observed total resistivity now becomes a weighted average of the resistivity of both layers (Herman, 2001).

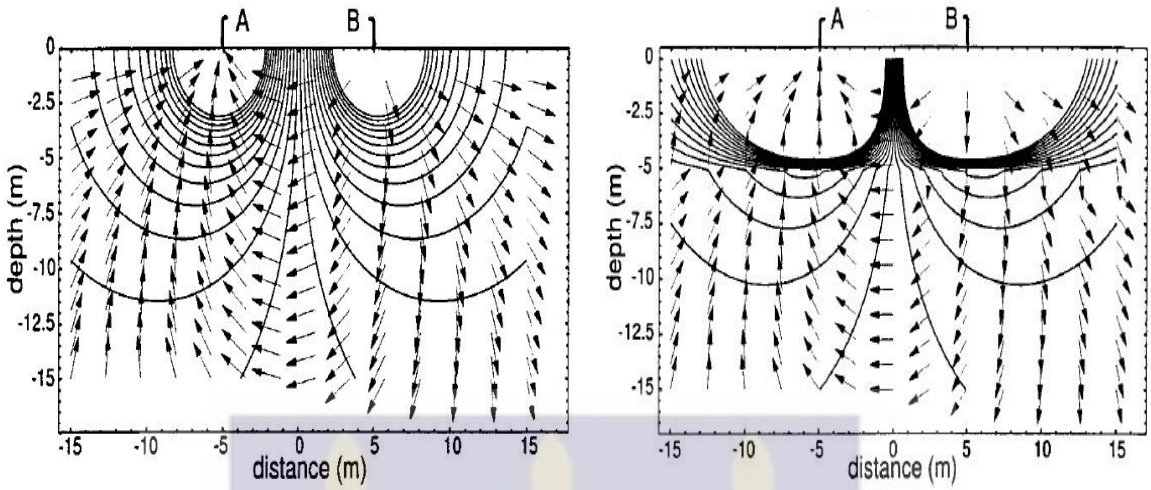


Figure 3.1 Distribution of current (arrows) and potential lines (solid lines) for two current electrodes at the surface with (a) homogeneous subsurface (b) inhomogeneous two-layered subsurface (after Herman, 2001)

In every heterogeneous subsurface environment (as it mostly is), similarly, the observed resistivity is a weighted average of the resistivity of the various materials that the current encounters. It represents that of an entire volume, and not a particular material or location. As such it cannot be the true resistivity of any of the underlying material, but rather the apparent resistivity, $\boldsymbol{\rho_a}$.

Just as the resistivity obtained are apparent resistivity and not the true resistivity of the underlying material, so are the effective depths not the exact depths of the locations of the boundaries between the various materials or layers. This again is due to the fact that the current is so spread out and does not flow in a perfectly defined layer of exact thickness as it travels through the volume of material between the current electrodes (Herman, 2001). Subsurface profiles and images constructed from such lateral and vertical apparent resistivity distribution and effective depths are known as pseudo-sections (Hallof, 1957). Even though true depth information cannot be directly inferred from pseudo-sections, they are valuable tools for qualitative analyses and quality control (Dahlin, 1996).

True resistivity values and actual depths may be obtained through various 'inversion methods' (Herman, 2001). Data inversion is geared towards finding that model of the subsurface whose resistivity character is most similar to the measured field values. Without inversion of the resistivity data, depths as plotted in pseudo-sections are normally an overestimation or underestimation of the true depth of investigation.

The effective and true depths, and apparent and true resistivity yields of the subsurface have been included for analysis in this work.

### 3.2 Arrays

Assuming a subsurface of uniform composition and infinite extent with one source and one sink electrodes for the current, the total current **I,** flows away from or toward each electrode across the surface of a half sphere with area **A**

$$\mathbf{A} = \frac{1}{2}(4\pi r^2) \qquad \textbf{(6)}$$

The vector form of Ohm's law can be written as

$$\mathbf{J} = \sigma\mathbf{E} \qquad \textbf{(7)}$$

where **J** is the current density, **σ** is the conductivity of the medium and **E** is the electric field intensity

The relation between the electric potential and the field intensity is given by:

$$\mathbf{E} = -\nabla\phi \qquad \textbf{(8)}$$

Combining equations **(7)** and **(8)**

$$\mathbf{J} = -\sigma\nabla\phi \qquad \textbf{(9)}$$

The current sources are point sources. Thus, the current and the current density over an elemental volume $\Delta V$ around the current source I, located at ($x_s$, $y_s$, $z_s$), according to Dey and Morrison (1979) is given by :

$$\nabla \bullet \mathbf{J} = \frac{\mathbf{I}}{\Delta \mathbf{V}} \delta(\mathbf{x} - \mathbf{x_s})\delta(\mathbf{y} - \mathbf{y_s})\delta(\mathbf{z} - \mathbf{z_s}) \qquad \textbf{(10)}$$

The resistivity ($\rho$) of the medium is the inverse of the conductivity ($\rho=1/\sigma$). Equation **(7)** can then be rewritten as

$$\mathbf{J} = \frac{\mathbf{E}}{\rho} = \frac{\mathbf{I}}{\frac{1}{2}(4\pi \mathbf{r}^2)} = \frac{-1}{\rho \frac{\partial \mathbf{v}}{\partial \mathbf{r}}} \quad \textit{(}\text{for one electrode)} \qquad \textbf{(11)}$$

It follows that for a constant **ρ,** when integrated for a potential **V**, **r** distance away from that electrode, the equation simplifies to

$$\mathbf{V(r)} = \frac{\rho \mathbf{I}}{2\pi \mathbf{r}} \qquad \textbf{(12)}$$

The electric potentials measured at **M** and **N** in the general linear array (figure 3.2) are superpositions of the potential due to each of the two source electrodes located at **A** and **B** with the distance **r** between the electrodes given by **AM, MB, AN** and **NB**.

The potentials at **M** and **N** are given by

$$\mathbf{V_M} = \frac{\rho \mathbf{I}}{2\pi(\frac{1}{\mathbf{AM}} - \frac{1}{\mathbf{MB}})} \textbf{ and } \mathbf{V_N} = = \frac{\rho \mathbf{I}}{2\pi(\frac{1}{\mathbf{AN}} - \frac{1}{\mathbf{NB}})} \qquad \textbf{(13)}$$

The total potential difference between the electrodes **M** and **N** is thus

$$\mathbf{V} \text{ or } \mathbf{V_{MN}} = \frac{\rho \mathbf{I}}{2\pi(\frac{1}{\mathbf{AM}} - \frac{1}{\mathbf{MB}} - \frac{1}{\mathbf{AN}} + \frac{1}{\mathbf{NB}})} \qquad \textbf{(14)}$$

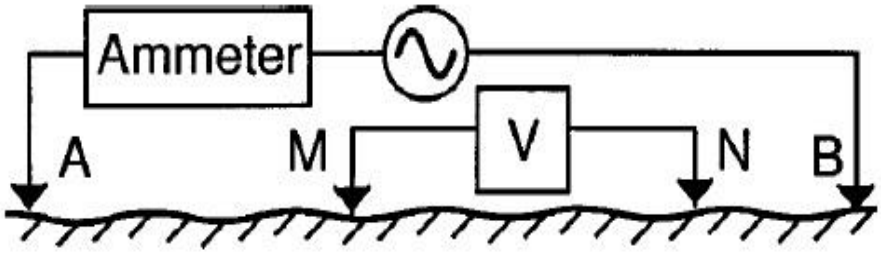


Figure 3.2 A conventional four electrode array set-up to measure subsurface resistivity (after Herman, 2001)

Equation **(14)** may be rearranged to give

$$\mathbf{V} = \frac{\mathbf{V}}{\mathbf{I}} \bullet \mathbf{K}, \qquad \mathbf{where\ K} = 2\pi\left(\frac{1}{\mathbf{AM}} - \frac{1}{\mathbf{MB}} - \frac{1}{\mathbf{AN}} + \frac{1}{\mathbf{NB}}\right) \qquad \mathbf{(15)}$$

Geometric factor **K** is therefore dependent upon the spatial arrangement of the electrodes, and it is these specific spatial arrangements which give rise to the different arrays.

### 3.3 Study Area and Anomaly selection

#### 3.3.1 Phase One

The study area is underlain by crystalline rocks, highly metamorphosed and deformed. This deformation as seen in exposures includes prominent brittle structures and fracture zones; predominantly pervasive, and known to increase secondary porosity and permeability. However, the observed thick overburden associated with the area obscure the surface expression of these structures, and for a large part they are represented in the near surface as expressions of peculiar texture, colour and sometimes alteration. More often, these areas are zones of weakness and serve as ready pathways for percolation. As a result, they are known

to be associated with pronounced low resistivity, such as are targeted during surveys for borehole siting and are usually observed around producing ones.

For purposes of the study, fifteen of such producing borehole sites (sited and developed) were selected as possible ground anomalies for imaging for the first phase. Information as to their location, distribution and character were acquired from the Physical Development and Municipal Services Directorate (PDMSD) of the University of Ghana and the drillers, Heisa Engineering. Figure 3.3 shows the location and distribution of the boreholes.

### 3.3.2 Phase Two

A second site, an approximately 200 $m^2$ temporary dumping ground located in the southern part of the university campus was selected for imaging for the second phase. A complex resistivity distribution was anticipated for the 'very' near subsurface as a result of the dumping activity and current remediation exercises. Rapidly varying resistivity with sharp contrasts was expected paralleling laterally varying artificial inhomogeneity, caused by refuse material of different nature at different stages of degradation. Also, the remediation approach of clearing part of the refuse with heavy machinery had incorporated some of these materials into the top soil layer with variable compaction. The location of the site is shown in figure 3.3.

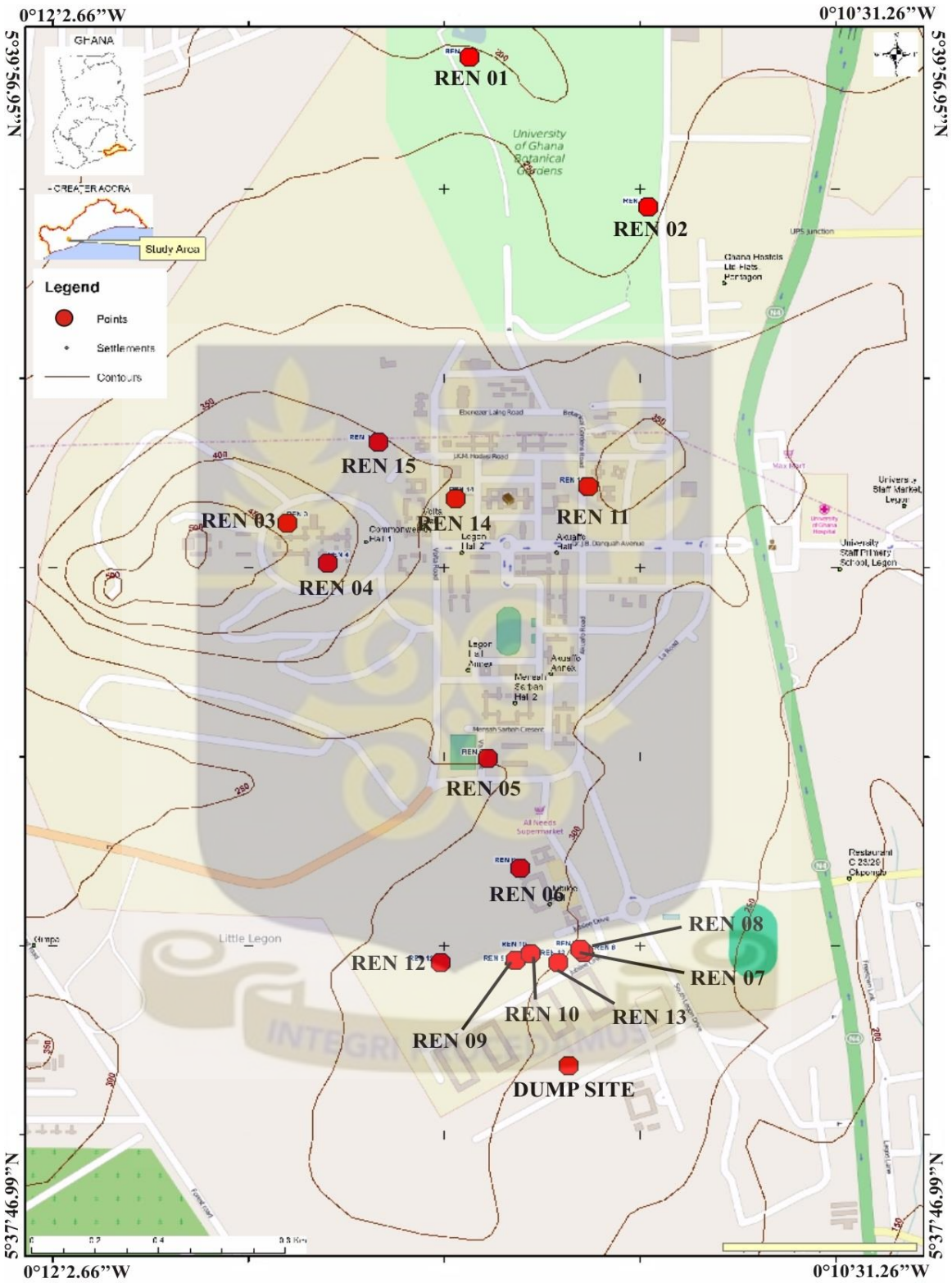


Figure 3.3 Map of study area showing location and distribution of survey points (Boreholes and Dumpsite)

The site was selected for two reasons;

i. It presented an ideal setting to assess the performance of the arrays in a 'noisy' environment.

ii. Also, it presented an opportunity to assess the ability of the arrays to image anomaly with no definite geometry such as possible leachate contamination and seepage.

### 3.4 Instrumentation

'Imaging' was carried out using standard survey equipment – electrodes, cables, global positioning system (G.P.S), compass and a resistivity meter. The resistivity meter used for the first phase was the single channel SARIS (Scintrex Automated Resistivity Imaging System) Resistivity module from Scintrex, Canada. A ten channel IRIS Syscal Pro was used for the second phase. The electrodes were 0.7 m-long, 0.02 m-wide tapering tip steel rods and the cables, a 0.003 m-wide insulated copper core conveniently wound onto reels. The GPS was a Garmin VISTA HCx and the compass a Konustar. Other components were clips, plugs and connectors, hammers, pegs and tape measure.

### 3.5 Survey design and Data acquisition

#### 3.5.1 Phase One

The survey was designed to 'image' lateral and vertical variation in resistivity across the boreholes in the study area, and in the process, possibly delineate resistivity anomalies. This was with respect to subsurface anisotropy.

Profiling was done on 40-50 m traverses across the boreholes, targeting three different depths. The traverses were oriented in two perpendicular directions, the first, paralleling the local structural trend of the rocks (SW-NE) in the area – Traverse A, and the other, across it (SE-NW) – Traverse B. The local trend of the rocks (strike) from literature and actual field measurement ranged between 028° – 040°. This was used as a guide for marking out the traverses.

Profiling was with all three configuration – Wenner, Schlumberger and dipole-dipole – while using approximately the same current electrode distances (similar distance between A and B electrodes), corresponding to a particular investigation depth. This was for the Wenner and Schlumberger arrays. Three of such current electrode distances were used. The dipole-dipole array expansion was done about the mid-point increasing the n-factor while the current and potential pairs were kept constant. The various array configurations are shown in Figure 3.4.

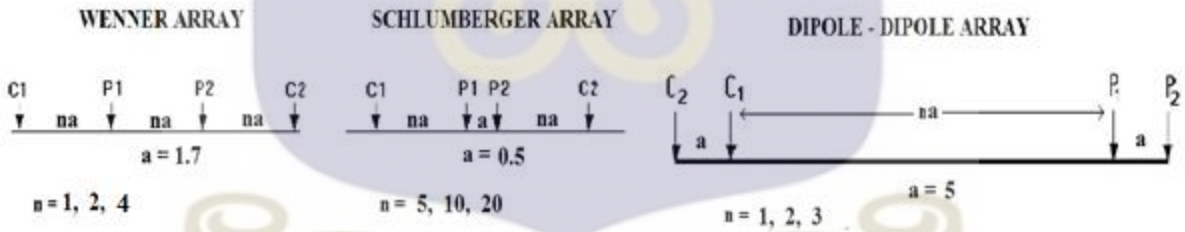


Figure 3.4 Dimension of arrays used in profiling

Profiling was a constant separation traverse with inter-sampling distance of 5 m. With at least 8 sampling points per traverse along a particular depth, all 3 depths yielded about 24 resistivity measurement per array for each direction. This was done for all 15 boreholes sites. The sites have been named numerically in order of sampling, with 'REN' as prefix. Summarily, 270 profiles were run targeting 3 different depths in the two orthogonal

directions using all three arrays. All sampling points on the traverse for the various arrays were co—located.

Analysis of the apparent resistivity data acquired was qualitative. Comparison was in the general resistivity character observed along and across depth, magnitude and range of resistivity values, similarity of trends, parallelism of trends and erraticism in the trends. Comparison was also between profile plots of the various arrays for each traverse, per site. Increase in current electrode spacing (AB) was assumed as an increase in effective depth of probing. $D_1$, $D_2$ and $D_3$ refers to depths corresponding to AB=5.1 m (n=1), 5.5 m (n=5) and n=1 (for dipole-dipole), AB=10.2 m (n=2), 10.5 m (n=10) and n=2 (dipole-dipole), and AB=20.4 m (n=3), 20.5 m (n=20) and n=3 (dipole-dipole) configurations respectively for Wenner, Schlumberger and dipole-dipole arrays. The apparent resistivity was reported in Ohm-metre (Ωm). The borehole position in the plots is located at 0 m offset.

### 3.5.2 Phase Two

The survey was designed to target the sharply varying resistivity character of the 'very' near subsurface of the dumpsite and the performance of the arrays in imaging this, and the related anomaly in that setting.

Profiling was initially carried out on two perpendicular traverses, a 20 m SW-NE line (Traverse A) and a 30 m SE-NW line (Traverse B), for three different depths.

This was to observe and establish the vertical and lateral character (with respect to anisotropy) of the complex resistivity nature of the site. The traverses were positioned to cover parts of the active (northern) and passive (southern) portions of the dumpsite on each

line. Figure 3.5 shows a schematic diagram of the site, not drawn to scale. Profiling was at constant separation with 1 m inter-sampling distance. The array dimensions are also shown in figure 3.7.

A second set of profiling was done along a 10 m stretch on the SW-NE line based on results from the first. Profiles along this traverse showed comparatively sharper resistivity variation. The profiling was also along three different depths and targeted an artificially emplaced material in the upper more complex part of the imaged subsurface. The material was a 0.5 m thick unit of rock salt extending 2 m, emplaced in a 1.2 m-deep trench created along the part of the traverse exhibiting sharp resistivity contrasts both laterally and vertically. A sketched diagram of the trench section is shown in figure 3.6. Based on its electrical properties, the rock salt was selected as it could still provide a pronounced contrast (anomalous drop) in the presence of the observed sharply varying resistivity character of the site at shallow depth. The array dimension corresponding to the depth of the buried salt was obtained by vertical electrical sounding (VES) using both Wenner and Schlumberger array methods.

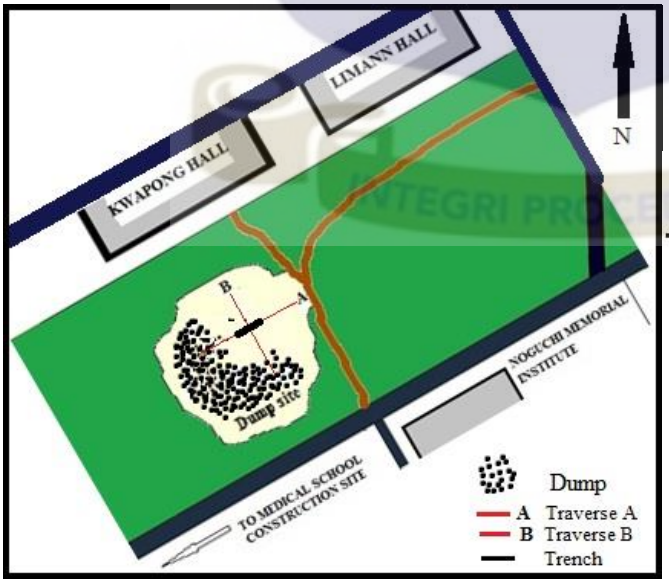


Figure 3.5 Sketch of the dumpsite (not drawn to scale)

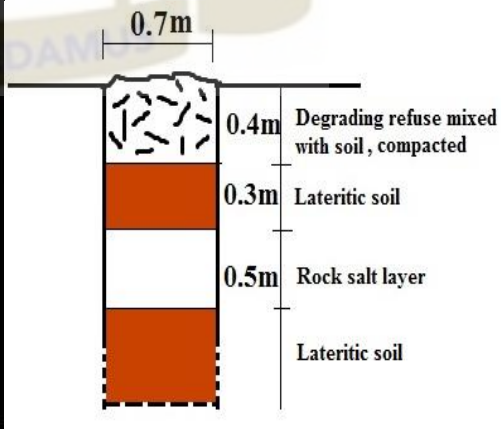


Figure 3.6 Cross section of trench

The sounding was on two points along the trench, with a metre interval. The salt unit showed the expected anomalous drop in both sounding curves (figure 4.3.2). Based on this, three profiles were run with array dimensions corresponding to the depth of the salt layer, above and beneath it. The array dimensions are shown in figure 3.7. Profiling was at constant separation with inter-sampling distance of 0.5 m, in order to increase the resolution of the resulting images. All sampling points on the traverse for the various arrays were co—located.

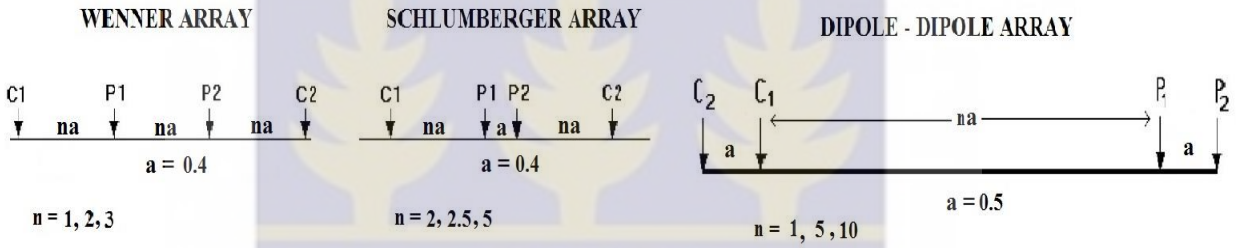


Figure 3.7 Dimension of arrays used in profiles targeting buried salt unit

### 3.6 Data Reduction and Processing

Measurements on the field were repeated a number of times over each sampling point to establish consistency. The mean of these values were recorded and the standard deviations of subsequent points were also noted. Standard deviation limit was set at 8%, above which values were rejected or measurements retaken. The data was then checked for measurement artefact (spikes and sharp drops), and sampling points reporting such anomalous resistivity were re-sampled to ascertain the possibility of instrumentation error, poor electrode-ground contact and electrode shortening, and data duplication occurring.

The apparent resistivity values for all three arrays for each borehole site were plotted as profiles (apparent resistivity against offset), using the 2007 version of Microsoft's Excel. 90 of these plots were produced for qualitative analysis.

Data set from the dumpsite was inverted, using RES2DIV program (ver.3.59.) from Geotomo Software to give true resistivity sections of the near subsurface. Data set for the first profile (Traverses A and B) was inverted using the standard smoothness-constrained least square method. It is most suitable for data where gradual change in resistivity is expected such as when delineating contamination plumes (Tamssar, 2013). The second profile data set (Traverse across salt layer) on the other hand, was inverted using the robust method which is recommended for highlighting sharp boundaries in resistivity variation. It is also suitable when abrupt discontinuities in resistivity trend is expected (Tamssar, 2013), such as in a laterally varying heterogeneous subsurface.

The damping factor was optimized and the widths of the model cells were set at half the unit electrode spacing to accommodate the large near surface resistivity variation.

# CHAPTER FOUR

# RESULTS AND DISCUSSION

Resistivity profiles and sections from the surveys have been presented and discussed below. A combination of the profiles obtained for the various depths investigated, effectively constituted a two-dimensional (2-D) data distribution with resistivity changes in both vertical and horizontal directions as measured along the survey line. This yielded a more comfortable overview of the resistivity variations in the subsurface section below the traverses.

## 4.1 Borehole Sites

Profile patterns from the plots showed a range of trends (from regular well-defined trends to undulating, erratic and ill-defined trends), reflective of the sub-environment (subsurface environment) where the boreholes were sited. The patterns for each array have been compared across depth ($D_1$, $D_2$ and $D_3$) for each traverse, and also between traverses (A and B) for each site. Similarity in resistivity values between traverses is indicative of similar conductivity along those directions. A wider range in resistivity values is also suggestive comparatively, of the extent of lateral inhomogeneity along that traverse direction.

### 4.1.1 REN-01

Apparent resistivity values for the Wenner array ranged between 3.49 - 46.52 Ωm. The resistivity values were largely the same for both traverses. Profile patterns were also similar for both traverses. The profile plots are shown in figure 4.1.1a.

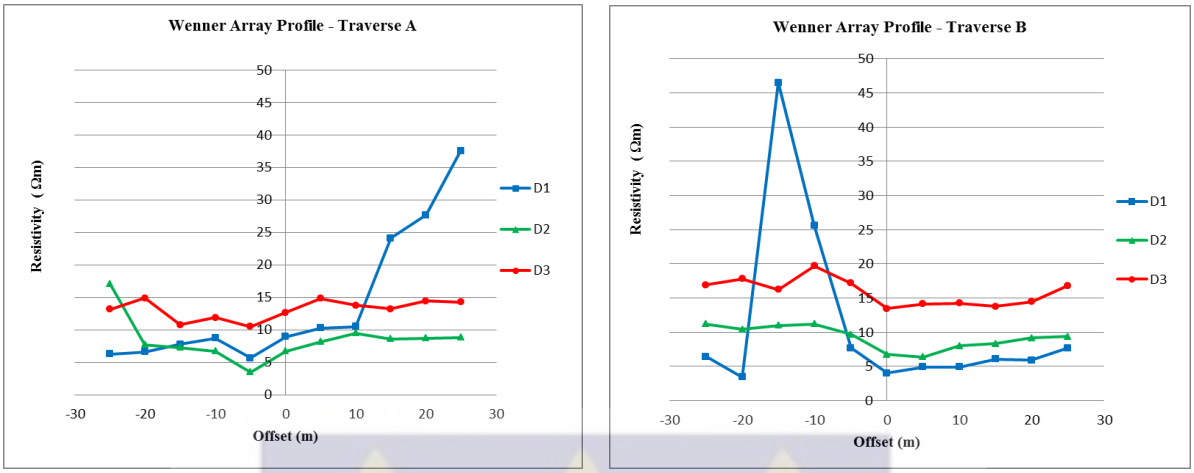


Figure 4.1.1a Wenner Array Profiles for REN-01 (SW-NE for Traverse A, SE-NW for Traverse B)

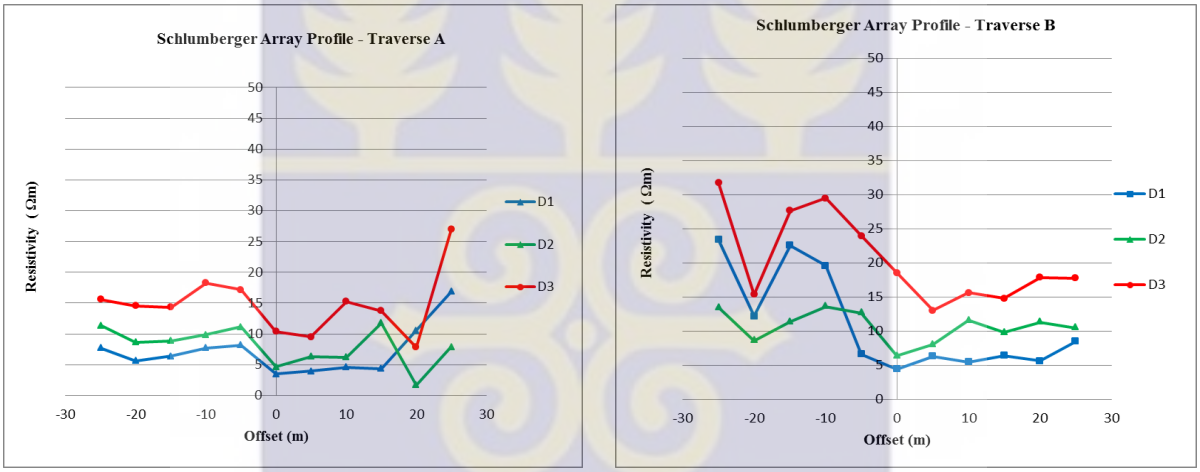


Figure 4.1.1b Schlumberger Array Profiles for REN-01(SW-NE for Traverse A, SE-NW for Traverse B)

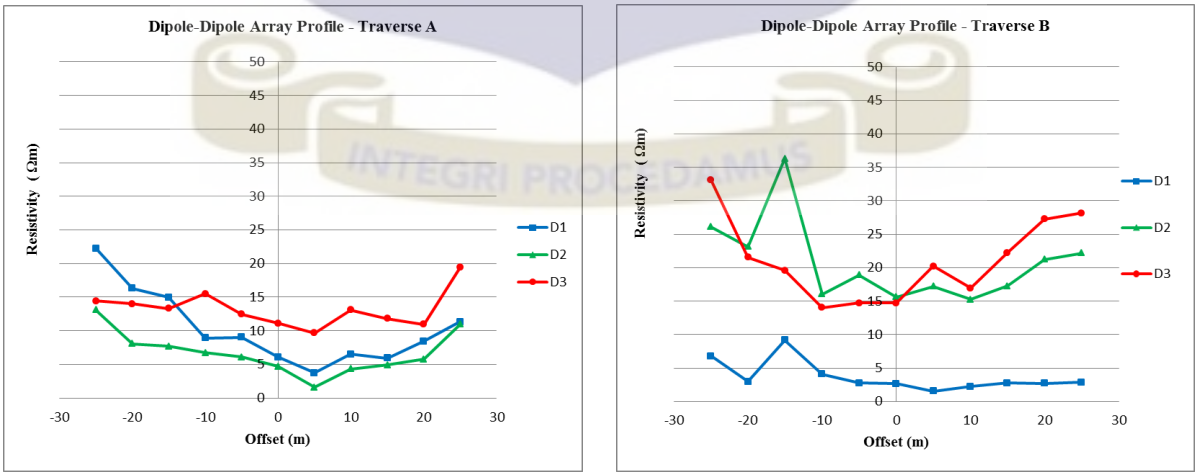


Figure 4.1.1c Dipole-Dipole Array Profiles for REN-01 (SW-NE for Traverse A, SE-NW for Traverse B)

Where $D_1$ = 1st Depth (Shallow), $D_2$ = 2nd Depth (intermediate) and $D_3$ = 3rd Depth (Deep)

Traverse A profile patterns were similar and fairly parallel. The resistivity varied slightly along the traverse and was for most parts, constant. The resistivity decreased across depth slightly from $D_1$ –$D_2$ and increased sharply from $D_2$ - $D_3$. There was no resistivity drop observed over the borehole position. Traverse B profile patterns were also similar and fairly parallel. There was a slight general decrease in resistivity to the NW along the traverse. Resistivity was observed to increase with depth sharply from $D_2$ - $D_3$. There was no observed resistivity drop over the borehole position.

The Schlumberger array resistivity values ranged between 1.67 – 31.75 Ωm. Traverse B had comparatively higher values while Traverse A had the wider range. Profile patterns for both traverses were different. The profile plots are shown in figure 4.1.1b.

Traverse A profile patterns were similar and fairly parallel. The resistivity along the traverse varied sharply, with a general decrease to the NE. The resistivity was however observed to increase with depth, more sharply from $D_2$ - $D_3$. A drop in resistivity was observed over the borehole position. Traverse B profile patterns were also similar, but not parallel. The resistivity decreased sharply along the traverse from an observed high in the SE to uniform in the NW. The resistivity also increased across depth, but this was not consistent throughout the traverse. There was no drop in resistivity over the borehole position.

The dipole-dipole array resistivity values ranged between 1.6 – 36.3 Ωm. The resistivity values were similar for both traverses. Profile patterns were however different. The profile plots are shown in figure 4.1.1c.

Traverse A profile patterns were similar but only parallel for $D_2$ and $D_3$. The resistivity was seen to decrease from observed high at the end of the traverse toward the middle part.

Resistivity decreased across depth from $D_1$ - $D_2$ and increased sharply from $D_2$ - $D_3$. There was no observed drop in resistivity over the borehole position. Traverse B profile patterns had some semblance, but were not parallel. The resistivity along traverse varied slightly, more pronounced in $D_2$ and $D_3$. The resistivity however increased sharply with depth. There was no drop in resistivity over the borehole position.

Wenner and Schlumberger profile patterns were similar for Traverse A, but less so for Traverse B. Dipole-Dipole array profile patterns for Traverse B were more similar to the other two arrays. Traverse A profile patterns were however different.

4.1.2 REN-02

The Wenner array resistivity values ranged between 4.71 – 92.24 Ωm. The resistivity values were fairly similar for both traverses. However, profile patterns were different. The profile plots are shown in figure 4.1.2a.

Traverse A profile patterns were similar and parallel for $D_1$ and $D_2$. $D_3$ was different. Resistivity decreased from an initial high at the NE and SW towards the middle of the traverse. The resistivity along $D_3$ was fairly uniform. The resistivity was observed to decrease across depth. There was a pronounced drop in resistivity over the borehole position. This was only observed in $D_1$ and $D_2$. Traverse B profile pattern were also similar for $D_1$ and $D_2$. They were however not parallel. $D_3$ was also different. The resistivity was observed to increase sharply towards the NW along the traverse for $D_1$ and $D_2$.. $D_3$ was fairly constant along the traverse. There was no drop in resistivity over the borehole position.

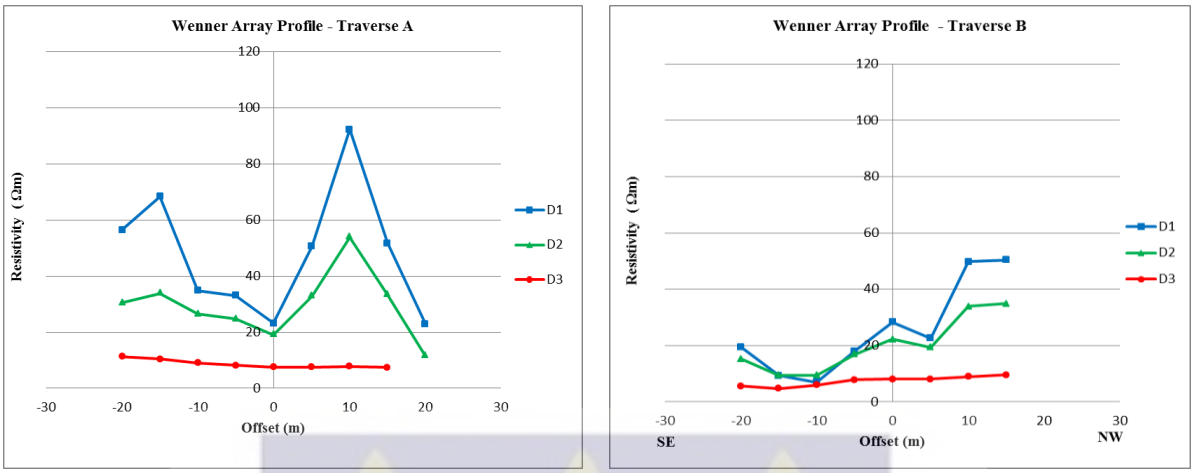


Figure 4.1.2a Wenner Array Profiles for REN-02 (SW-NE for Traverse A, SE-NW for Traverse B)

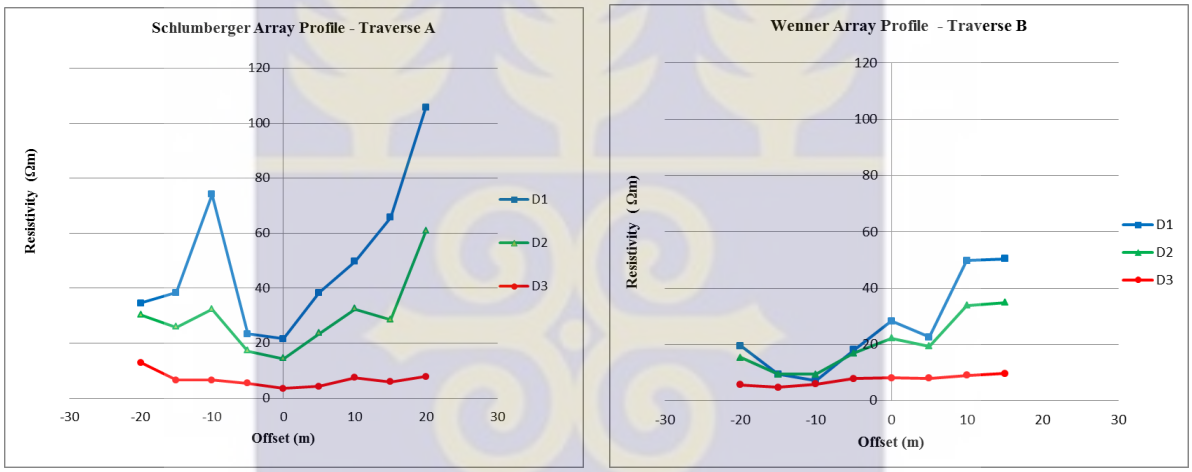


Figure 4.1.2b Schlumberger Array Profiles for REN-02 (SW-NE for Traverse A, SE-NW for Traverse B)

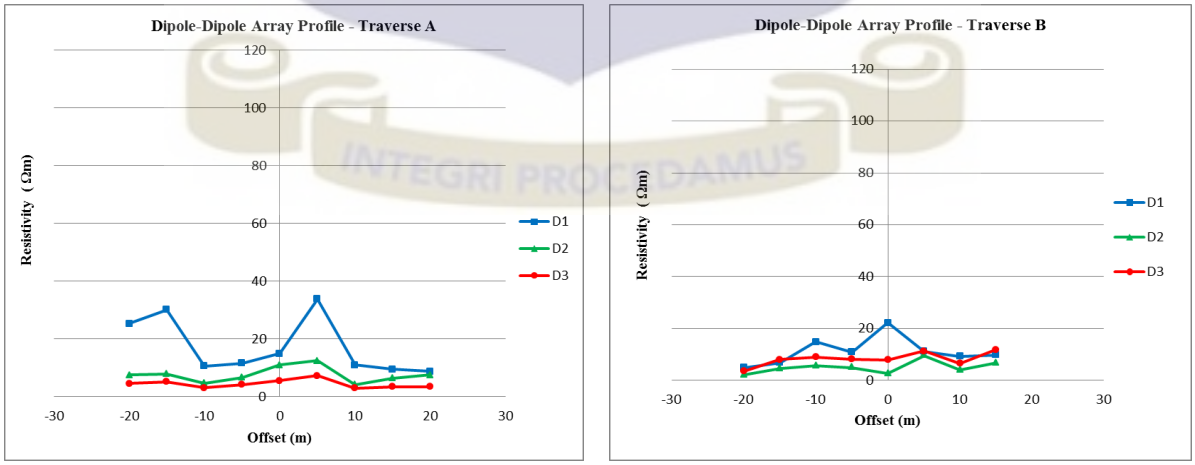


Figure 4.1.2c Dipole-Dipole Array Profiles for REN-02 (SW-NE for Traverse A, SE-NW for Traverse B)

Where $D_1$ = 1st Depth (Shallow), $D_2$ = 2nd Depth (intermediate) and $D_3$ = 3rd Depth (Deep)

The Schlumberger array resistivity array values ranged between 3.6 – 105.7 Ωm. Traverse A had the higher values. Profile patterns for both traverses were different. The profile plots are shown in figure 4.1.2b

Traverse A profile patterns were fairly similar but not parallel for $D_1$ and $D_2$. $D_3$ was different. The resistivity was observed to increase sharply toward the NE. $D_3$ was fairly constant along the traverse. The resistivity however decreased with depth. There was a pronounced drop in resistivity over the borehole position. Traverse B profile patterns were also fairly similar for $D_1$ and $D_2$ but not parallel. The resistivity decreased sharply toward the NW. Resistivity was however constant along $D_3$. The resistivity also decreased with depth. This was more pronounced in the NW. There was no observed resistivity drop over the borehole position.

The dipole-dipole array resistivity values ranged between 2.63 – 33.9 Ωm. The resistivity values were similar for both traverses. Profile patterns were however different. The profile plots are shown in figure 4.1.2c.

Traverse A profile patterns were similar and parallel for $D_2$ and $D_3$. $D_1$ was erratic and different. The resistivity variation along traverse was gentle. The resistivity decreased across depth, and sharply so for $D_1$ - $D_2$. There was an observed drop in resistivity over the borehole position. Traverse B profile pattern were also similar and parallel for $D_2$ and $D_3$. The resistivity along the traverse for $D_3$ was erratic. Resistivity also varied sharply along traverse for $D_2$ and $D_3$, but there was a general increase toward the NW. There was a slight drop in resistivity over the borehole position.

Profile patterns for Wenner and dipole-dipole arrays were very similar for Traverse A. Schlumberger array profile pattern was less so. Traverse B profile patterns were however similar for Wenner and Schlumberger arrays but differed for dipole-dipole array.

4.1.2 REN-03

The Wenner array resistivity values ranged between 10.3 – 716.3 Ωm. The resistivity values were high for Traverse A but Traverse B had the wider range. Profile patterns for both traverses were different. The profile plots are shown in figure 4.1.3a.

Traverse A profile patterns were similar and fairly parallel. The resistivity varied gently along the traverse and decreased sharply to the NE. The resistivity increased with depth. There was no observed drop in resistivity over the borehole position. Traverse B profile patterns were less similar and erratic. The resistivity decreased sharply toward the NW for $D_1$ and $D_2$. $D_3$ showed a consistent increase toward the NW. There was no resistivity drop over the borehole position.

The Schlumberger array resistivity values ranged between 43.49 – 659 Ωm. Traverse A had the higher values and Traverse B, the wider range. Profile patterns were different. The profile plots are shown in figure 4.1.3b.

Traverse A profile patterns were similar and fairly parallel. The resistivity increased generally to the NE and decreased across depth. There was a slight drop in resistivity over the borehole position. Traverse B profile patterns were also less similar but more erratic. The resistivity however decreased sharply toward the NW for $D_1$ and $D_2$. $D_3$ showed an increase along the traverse. The resistivity across depth was inconsistent and ill-defined.

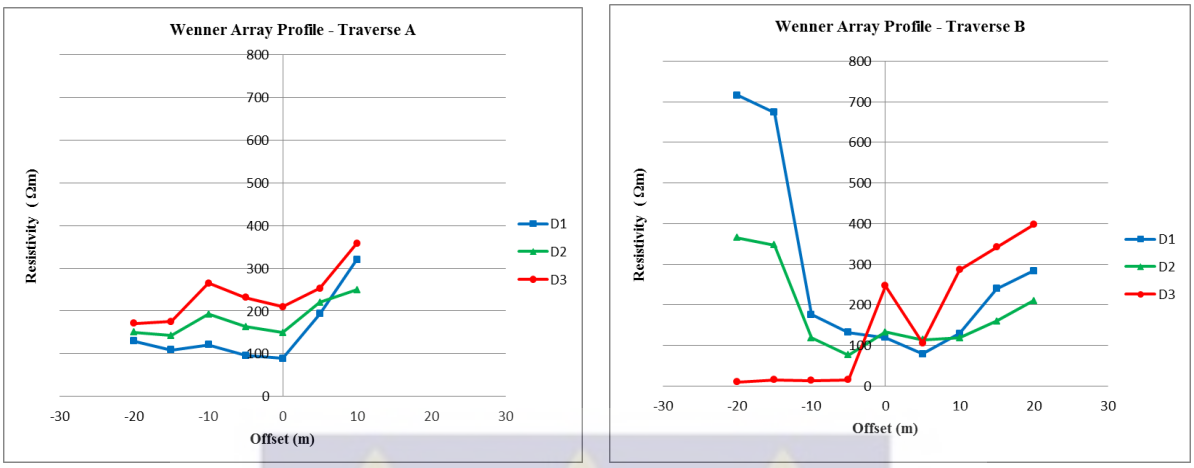


Figure 4.1.3a Wenner Array Profiles for REN- 03 (SW-NE for Traverse A, SE-NW for Traverse B)

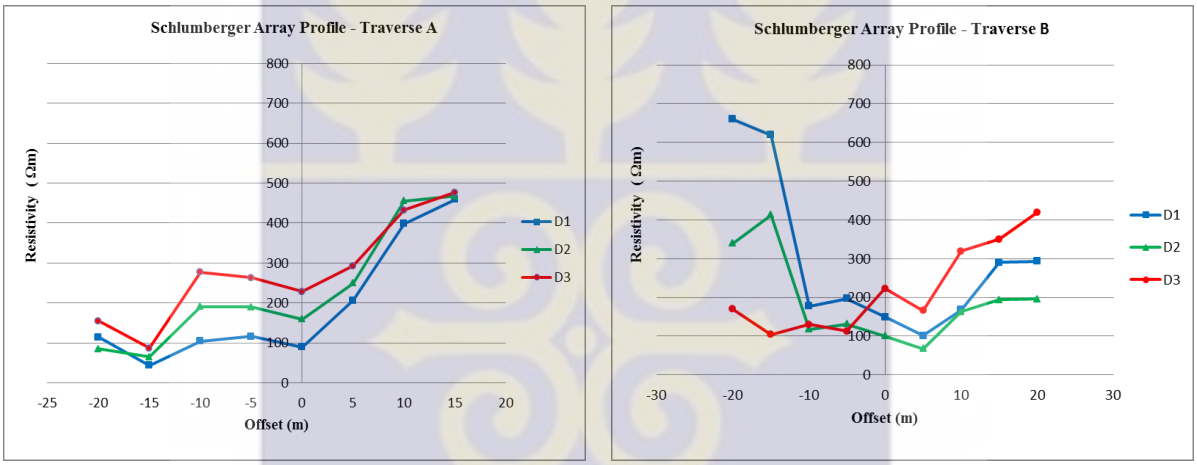


Figure 4.1.3b Schlumberger Array Profiles for REN- 03(SW-NE for Traverse A, SE-NW for Traverse B)

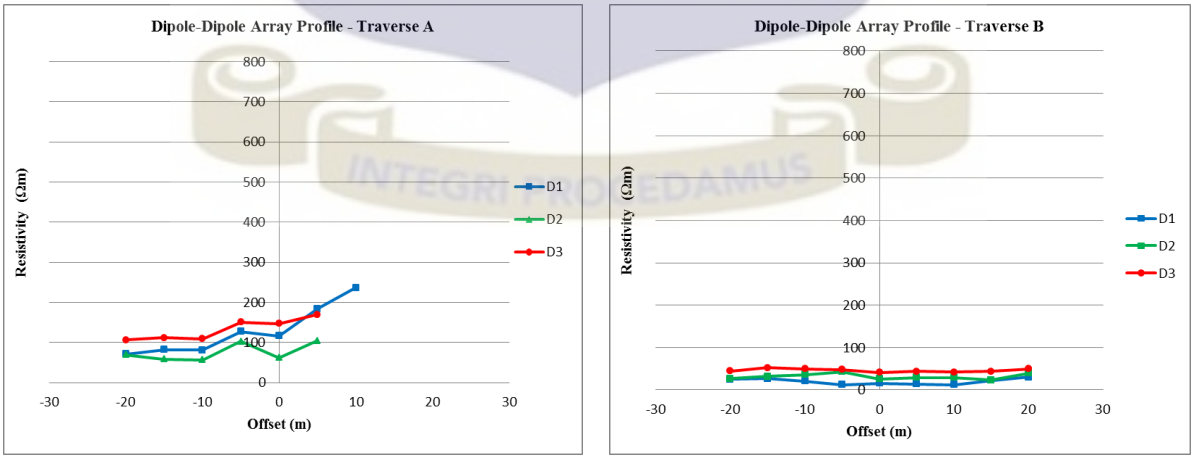


Figure 4.1.3c Dipole-Dipole Array Profiles for REN- 03 (SW-NE for Traverse A, SE-NW for Traverse B)

Where $D_1$ = 1st Depth (Shallow), $D_2$ = 2nd Depth (intermediate) and $D_3$ = 3rd Depth (Deep)

There was no drop in resistivity over the borehole position.

The dipole-dipole array resistivity values ranged between 11.96 – 236.2 Ωm. Traverse A had both the higher values and the wider range. Profile patterns were however different for both traverses. The profile plots are shown in figure 4.1.3c.

Traverse A profile patterns were similar and fairly parallel. The resistivity increased along the traverse toward the NE. The resistivity decreased across depth from $D_1$ - $D_2$ and increased sharply from $D_2$ – $D_3$. There was a drop in resistivity over the borehole position. Traverse B profile patterns were similar and fairly parallel. The resistivity along the traverse was inconsistent and showed sharp variations. The resistivity also increased sharply across depth. There was no drop in resistivity over the borehole position.

Profile patterns for Traverse A were similar for Wenner and Schlumberger arrays, but less so for dipole-dipole array. Traverse B profile patterns were also similar for Wenner and Schlumberger arrays. Dipole-Dipole array pattern was different.

4.1.4 REN-04

The Wenner array resistivity values ranged between 100 – 819.8Ωm. The Traverse A values were relatively higher compared to Traverse B. The traverses had different profile patterns. The profile plots are shown in figure 4.1.4a.

Profile pattern for Traverse A were similar across depth, and increased sharply toward the Northeastern end of the Traverse. There was no pronounced drop over the borehole position across depth. Profile pattern for Traverse B were similar for $D_1$ and $D_2$ only. The resistivity trend across depth was ill-defined, with some parts showing constant increase and others,

constant decrease. There was no general trend along traverse. There was no drop over the borehole position. The resistivity variation was sharp.

The Schlumberger array resistivity values ranged between 71.9 – 792.7Ωm. Traverse A resistivity values were much higher than Traverse B. The profile plots are shown in figure 4.1.4b.

Traverse A profile patterns were similar but not parallel across depth. There was an observed increase in resistivity towards the northeastern end of the profiles. The resistivity was observed to constantly decrease with depth. Resistivity variation was sharp along the traverse, and there was no drop in resistivity over the borehole position. Profile patterns for Traverse B were similar and parallel across depth. There was a general increase along traverse for the first part, and a sharp decrease after the borehole position to the NW. There was constant decrease in resistivity with depth with almost similar values in the northwestern part. Variation in the resistivity was sharp.

The dipole-dipole array resistivity values ranged between 2.799 – 309.55Ωm. Traverses A and B generally had similar values. The low values were however observed in the $D_2$ of Traverse A. The profile plots are shown in figure 4.1.4c.

Traverse A pattern were somewhat similar, but not parallel across depth. The resistivity increased with depth for the first half of the traverse, and decreased for the other half toward the NE. This part showed a sharp drop in $D_2$ values with corresponding sharp increases in $D_1$ and $D_3$. There was however no drop over the borehole position. Profile patterns for Traverse B were not similar and parallel across depth. The resistivity trends across depth and along traverse were both ill-defined with no regular pattern. The resistivity variations were sharp.

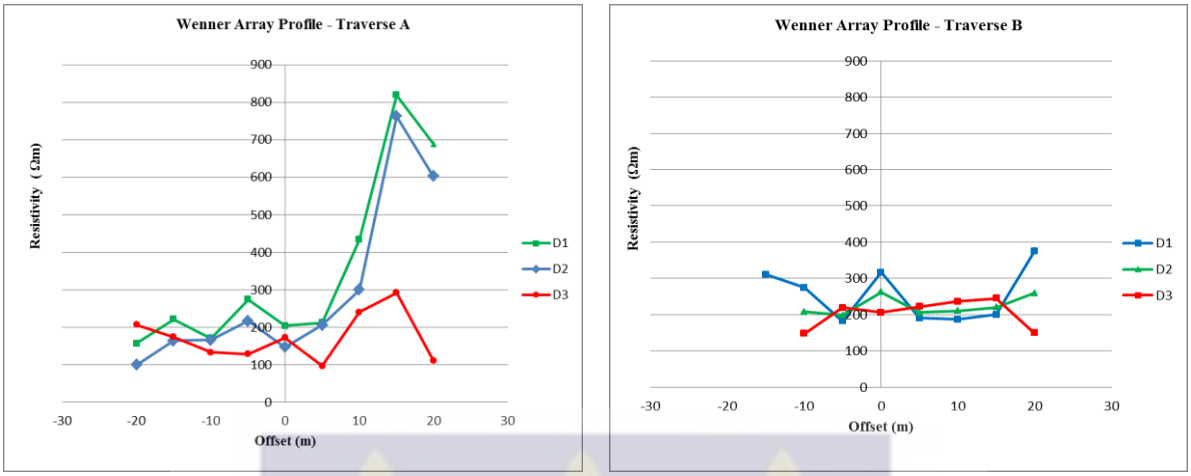


Figure 4.1.4a Wenner Array Profiles for REN-04 (SW-NE for Traverse A, SE-NW for Traverse B)

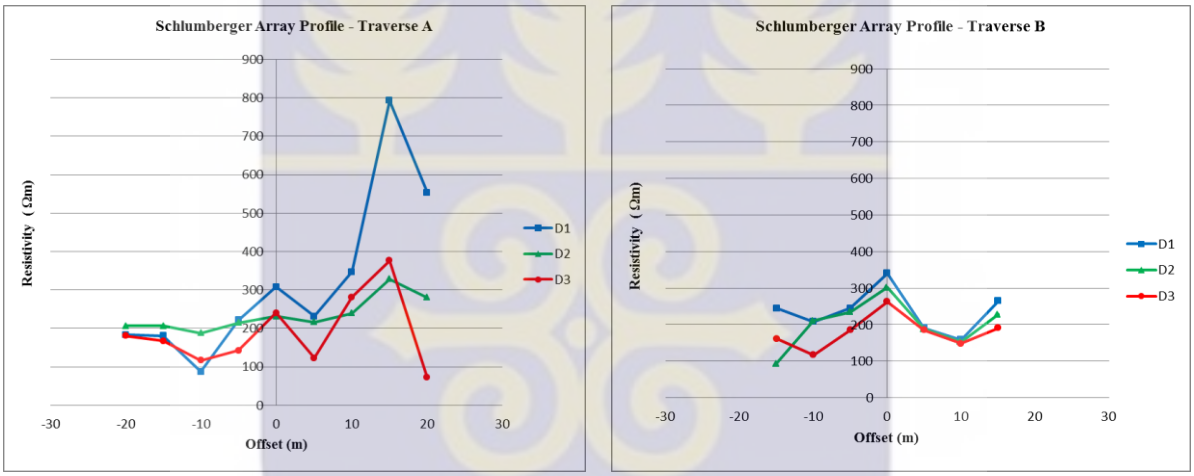


Figure 4.1.4b Schlumberger Array Profiles for REN-04 (SW-NE for Traverse A, SE-NW for Traverse B)

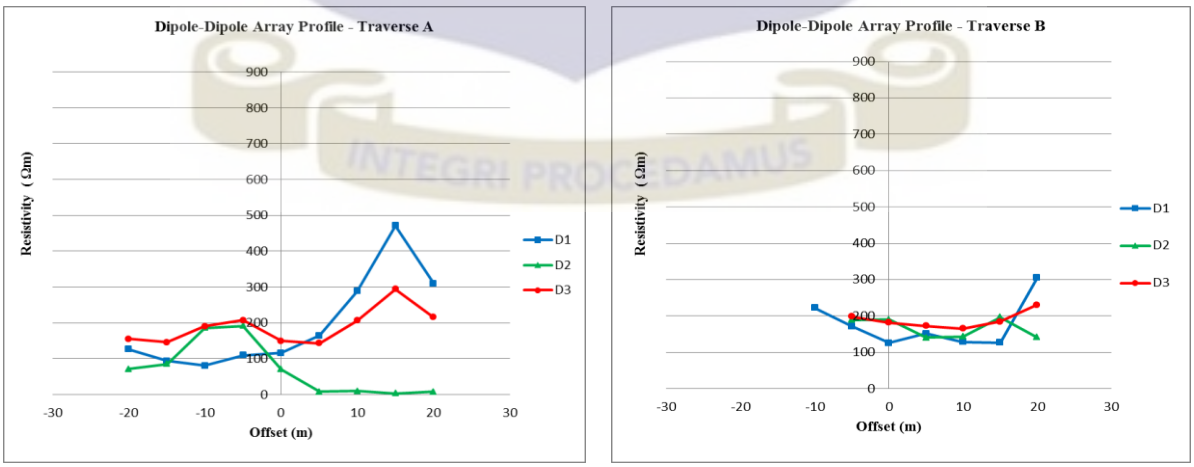


Figure 4.1.4c Dipole-Dipole Array Profiles for REN-04 (SW-NE for Traverse A, SE-NW for Traverse B)

Where $D_1$ = 1st Depth (Shallow), $D_2$ = 2nd Depth (intermediate) and $D_3$ = 3rd Depth (Deep)

The resistivity patterns for Wenner and Schlumberger arrays were similar for Traverse A but differed for Traverse B. Dipole-Dipole array patterns were somewhat similar to the Wenner and Schlumberger patterns for Traverse A, but were ill-defined. Traverse B was inconsistent with the other two.

### 4.1.5 REN-05

The Wenner array resistivity values ranged between 35.1 – 585.1Ωm. Traverse A showed the wider range in resistivity with Traverse B, having the higher values. Profile patterns for both traverses were different. Figure 4.1.5a shows the profile plots.

Traverse A profile patterns were similar but not parallel. The resistivity increased consistently along the traverse toward the NE. Resistivity also increased across depth for the first half of the traverse and decreased for the rest toward the NE. However, similar resistivity across depth was observed for $D_1$ and $D_2$ in parts of the traverse. There was a resistivity drop over the borehole position. This was not observed in $D_3$. Traverse B profile patterns were similar but not parallel. The resistivity along traverse and across depth was ill-defined. There was however a pronounced drop in resistivity over the borehole position. This was consistent across depth.

The Schlumberger array resistivity values ranged between 31.8 – 747.6 Ωm. Similarly, Traverse A had the wider range, with Traverse B showing the higher values. Profile patterns for both traverses were different. Figure 4.1.5b shows the profile plots.

Traverse A profile patterns were similar but not parallel. Resistivity decreased sharply along traverse toward the NE. There was no drop in resistivity over the borehole position.

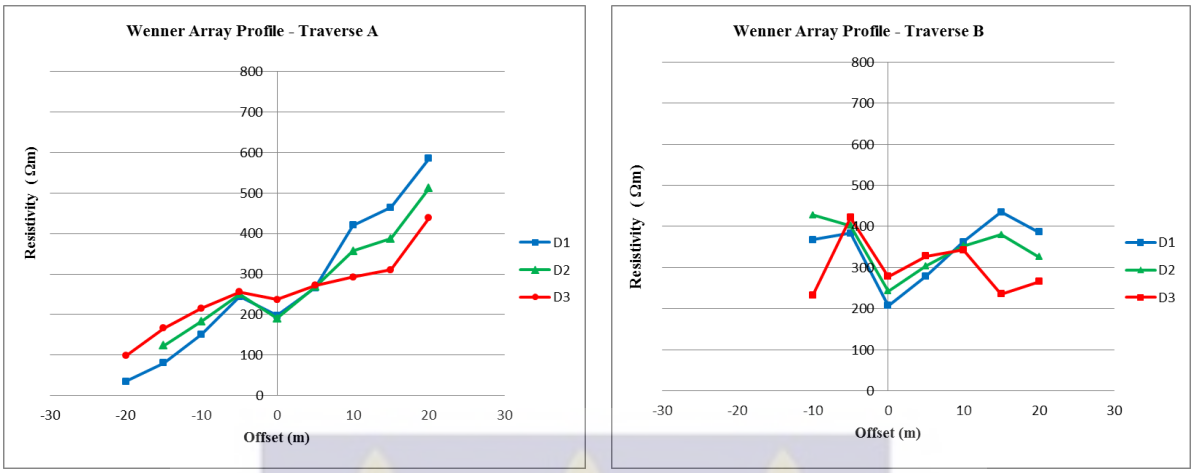


Figure 4.1.5a Wenner Array Profiles for REN-05(SW-NE for Traverse A, SE-NW for Traverse B)

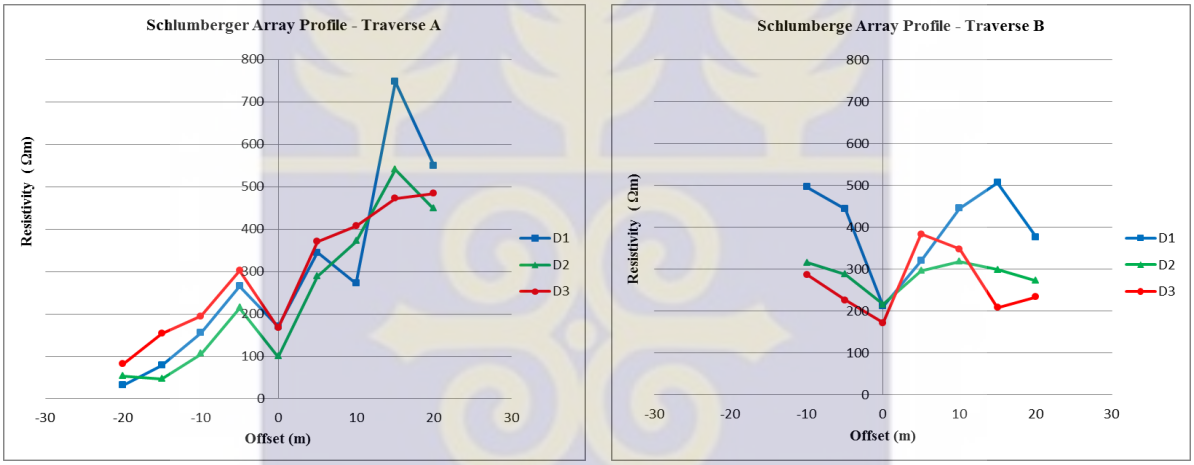


Figure 4.1.5b Schlumberger Array Profiles for REN-05 (SW-NE for Traverse A, SE-NW for Traverse B)

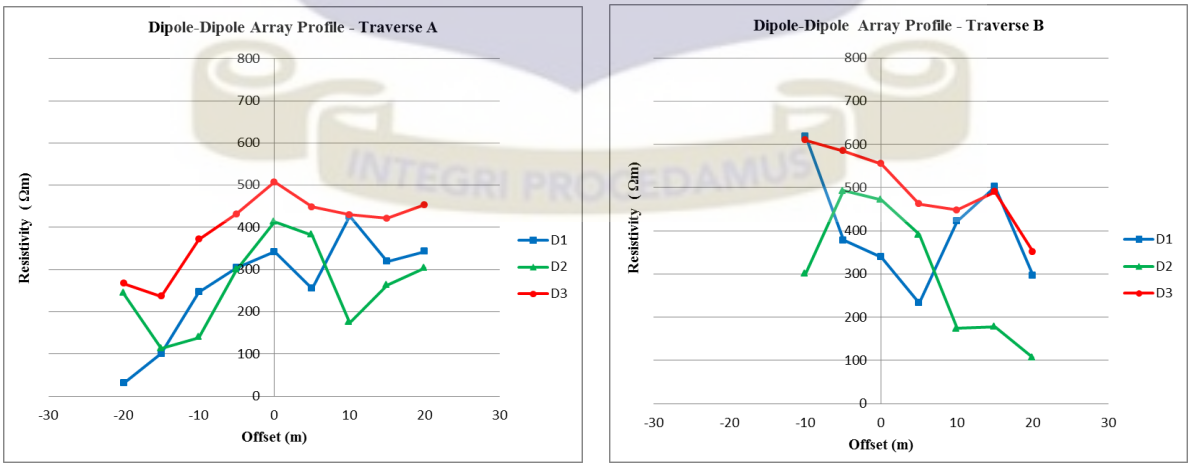


Figure 4.1.5c Dipole-Dipole Array Profiles for REN-05 (SW-NE for Traverse A, SE-NW for Traverse B)

Where $D_1$ = 1st Depth (Shallow), $D_2$ = 2nd Depth (intermediate) and $D_3$ = 3rd Depth (Deep)

The resistivity decreased across depth from $D_1 - D_2$ and was increased sharply for $D_2 - D_3$. Traverse B profile patterns were fairly similar but not parallel. The resistivity along the traverse was inconsistent, varying sharply toward the NE. The resistivity generally decreased with depth. There was a drop in resistivity over the borehole position. This was observed across depth.

The dipole-dipole array resistivity values ranged between 30.7 – 507.55Ωm. Similarly, Traverse A had the wider range and Traverse B, the higher values. Profile patterns were different for both traverses. Figure 4.1.5c shows the profile plots.

Traverse A profile patterns were not similar and parallel. The resistivity variations were sharp along the traverse. The resistivity generally increased to the NE. The resistivity across depth was largely inconsistent. Traverse B profile patterns were similar and parallel for $D_1$ and $D_3$. $D_2$ was different. Resistivity generally decreased toward the NW for $D_1$ and $D_3$. The resistivity across depth was also inconsistent. There was no observed drop in resistivity over the borehole position.

Wenner and Schlumberger arrays had similar profile patterns for both traverses. Schlumberger array patterns were however characterized by sharper variation. Dipole-Dipole array profile patterns were not similar to that of the other two arrays for both traverses.

4.1.6 REN-06

The Wenner array resistivity values ranged between 8.31 – 319.2 Ωm. Traverse A had the wider range but Traverse B had the higher values. Profile patterns for both traverses were different. Figure 4.1.6a shows the profile plots.

Traverse A profile patterns were similar but not parallel. The resistivity along the traverse showed a general decrease toward the NE. Resistivity was high and uniform to the SW before dropping sharply to and largely uniform low resistivity NE. This was consistent in all the profiles. Resistivity across depth decreased from $D_1 – D_2$ and increased for $D_2 – D_3$. There was no resistivity drop over the borehole position. Traverse B profile patterns were similar for $D_1$ and $D_2$ but not parallel. $D_3$ was different. The resistivity along the traverse for $D_1$ and $D_2$ increased for the first half of the traverse and decreased sharply to the NW. $D_3$ did not show much variation. The resistivity however decreased with depth. There was no distinct drop in resistivity over the borehole position.

The Schlumberger array resistivity values ranged between 3.42 – 301.5 Ωm. Similarly, Traverse A had the wider range and Traverse B, the higher values. Figure 4.1.6b shows the profile plots.

Traverse A profile patterns were also similar and fairly parallel. The resistivity along the traverse decreased sharply from an initial high to the SW towards the NE. Resistivity varied sharply along the traverse. Resistivity decreased across depth from $D_1 – D_2$ and increased from $D_2 – D_3$. There was no drop in resistivity over the borehole position. Traverse B profile patterns were similar for $D_1$ and $D_2$, but not parallel. The resistivity along traverse was inconsistent, decreasing to the NW from an initial high to the SE.

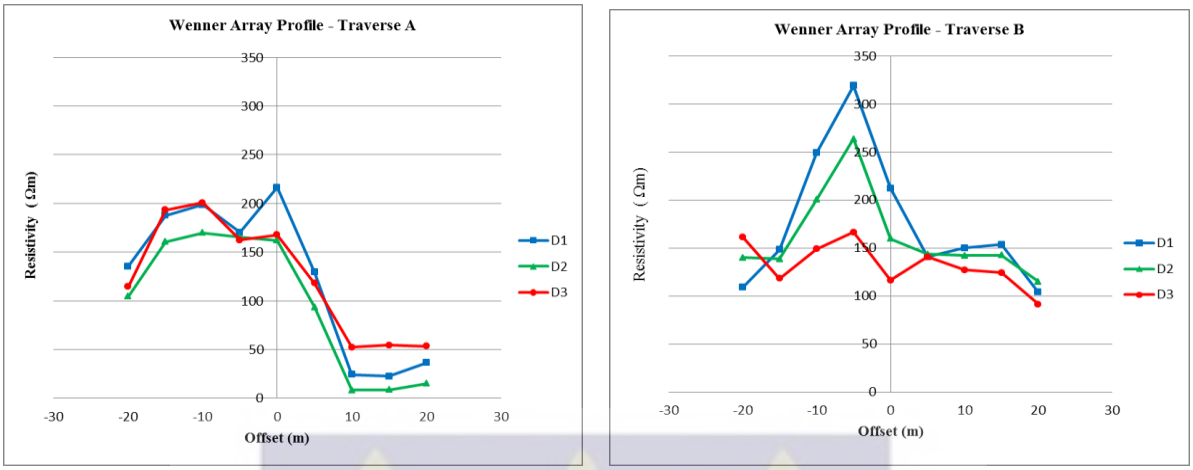


Figure 4.1.6a Wenner Array Profiles for REN-06 (SW-NE for Traverse A, SE-NW for Traverse B)

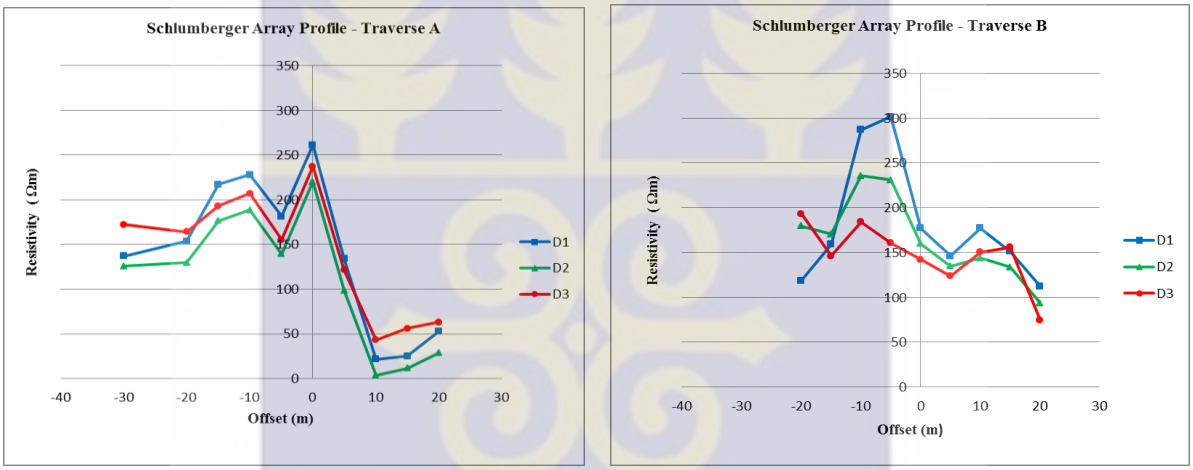


Figure 4.1.6b Schlumberger Array Profiles for REN-06 (SW-NE for Traverse A, SE-NW for Traverse B)

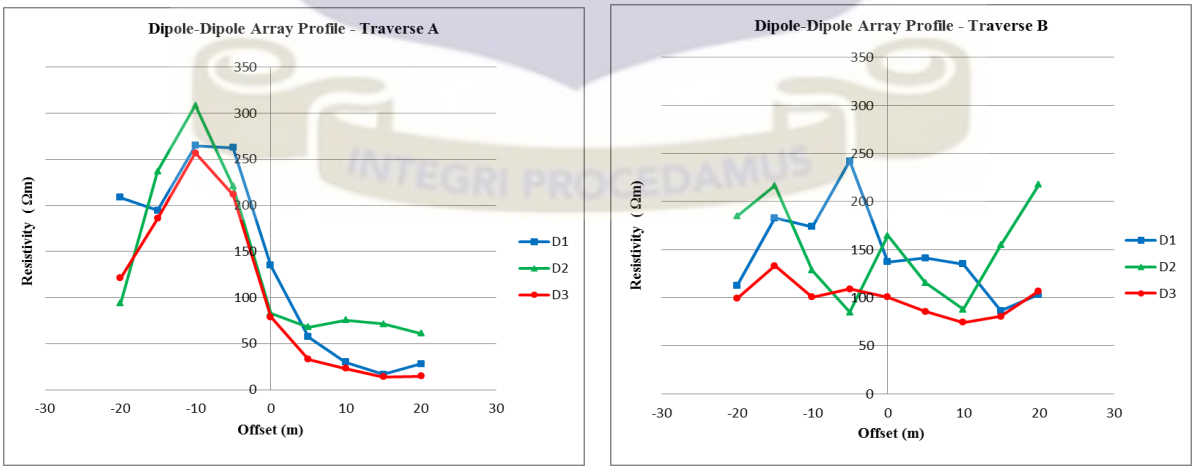


Figure 4.1.6c Dipole-Dipole Array Profiles for REN-06 (SW-NE for Traverse A, SE-NW for Traverse B)

Where $D_1$ = 1st Depth (Shallow), $D_2$ = 2nd Depth (intermediate) and $D_3$ = 3rd Depth (Deep)

Resistivity decreased across depth. There was no drop in resistivity over the borehole position.

The dipole-dipole array resistivity values ranged between 8.31 – 319.2 Ωm. Similarly, Traverse A had the wider range and Traverse B, the higher values. Profile patterns for both traverses were different.

Traverse A profile pattern were similar but not parallel. Resistivity was observed to increase in the SW before decreasing sharply to uniform values in NE. The resistivity across depth was inconsistent increasing from $D_1$ – $D_2$ and decreasing from $D_2$ – $D_3$ to the NE and SW. There was no observed drop in resistivity over the borehole position. Traverse B profile patterns were not similar and parallel. The resistivity along the traverse decreased generally for $D_1$ and $D_3$. Resistivity along $D_2$ varied sharply. Resistivity however decreased with depth. There was no observed drop in resistivity over the borehole position.

Profile patterns for traverse A were very similar for all three arrays. Traverse B profile patterns were similar for Wenner and Schlumberger arrays. Dipole-Dipole array profile patterns were fairly similar for $D_1$ and $D_3$. $D_2$ was mostly erratic.

4.1.7 REN-07

The Wenner array resistivity values ranged between 12.51 – 657.9 Ωm. Traverse A had the higher values, but traverse B had the wider range. Profile patterns were however fairly similar for both traverses. Figure 4.1.7a shows the profile plots.

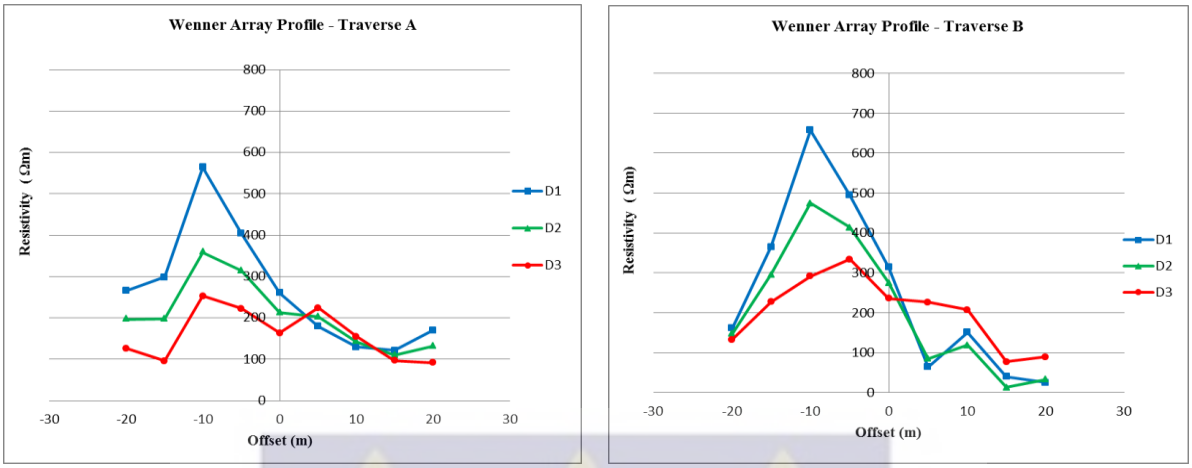


Figure 4.1.7a Wenner Array Profiles for REN-07 (SW-NE for Traverse A, SE-NW for Traverse B)


Figure 4.1.7b Schlumberger Array Profiles for REN-07 (SW-NE for Traverse A, SE-NW for Traverse B)

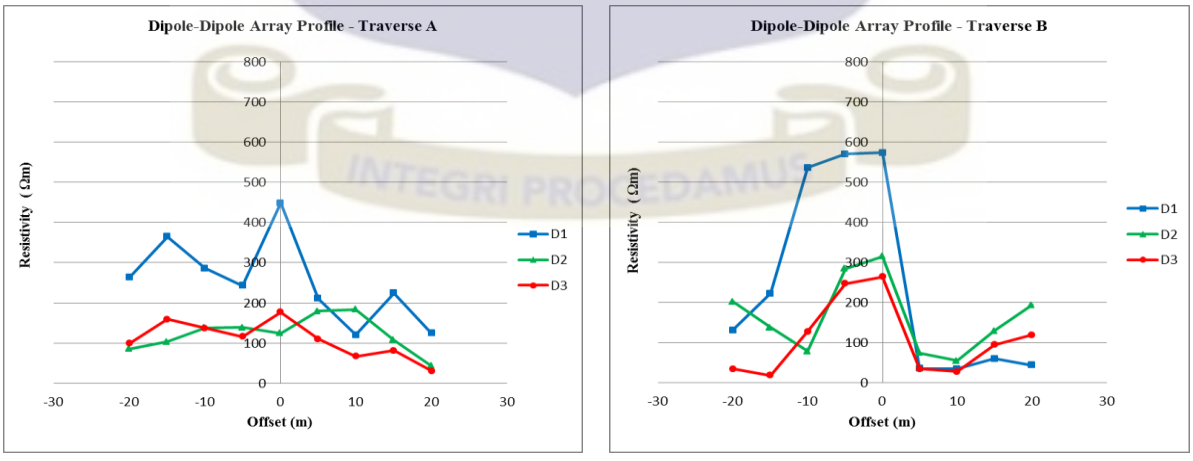


Figure 4.1.7c Dipole-Dipole Array Profiles for REN-07 (SW-NE for Traverse A, SE-NW for Traverse B)

Where $D_1$ = 1st Depth (Shallow), $D_2$ = 2nd Depth (intermediate) and $D_3$ = 3rd Depth (Deep)

Profile pattern for Traverse A were similar but not parallel. Resistivity decreased sharply from an initial high in the SW toward the NE. This was more prominent in $D_1$. The resistivity across depth was inconsistent along the traverse, but a general decrease was observed to the SW. Similar resistivity was observed to the NE across depth. There was no observed drop in resistivity over the borehole position. Profile patterns for Traverse B were similar, but not parallel. Resistivity was generally high to the SE but decreased sharply to the NW. This was also most prominent in $D_1$. The resistivity decreased across depth to the SE but increased to the NW. There was however no observed drop in resistivity over the borehole position.

Schlumberger array resistivity values ranged between 61.07 – 643.8 Ωm. Similarly, Traverse A had the higher values and Traverse B, the wider range. The profile patterns for both traverses were fairly similar. Figure 4.1.7b shows the profile plots.

Traverse A profile patterns were similar and not parallel. The resistivity showed a general decrease toward the NE. Resistivity was more erratic and the trend less obvious. This was observed in $D_1$, $D_2$ and $D_3$. The resistivity showed a general decrease with depth, much more defined to the SW. There was no observed resistivity drop over the borehole position. Traverse B profile patterns were similar and fairly parallel, except to the NW. resistivity was a pronounced high to the SE but decreased sharply along traverse to the NW. Resistivity also decreased with depth for large parts of the traverse. There was no resistivity drop over the borehole position.

The dipole-dipole resistivity values ranged between 12.51 – 657.9 Ωm. Similarly, Traverse A had the higher values, and Traverse B having the wider range. Profile patterns for both traverses were less similar. Figure 4.1.7c shows the profile plots.

Profile patterns for Traverse A were not similar and parallel, but erratic. $D_1$ showed a general decrease in resistivity toward the NE. $D_2$ and $D_3$ had almost imperceptible decreases. Resistivity however, decreased across depth. There was no drop in resistivity over the borehole position. Profile patterns for Traverse B were more similar, and fairly parallel. There was also a general resistivity high to the SE which decreased sharply to the NW. Resistivity decreased with depth to the se but was ill-defined to the NW. The variations were less erratic. There was no observed drop over the borehole position.

Wenner and Schlumberger array profile patterns were fairly similar for both Traverses A and B. Dipole-Dipole array profile patterns were less similar for Traverse A, but more so for Traverse B.

4.1.8 REN-08

The Wenner array resistivity values ranged between 25.4 - 494 Ωm. Traverse A had the wider range with Traverse B having the higher values. Profile patterns for both traverses were different. Figure 4.1.8a shows the profile plots.

Profile patterns for Traverse A were similar, but parallel for only $D_2$ and $D_3$. The resistivity along traverse for $D_2$ and $D_3$ was uniform. $D_1$ however showed a decrease toward the NE. The resistivity increased with depth for the NW and decreased for the SW. There was a drop in resistivity over the borehole position. This was more prominent in $D_1$. Profile patterns for Traverse B were similar and parallel. Resistivity decreased generally towards the NW and increased across depth. There was also a drop in resistivity over the borehole position, observed across depth.

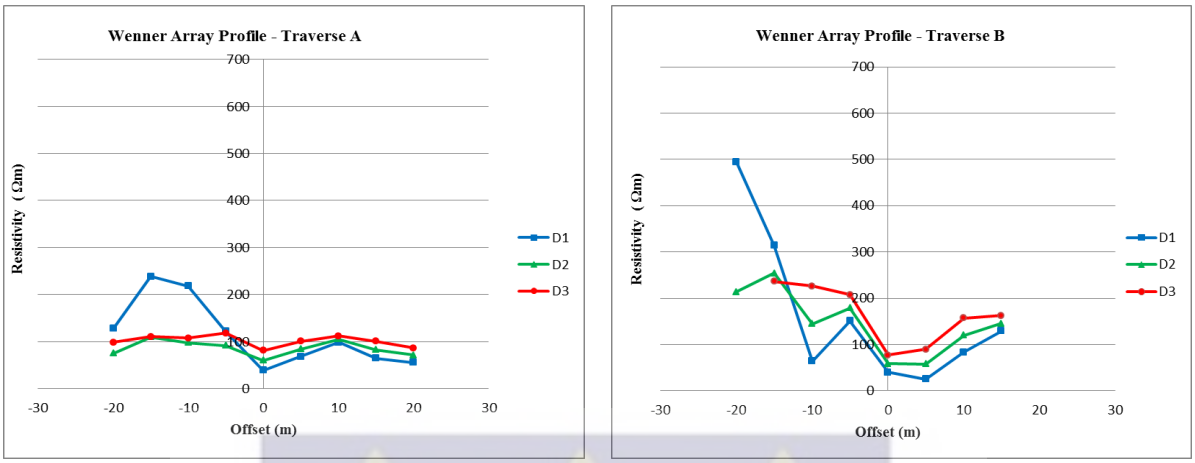


Figure 4.1.8a Wenner Array Profiles for REN-08 (SW-NE for Traverse A, SE-NW for Traverse B)

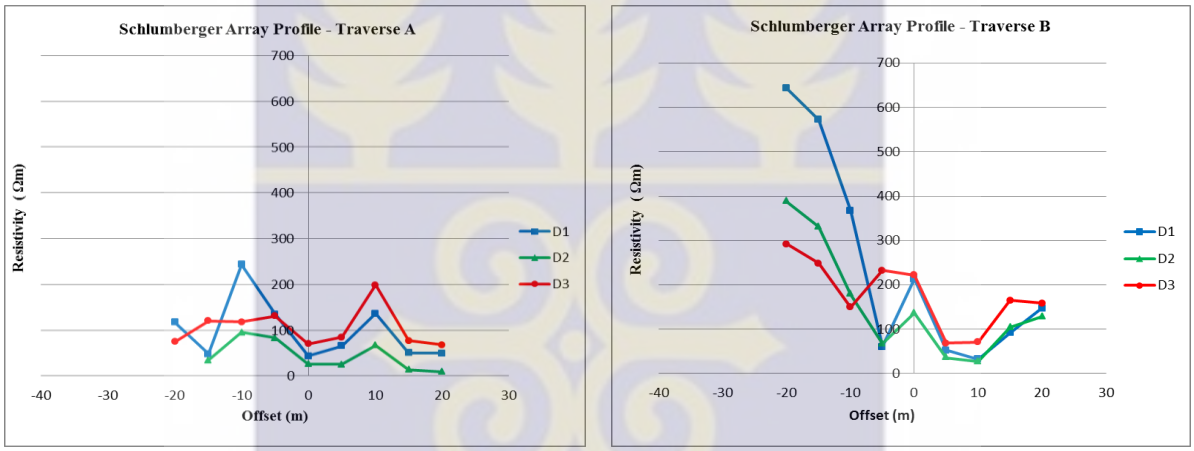


Figure 4.1.8b Schlumberger Array Profiles for REN-07 (SW-NE for Traverse A, SE-NW for Traverse B)

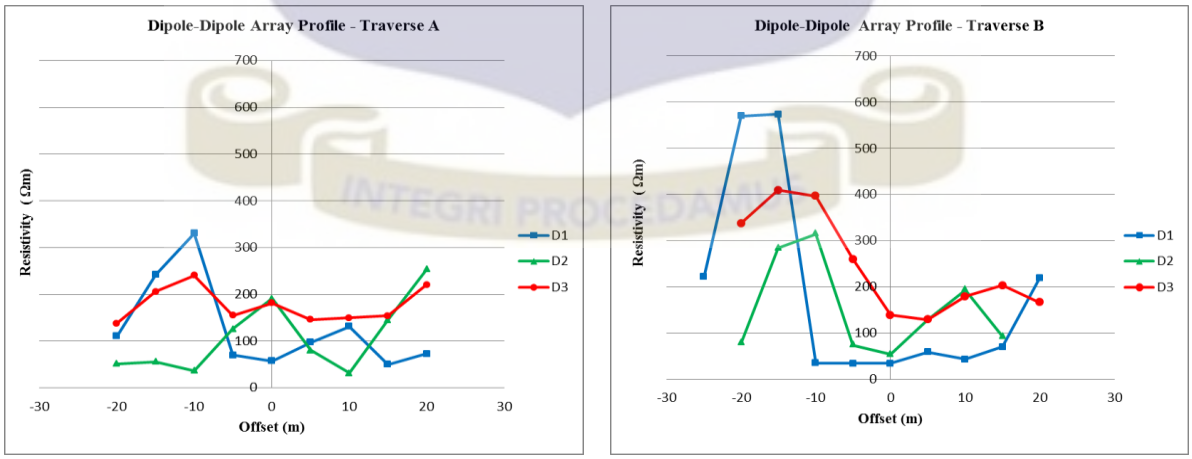


Figure 4.1.8c Dipole-Dipole Array Profiles for REN-08 (SW-NE for Traverse A, SE-NW for Traverse B)

Where $D_1$ = 1st Depth (Shallow), $D_2$ = 2nd Depth (intermediate) and $D_3$ = 3rd Depth (Deep)

The Schlumberger array resistivity values ranged between 8.86 – 643.8 Ωm. Traverse B had both the wider range and the higher values. Profile patterns were different for both traverses. Figure 4.1.8b shows the profile plots.

Profile patterns for Traverse A were similar, and not parallel. The resistivity along the traverse was erratic and the trend, ill-defined. The resistivity however decreased across depth from $D_1 - D_2$ and increased for $D_2 - D_3$. There was a drop in resistivity over the borehole position. This was observed across depth. Profile patterns for Traverse B were similar and fairly parallel. Resistivity along the traverse showed a general decrease toward the NW. The resistivity trend across depth was inconsistent for, but there was an observed increase from $D_2 - D_3$. There was no drop in resistivity over the borehole position.

The dipole-dipole array resistivity values ranged between 34.6 – 573.4 Ωm. Of the two, Traverse B had both the wider range and the higher values. Profile patterns were different for both traverses. Figure 4.1.8c shows the profile plots.

Profile patterns for Traverse A were not similar and parallel. The resistivity trends were ill-defined and erratic along the traverse and also across depth. There was no observed resistivity drop over the borehole position. Profile patterns for Traverse B were fairly similar and not parallel. Resistivity generally increased toward the NW and decreased with depth. A drop in resistivity was observed in $D_3$ and $D_2$. $D_1$ did not show this.

Wenner and Schlumberger array profile patterns were similar for Traverse B, but less so for Traverse A. Dipole-Dipole array profile patterns were different for traverses, compared to that of the other two arrays.

4.1.9 REN-09

The Wenner array resistivity values ranged between 29.35 – 602.4 Ωm. Resistivity values were similar for both Traverses A and B. Profile patterns were also similar for both traverses. Figure 4.1.9a shows the profile plots.

Traverse A profile patterns were similar and fairly parallel. High resistivity was observed at the traverse ends, which decreased sharply toward the middle parts. The resistivity decreased with depth. There was a pronounced drop in resistivity over the borehole position. Traverse B profile pattern were similar and fairly parallel. Similarly, high resistivity was observed at the ends of the traverse and decreased sharply towards the middle parts. The resistivity across depth decreased for $D_1$ - $D_2$ and increased for $D_2$ – $D_3$. There was a pronounced drop in resistivity over the borehole position. This was consistent across depth.

The Schlumberger array resistivity values ranged between 42.87 – 642.9 Ωm. The resistivity values were fairly similar for both Traverses A and B. Profile patterns were also similar. Figure 4.1.9b shows the profile plots.

Traverse A profile patterns were similar and fairly parallel. The resistivity was observed to be high at both ends of the traverse and decreased sharply towards the middle parts. Resistivity was similar for $D_1$, $D_2$ and $D_3$. The resistivity generally decreased across depth. There was a pronounced drop in resistivity over the borehole position. Traverse B profile patterns were similar and parallel. The resistivity was also high at the traverse ends and decreased sharply towards the middle parts. Resistivity however decreased across depth from $D_1$ – $D_2$ and increased from $D_2$ – $D_3$. There was also a pronounced drop in resistivity over the borehole position.

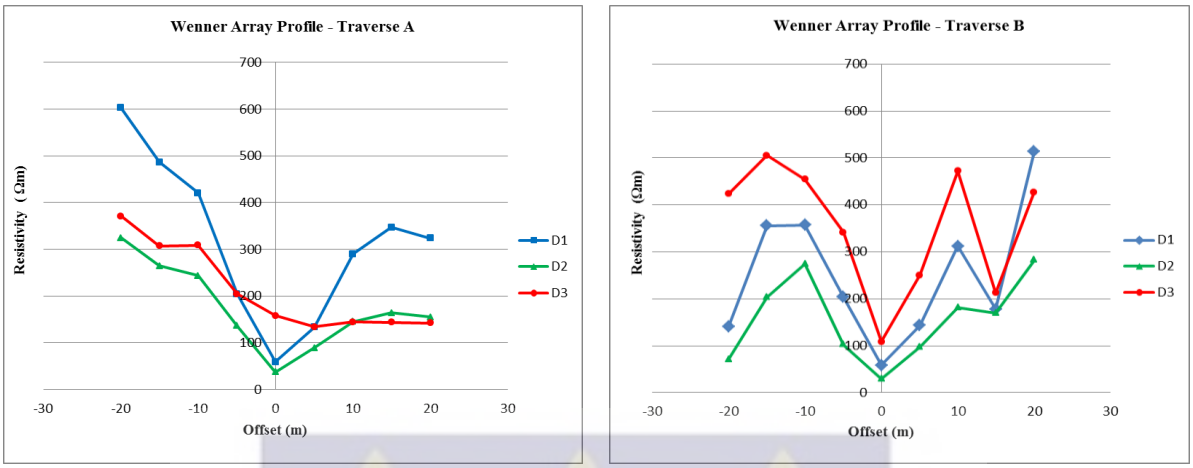


Figure 4.1.9a Wenner Array Profiles for REN-09 (SW-NE for Traverse A, SE-NW for Traverse B)

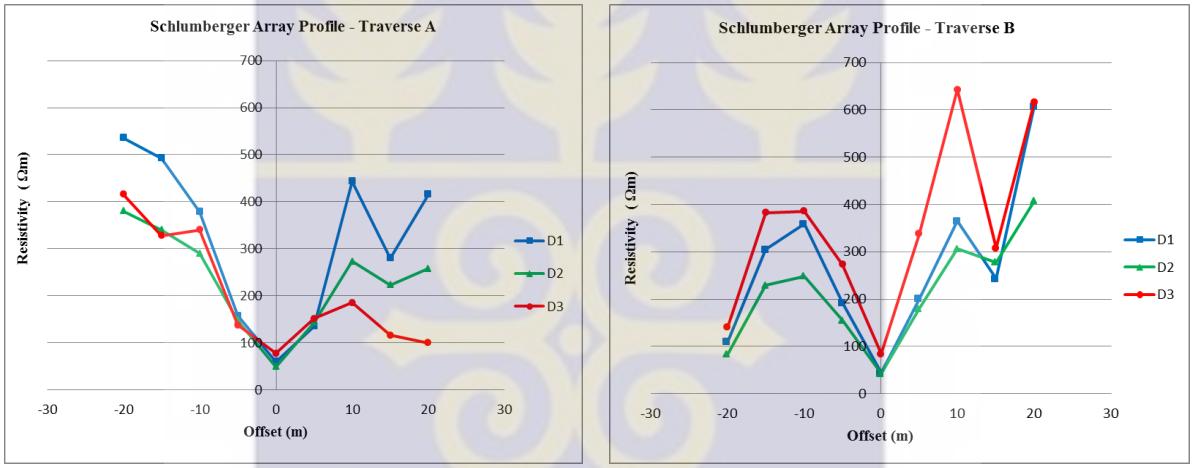


Figure 4.1.9b Schlumberger Array Profiles for REN-09 (SW-NE for Traverse A, SE-NW for Traverse B)

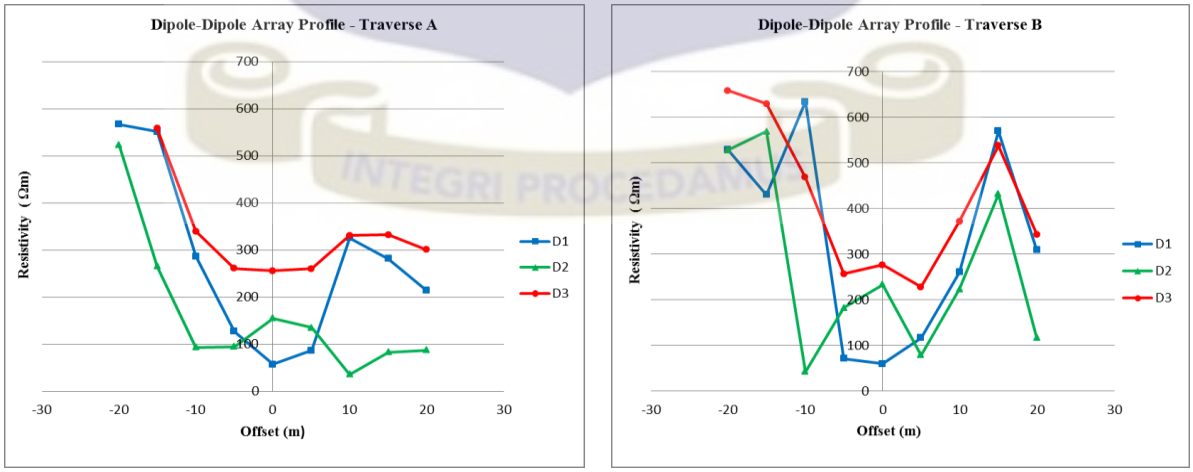


Figure 4.1.9c Dipole-Dipole Array Profiles for REN-09 (SW-NE for Traverse A, SE-NW for Traverse B)

Where $D_1$ = 1st Depth (Shallow), $D_2$ = 2nd Depth (intermediate) and $D_3$ = 3rd Depth (Deep)

The dipole-dipole array resistivity values ranged between 36.52 – 658.35 Ωm. Of the two, Traverse B had the higher values and the wider range. Figure 4.1.9c shows the profile plots.

Profile patterns were fairly similar. Traverse A profile patterns were fairly similar. $D_2$ and $D_3$ were fairly parallel. The resistivity was observed to be high at the ends of the traverse, more so to the SW. Resistivity along traverse was erratic with a general decrease to the NE. This was more prominent in the middle parts. The resistivity across depth was inconsistent. The drop in resistivity was only observed in $D_1$. Traverse B profile patterns were similar. They were however parallel for $D_2$ and $D_3$. Resistivity decreased toward the middle parts from observed high at the traverse ends. The resistivity across depth was inconsistent. There was an observed drop in resistivity over the borehole position.

Wenner and Schlumberger arrays had very similar profile patterns for Traverses A and B. Dipole-Dipole array profile patterns were also similar for Traverse A, but less so for Traverse B.

### 4.1.10 REN-10

The Wenner array resistivity values ranged between 208 - 991 Ωm. The resistivity values were similar for both traverses. Profile patterns were however different. Figure 4.1.10a shows the profile plots.

Traverse A profile patterns were similar, but not parallel. Resistivity decreased generally from the SW toward the NE. The resistivity variations were sharper for the first half of the traverse. This was consistent across depth. Resistivity also decreased with depth along the first half of the traverse to quite similar values in the NE. There was no pronounced drop in

resistivity over the borehole position. Traverse B profile patterns were similar and fairly parallel for $D_1$ and $D_2$. $D_1$ and $D_2$ showed a general increase in resistivity toward the NW. $D_3$ profile rather showed a decrease in resistivity. Across depth, the resistivity trend was inconsistent. Resistivity decreased from $D_1$ – $D_2$ and decreased from $D_2$ – $D_3$ to the SE. Resistivity decreased with depth to the NW. There was no resistivity drop over the borehole position.

The Schlumberger array resistivity values ranged between 129.1 – 1110 Ωm. The resistivity values for both traverses were similar. Profile patterns were different for both traverses. Figure 4.1.10b shows the profile plots.

Traverse A profile patterns were similar and fairly parallel. Resistivity generally decreased toward the NE. Resistivity varied sharply along the traverse and decreased with depth. There was an observed drop in resistivity over the borehole position. This was seen across depth. Traverse B profile pattern were similar and fairly parallel for $D_1$ and $D_2$. Resistivity variation along the traverse was erratic.

However, there was also a general decrease in resistivity toward the NW. Resistivity also decreased with depth. There was also an observed drop in resistivity across the borehole position.

The dipole-dipole array resistivity values ranged between 34.13 – 936.2 Ωm. The resistivity values were similar for both traverses. Profile patterns were however different. Figure 4.1.10c shows the profile plots.

Traverse A profile patterns were not similar and parallel, and erratic. Resistivity along the traverse was inconsistent, but a general increase to the NW could be deduced.

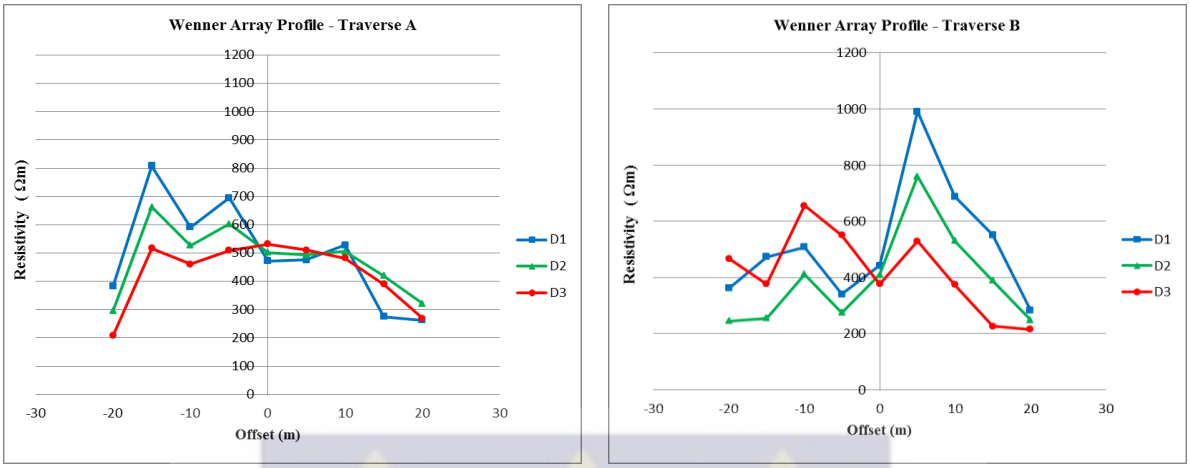


Figure 4.1.10a Wenner Array Profiles for REN-10 (SW-NE for Traverse A, SE-NW for Traverse B)

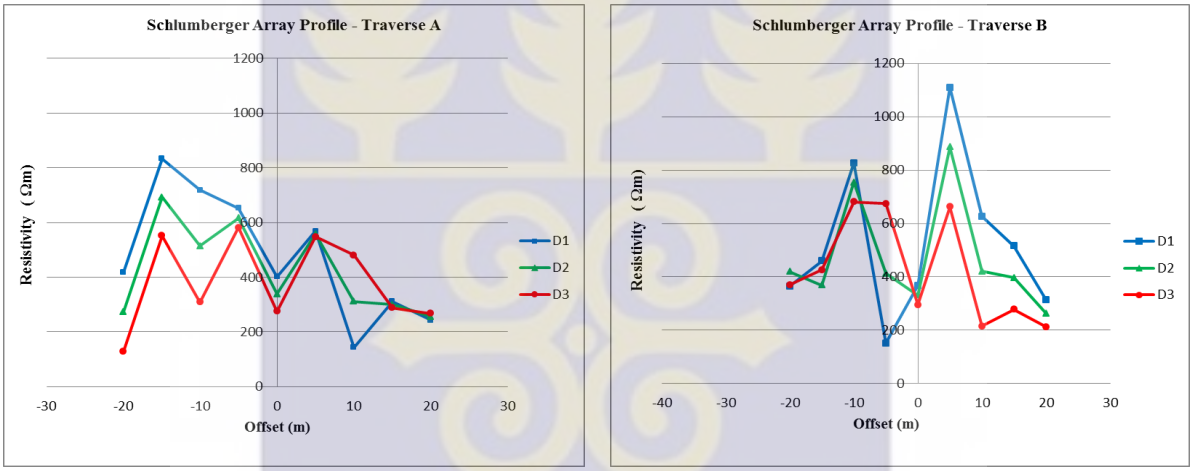


Figure 4.1.10b Schlumberger Array Profiles for REN-10 (SW-NE for Traverse A, SE-NW for Traverse B)

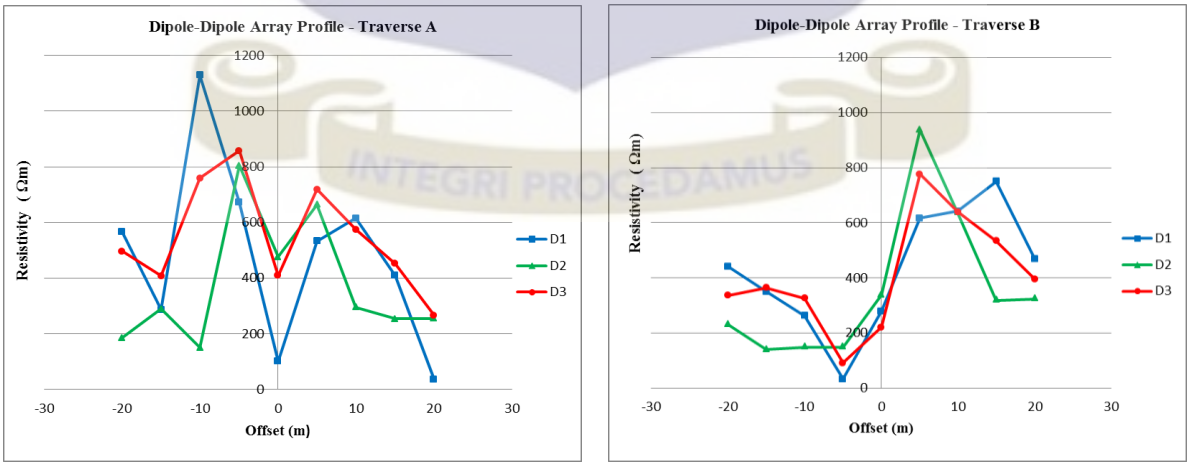


Figure 4.1.10c Dipole-Dipole Array Profiles for REN-10 (SW-NE for Traverse A, SE-NW for Traverse B)

Where $D_1$ = 1st Depth (Shallow), $D_2$ = 2nd Depth (intermediate) and $D_3$ = 3rd Depth (Deep)

The resistivity across depth was also inconsistent. There was a pronounced drop in resistivity over the borehole position. Traverse B profile patterns were similar, but not parallel. Resistivity increased sharply toward the NW, and increased across depth. The resistivity along traverse was less erratic. There was no observed drop in resistivity over the borehole position.

Wenner and Schlumberger array resistivity profile patterns were similar for both Traverses A and B. Dipole-Dipole array profile patterns had some semblance with the other two array profiles. However, the dipole-dipole array Traverse A profiles were distinctly different.

4.1.11 REN-11

The Wenner array resistivity values ranged between 66.34 – 719 Ωm. The profile plots are shown in figure 4.1.11a. Traverse A had both the higher resistivity values and the wider range. Profile patterns were different for both traverses.

Profile patterns for Traverse A were similar and parallel. Resistivity was largely uniform to the SW but increased sharply toward the NE. The resistivity also increased with depth. There was no drop in resistivity over the borehole position. This was observed across depth. Profile patterns for Traverse B were not similar and parallel. The resistivity along traverse and across depth was inconsistent. There was no drop in resistivity over the borehole position.

The Schlumberger array resistivity values ranged between 27.6 - 819 Ωm. The profile plots are shown in figure 4.1.11b. Traverse A had both the higher resistivity values and the wider range. Profile patterns were different for both traverses.

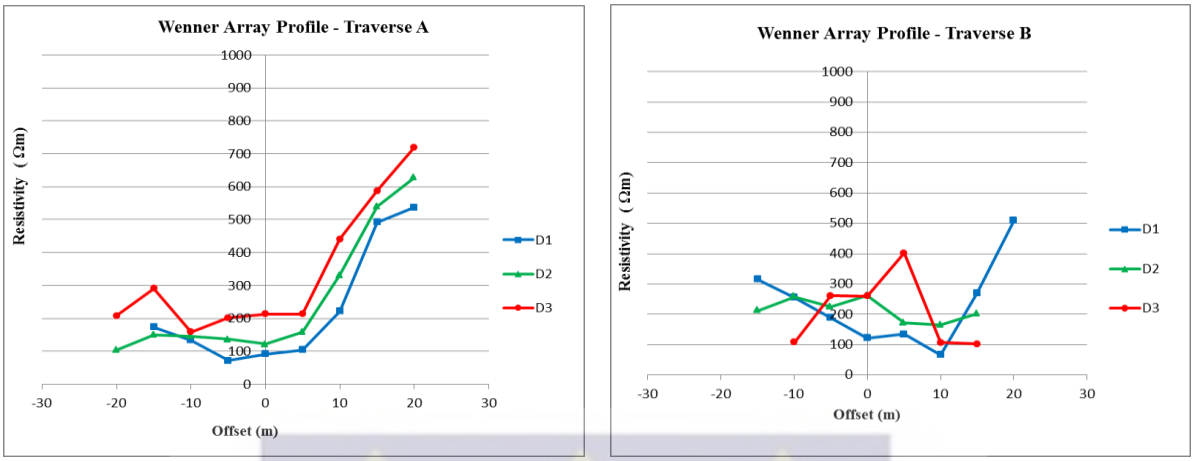


Figure 4.1.11a Wenner Array Profiles for REN-11 (SW-NE for Traverse A, SE-NW for Traverse B)

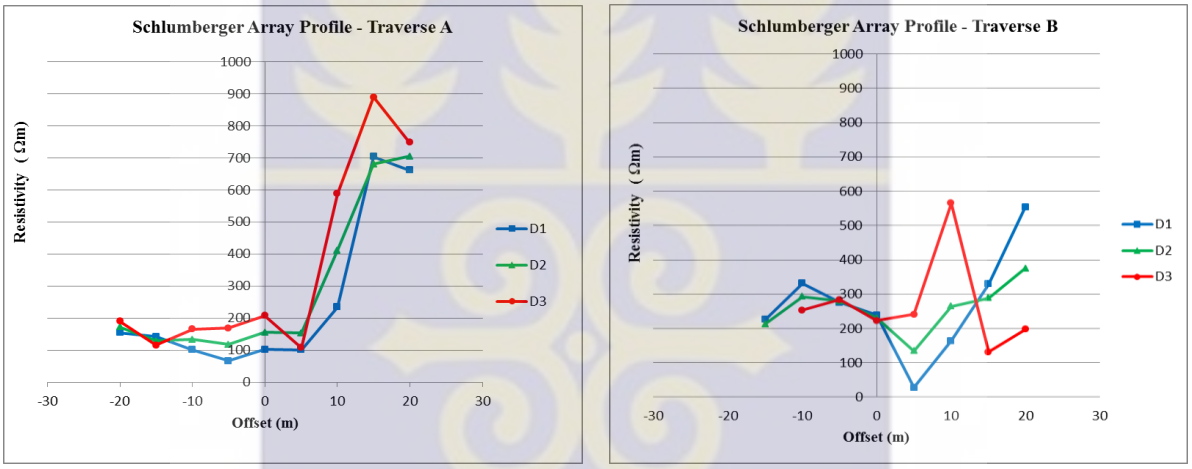


Figure 4.1.11b Schlumberger Array Profiles for REN-11(SW-NE for Traverse A, SE-NW for Traverse B)

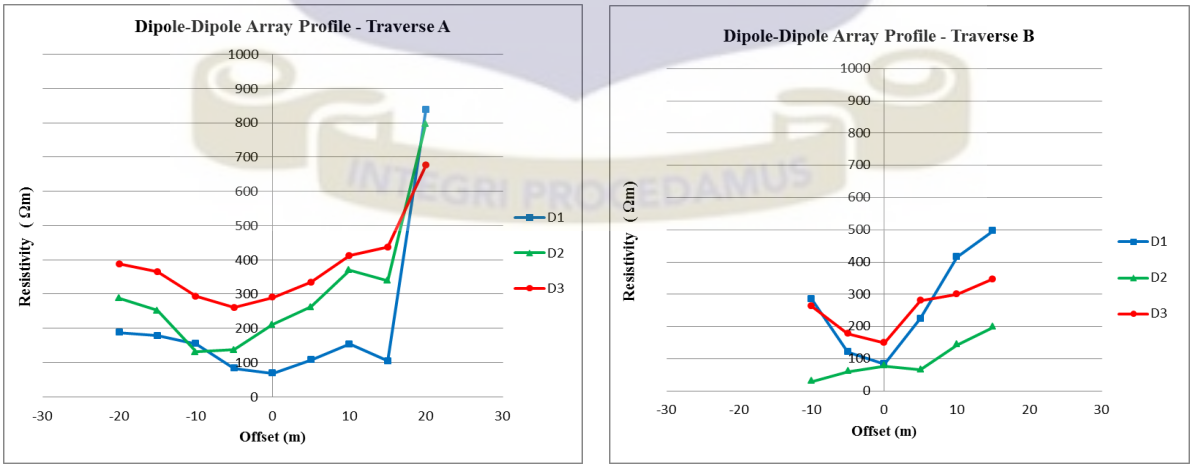


Figure 4.1.11c Dipole-Dipole Array Profiles for REN-11(SW-NE for Traverse A, SE-NW for Traverse B)

Where $D_1$ = 1st Depth (Shallow), $D_2$ = 2nd Depth (intermediate) and $D_3$ = 3rd Depth (Deep)

Profile patterns for Traverse A were similar and parallel. The resistivity along traverse was uniform to the SW and increased sharply toward the NE. Resistivity decreased with depth. There was no observed drop in resistivity over the borehole position. This was seen across depth. Profile patterns for Traverse B were also sharply-varying, not similar and nor parallel. The resistivity along traverse and across depth was inconsistent. There was no drop in resistivity over the borehole position.

The dipole-dipole array resistivity values ranged between 28.91 – 798.1 Ωm. The profile plots are shown in figure 4.1.11c. Traverse A had both the higher resistivity values and the wider range. Profile patterns were however different.

Profile patterns for Traverse A were similar and parallel. Resistivity increased to the NE, and across depth. There was no drop in resistivity over the borehole position. Profile patterns for Traverse B were not similar and nor parallel. The resistivity along traverse for $D_1$ and $D_3$ decreased from observed high to the SE and NW toward the middle parts. $D_2$ increased in resistivity toward the NW. Resistivity decreased from $D_1 – D_2$ and increased from $D_2 – D_3$. There was a pronounced drop in resistivity over the borehole position for $D_I$ and $D_3$. $D_2$ did not show this.

The profile patterns for Traverses A and B were very similar for Wenner and Schlumberger arrays. Dipole-Dipole array profile patterns for Traverse A were also similar to Wenner and Schlumberger array profile patterns. However, dipole-dipole array profiles showed gentle variation relative to sharper variation of the other two.

4.1.12 REN-12

The Wenner array resistivity values ranged between 157 – 1077 Ωm. The profile plots are shown in figure 4.1.12a. Resistivity values were fairly similar for both traverses. The profile pattern were however different.

Traverse A profile patterns were similar and parallel for $D_3$ and $D_2$. The resistivity along traverse decreased sharply from an initial high in the SW before increasing to the NE. Resistivity decreased towards the end of the traverse for $D_1$. $D_2$ and $D_3$ were fairly uniform. Resistivity decreased across depth for $D_1 – D_2$ before increasing for $D_2 – D_3$. There was no resistivity drop over the borehole position. Traverse B profile patterns showed some semblance between $D_1$ and $D_2$. These were also parallel. The resistivity along traverse was low at the SE and NW ends but peaked at the middle parts. Resistivity decreased with depth to the NW, but this was largely inconsistent along the profile. There was no drop in resistivity over the borehole position.

The Schlumberger array resistivity values ranged between 114.6 - 1183 Ωm. The profile plots are shown in figure 4.1.12b. Resistivity values were fairly similar. Profile patterns were different for both traverses.

The resistivity along traverse peaked at the middle parts and decreased gently toward the NE. Resistivity decreased across depth from $D_1 – D_2$ and increased slightly for $D_2 – D_3$. There was no observed drop in resistivity over the borehole position. Traverse B profile patterns were similar and parallel for $D_2$ and $D_3$. $D_1$ was erratic, with sharp variations along the traverse. Resistivity decreased slightly to the NW. Resistivity also decreased across depth for $D_1 – D_2$ and increased almost imperceptibly from $D_2 – D_3$.

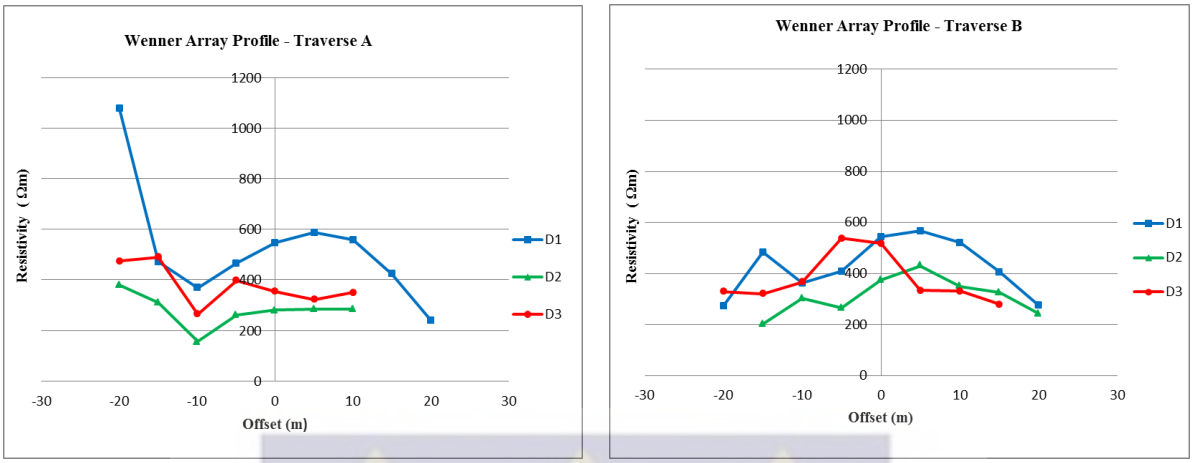


Figure 4.1.12a Wenner Array Profiles for REN-12 (SW-NE for Traverse A, SE-NW for Traverse B)

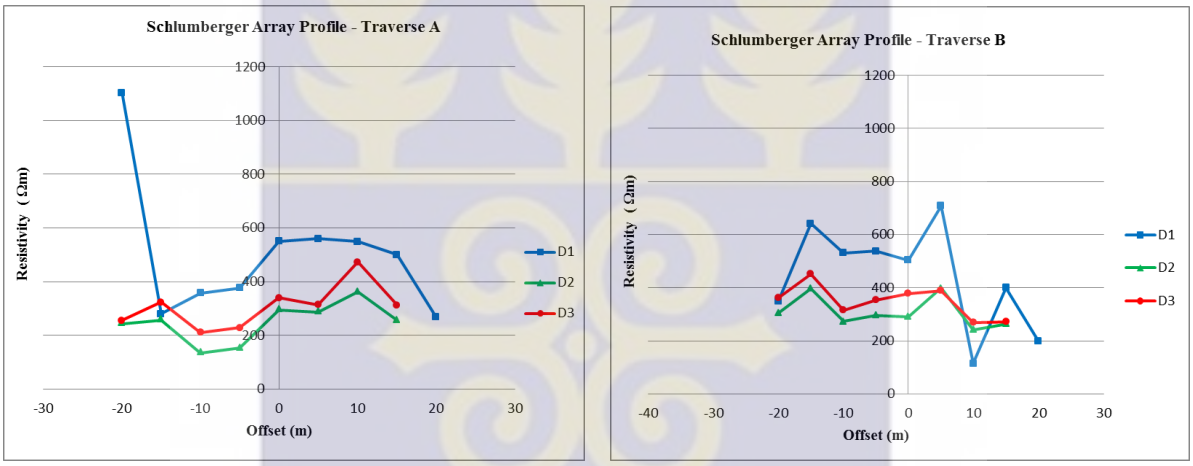


Figure 4.1.12b Schlumberger Array Profiles for REN-12 (SW-NE for Traverse A, SE-NW for Traverse B)

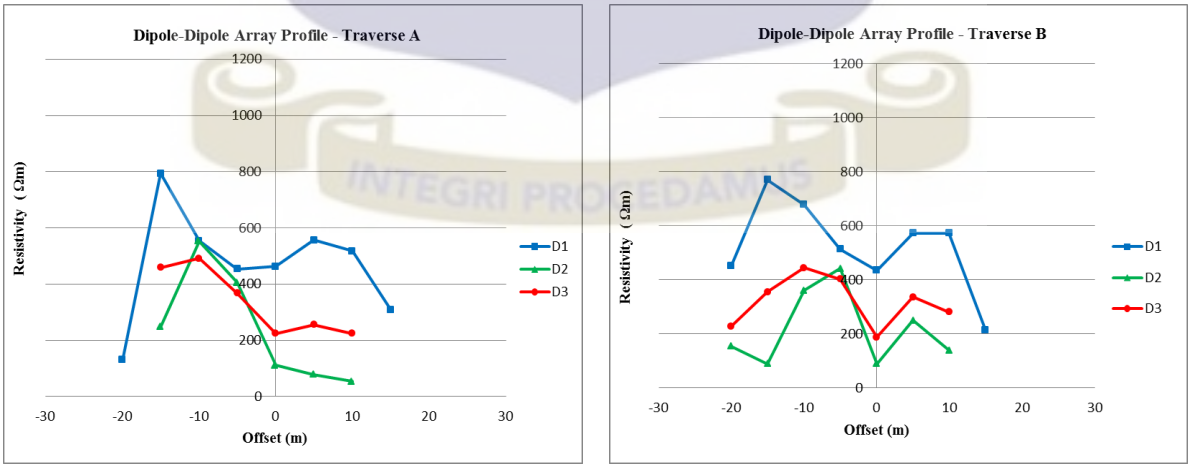


Figure 4.1.12c Dipole-Dipole Array Profiles for REN-12 (SW-NE for Traverse A, SE-NW for Traverse B)

Where $D_1$ = 1st Depth (Shallow), $D_2$ = 2nd Depth (intermediate) and $D_3$ = 3rd Depth (Deep)

There was no drop in resistivity over the borehole position.

The dipole-dipole array resistivity values ranged between 53.96 – 793.9 Ωm. The profile plots are shown in figure 4.1.12c. Traverse A had the wider range but Traverse B had the higher values. Profile patterns for both traverses were different.

Traverse A profile pattern were similar but not parallel for $D_2$ and $D_3$. $D_1$ profile pattern was different. There was however a general decrease in resistivity toward the NE. Resistivity decreased sharply across depth from $D_1 - D_2$ and increased for $D_2 - D_3$. This was not consistent. There was no drop in resistivity over the borehole position. Traverse B profile patterns were fairly similar and fairly parallel. The resistivity along traverse was erratic with sharp variations. Resistivity decreased sharply from $D_1 - D_2$ and increased slightly for $D_2 - D_3$. There was however a drop in resistivity over the borehole position.

Wenner and Schlumberger arrays profiles were similar for Traverse A, but differed for Traverse B. The Schlumberger array profile patterns were comparatively erratic. Dipole-Dipole array's $D_1$ profile for Traverse A shared some semblance with the other two arrays, Traverse B profile patterns were however different.

4.1.13 REN-13

The Wenner array resistivity values ranged between 16.76 – 846.9 Ωm. Figure 4.1.13a shows the profile plots. Traverse A had the higher values but Traverse B had the wider range. Profile patterns were different for both traverses.

Traverse A profile pattern were similar and fairly parallel for $D_1$ and $D_2$. $D_3$ was different. Resistivity along traverse was erratic and varied sharply. Resistivity however decreased with

depth. There was a drop in resistivity over the borehole position. $D_3$ did not show this. Traverse B profile patterns were similar but not parallel. Resistivity was observed to decrease sharply from the SE to almost uniform in the NW. There was no observed drop in resistivity over the borehole position.

The Schlumberger array resistivity values ranged between 40.84 – 938.6 Ωm. Figure 4.1.13b shows the profile plots. Similarly, Traverse A had the higher values and Traverse B, the wider range. Profile patterns were different for both Traverses.

Traverse A profile patterns were similar and fairly parallel. The resistivity along traverse was inconsistent and very erratic. A general high was observed in the SW and an increase toward the NE. Resistivity decreased with depth. There was a pronounced drop in resistivity over the borehole position. This was reflected across depth. Traverse B profile patterns were similar but not parallel. Resistivity decreased sharply from an initial high in the SE to almost uniform in the NW. Resistivity also decreased sharply across depth to almost uniform in the NW. There was no drop in resistivity over the borehole position.

The dipole-dipole array resistivity values ranged between 23.52 – 502.6 Ωm. Similarly, Traverse A had the higher values and Traverse B, the wider range. Figure 4.1.13c shows the profile plots.

Traverse A profile patterns were not similar and not parallel. The resistivity along traverse was erratic. However, $D_1$ and $D_3$ showed high resistivity in the SW and an increase toward the NE. Resistivity decreased with depth. There was no observed drop in resistivity over the borehole position. Traverse B profile patterns were fairly similar for $D_2$ and $D_3$. $D_1$ was different. $D_1$ showed a sharp increase toward the NW.

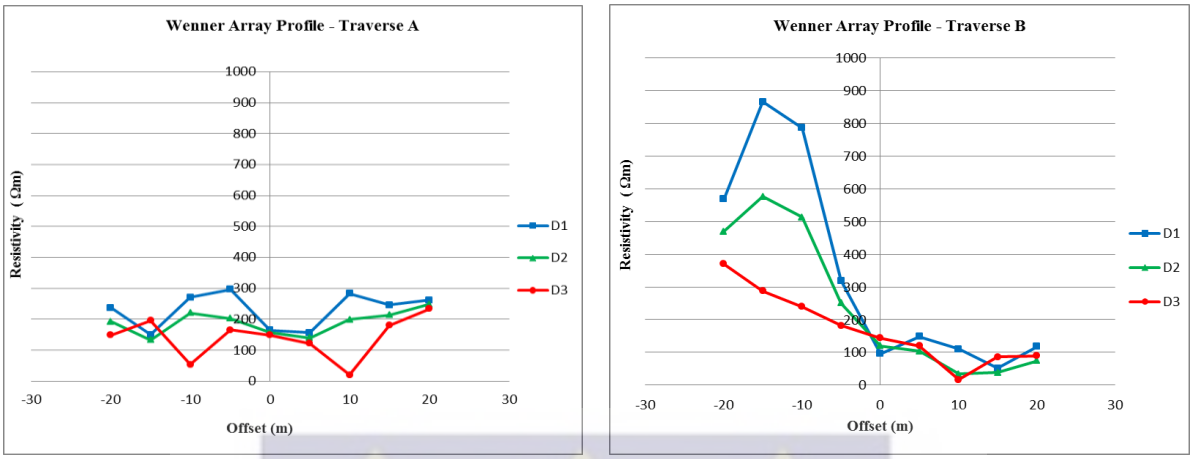


Figure 4.1.13a Wenner Array Profiles for REN-13 (SW-NE for Traverse A, SE-NW for Traverse B)

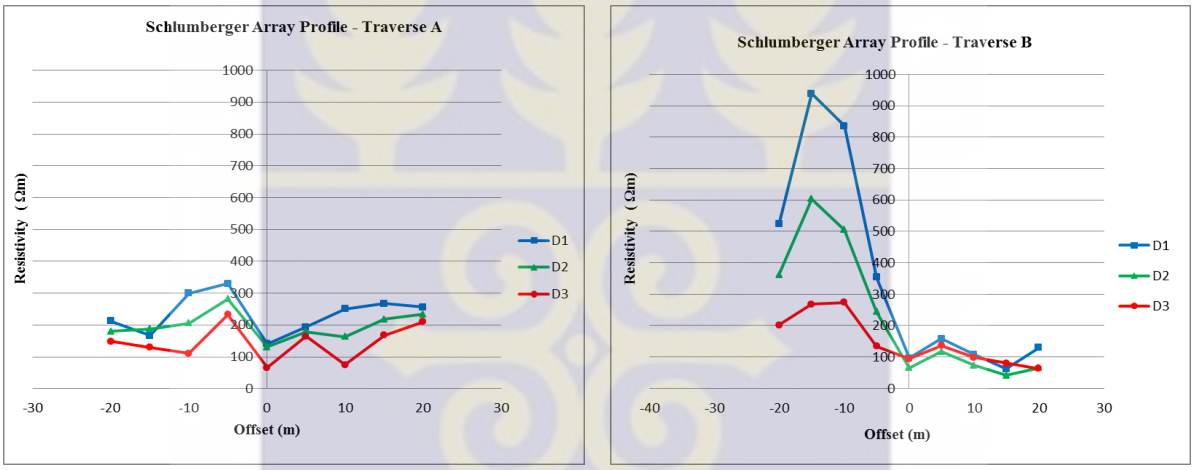


Figure 4.1.13b Schlumberger Array Profiles for REN-13 (SW-NE for Traverse A, SE-NW for Traverse B)

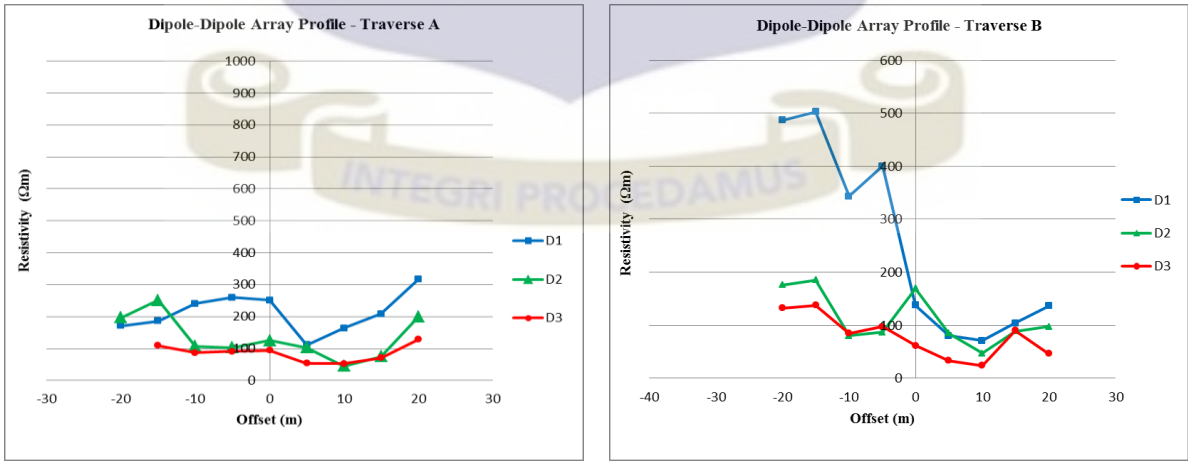


Figure 4.1.13c Dipole-Dipole Array Profiles for REN-13 (SW-NE for Traverse A, SE-NW for Traverse B)

Where $D_1$ = 1st Depth (Shallow), $D_2$ = 2nd Depth (intermediate) and $D_3$ = 3rd Depth (Deep)

$D_2$ and $D_3$ showed a much gentle decrease. Resistivity also decreased with depth. This was prominent to the SE. There was no drop in resistivity across the borehole position.

Wenner and Schlumberger array profile patterns for Traverse A had some semblance. Traverse B profile patterns were however much similar. Dipole-Dipole array profile patterns for Traverse A were different compared to the other arrays. Traverse B profiles were however also similar to the Wenner and Schlumberger array profiles.

4.1.14 REN-14

The Wenner array resistivity values ranged between 5.23 – 549.8 Ωm. Traverse A had both the higher values and the wider range. Profile patterns were different for both traverses. Figure 4.1.14a shows the profile plots.

Traverse A profile patterns were similar for $D_1$ and $D_2$ but not parallel. $D_3$ was different. The resistivity along the traverse decreased toward the middle parts from observed highs in the SW and NE. Resistivity decreased across depth from $D_1 – D_2$ and increased sharply from $D_2 – D_3$. There was a drop in resistivity over the borehole position. Traverse B profile patterns were similar but not parallel. Resistivity decreased sharply from an observed high in the SE toward the NW. Resistivity varied sharply along the traverse. Resistivity decreased across depth from $D_1 – D_2$ and increased sharply from $D_2 – D_3$. There was no drop in resistivity over the borehole position.

The Schlumberger array resistivity values ranged between 11.60 – 630 Ωm. Traverse A had both the higher values and the wider range. Profile patterns were different for both traverses. Figure 4.1.14b shows the profile plots.

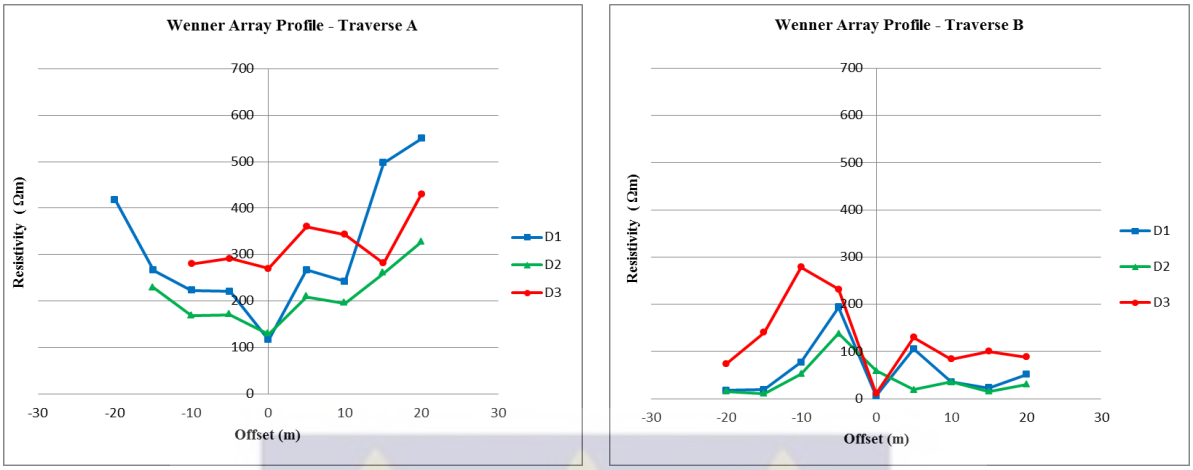


Figure 4.1.14a Wenner Array Profiles for REN-13 (SW-NE for Traverse A, SE-NW for Traverse B)

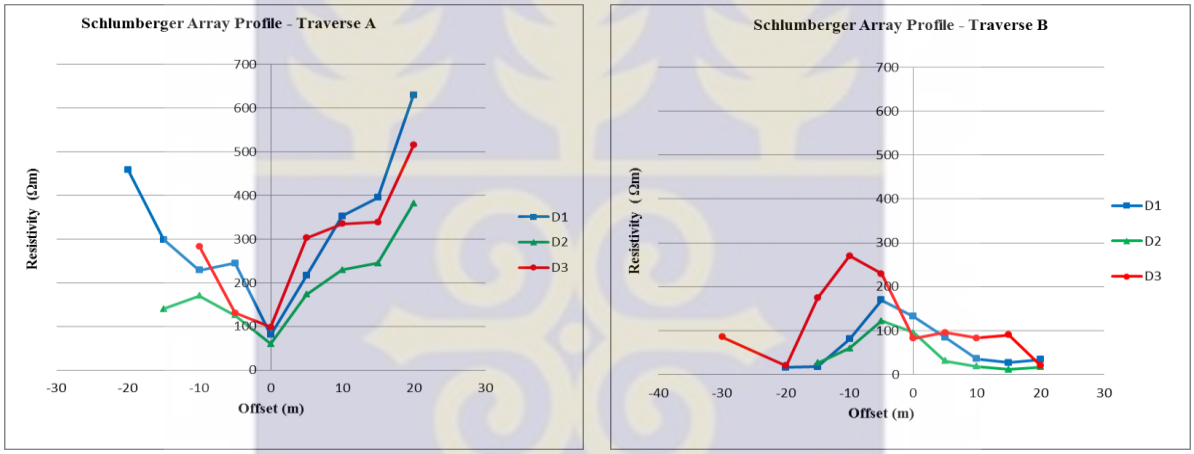


Figure 4.1.14b Schlumberger Array Profiles for REN-14 (SW-NE for Traverse A, SE-NW for Traverse B)

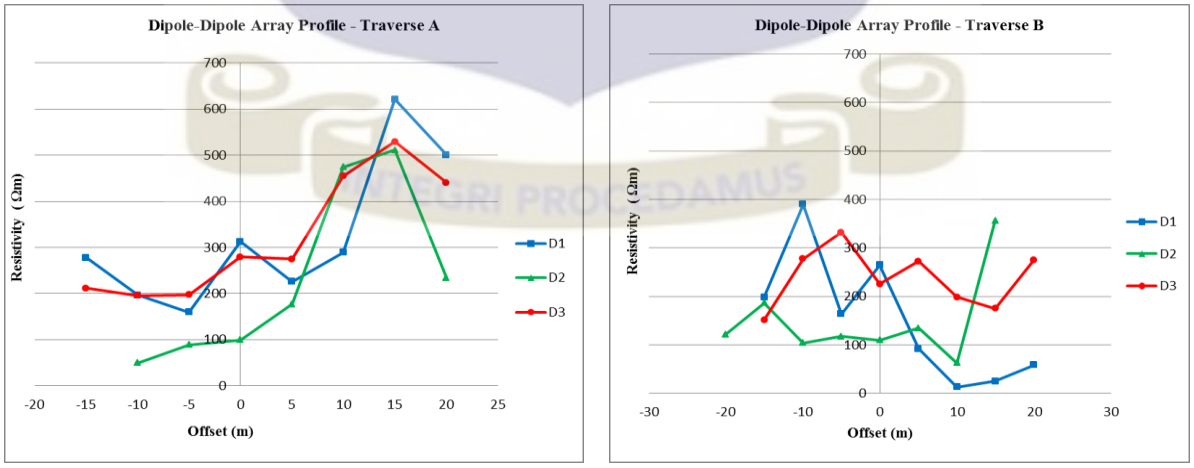


Figure 4.1.14c Dipole-Dipole Array Profiles for REN-14 (SW-NE for Traverse A, SE-NW for Traverse B)

Where $D_1$ = 1st Depth (Shallow), $D_2$ = 2nd Depth (intermediate) and $D_3$ = 3rd Depth (Deep)

Traverse A profile patterns were similar but not parallel. The resistivity along traverse decreased from observed highs in the SW and NE toward the middle parts. Resistivity varied sharply along the traverse. Resistivity decreased across depth from $D_1 - D_2$ and increased from $D_2 - D_3$. There was a pronounced drop in resistivity over the borehole position. Traverse B profile patterns were fairly similar but not parallel. Resistivity decreased generally toward the NW from an observed high in the SE. Resistivity decreased across depth from $D_1$ and $D_2$ and increased sharply for $D_2 - D_3$. There was no drop in resistivity over the borehole position.

The dipole-dipole array resistivity values ranged between 13.1 – 621.5 Ωm. Similarly, Traverse A had the higher values and the wider range. Profile patterns were different for both traverses. Figure 4.1.14c shows the profile plots.

Traverse A profile patterns were similar for $D_1$ and $D_3$, but not parallel. Resistivity generally decreased toward the SW. Resistivity varied sharply along the traverse. Resistivity also decreased for $D_1 - D_2$ and increased for $D_2 - D_3$.

There was no drop in resistivity over the borehole position. Traverse B profile patterns were not similar and parallel, but erratic. The resistivity trends both along traverse and across depth were ill-defined. There was no drop in resistivity over the borehole position.

Wenner and Schlumberger array profile patterns were similar for both Traverses A and B. Schlumberger array profile for Traverse A however showed sharper variation along the traverse. Dipole-Dipole array profile patterns for both traverses were different, compared to that from the other two arrays.

4.1.15 REN-15

Wenner array resistivity values ranged between 10.9 - 1315 Ωm. The profile plots are shown in figure 4.1.15a. Traverse A had the higher values and Traverse B, the wider range. Profile patterns were quite similar.

Traverse A profile patterns were similar but not parallel. The resistivity along traverse decreased sharply from observed high in SW and NE toward the middle parts. Resistivity also decreased across depth for $D_1 - D_2$ and increased $D_2 - D_3$. This was however not consistent along traverse. There was a pronounced drop in resistivity across the borehole position. Traverse B profile pattern were similar but not parallel. Resistivity also decreased along the traverse from observed high in the SE and NW toward the middle parts. Resistivity decreased across depth from $D_1 - D_2$ and increased from $D_2 - D_3$. This was also not consistent along the traverse. There was also pronounced drop in resistivity over the borehole position.

The Schlumberger array resistivity values ranged between 61.82 - 1447 Ωm. The profile plots are shown in figure 4.1.15b. Similarly, Traverse A had the higher resistivity values and Traverse B, the wider range. Profile patterns were similar for both traverses.

Traverse A profile patterns were similar but not parallel. Resistivity also decreased sharply along the traverse from observed highs in the SW and NE toward middle parts. Resistivity decreased across depth from $D_1 - D_2$ and increased sharply for $D_2 - D_3$. There was a pronounced drop over the borehole position. Traverse B profile patterns were similar $D_1 - D_2$ but not parallel. $D_3$ was different. However, resistivity decreased from the high in the SE and NW toward the middle of the traverse. $D_3$ showed a constant decrease toward the SE.

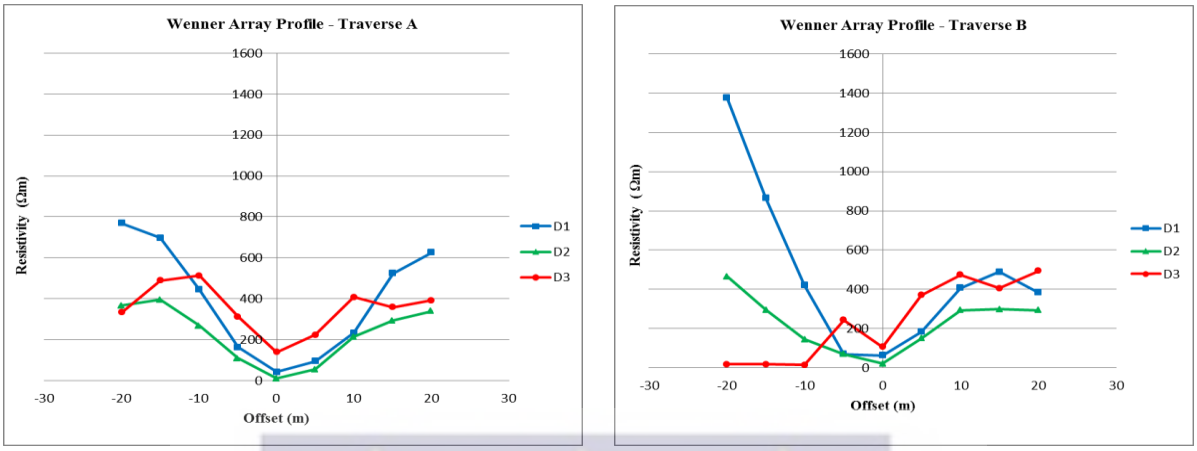


Figure 4.1.15a Wenner Array Profiles for REN-15 (SW-NE for Traverse A, SE-NW for Traverse B)

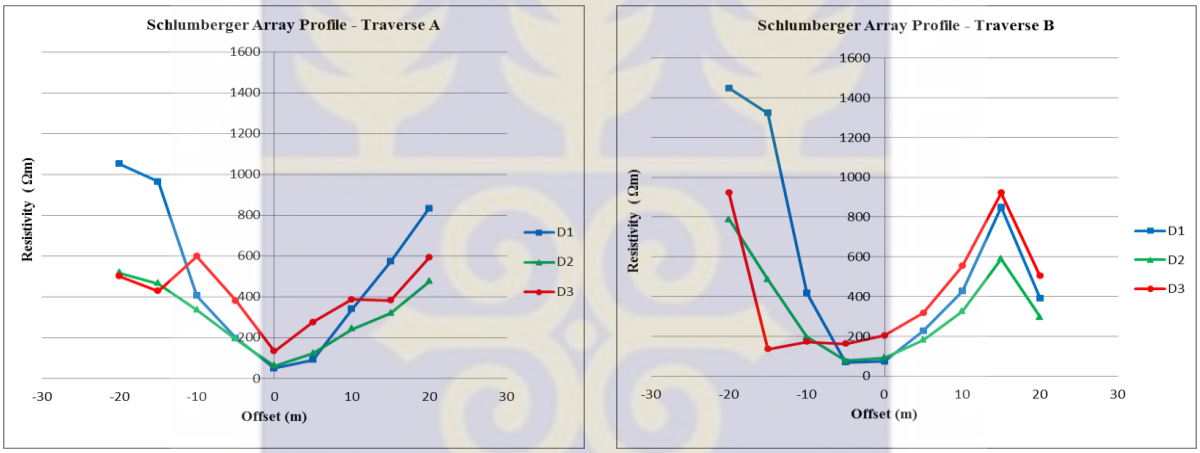


Figure 4.1.15b Schlumberger Array Profiles for REN-15 (SW-NE for Traverse A, SE-NW for Traverse B)


Figure 4.1.15c Dipole-Dipole Array Profiles for REN-15 (SW-NE for Traverse A, SE-NW for Traverse B)

Where $D_1$ = 1st Depth (Shallow), $D_2$ = 2nd Depth (intermediate) and $D_3$ = 3rd Depth (Deep)

Resistivity also decreased with depth for $D_1 - D_2$ and increased from $D_2 - D_3$. There was a drop in resistivity over the borehole position.

The dipole-dipole array resistivity values ranged between 52.98 - 1212 Ωm. The profile plots are shown in figure 4.1.15c. Traverse A had the higher values and Traverse B, the wider range. Profile patterns were similar for both traverses.

Traverse A profile patterns were also similar and not parallel. Resistivity was also observed to decrease from the SW and NE toward the middle of the traverse. Resistivity however increased across depth. There was a drop in resistivity over the borehole position. Traverse B profile patterns were similar and parallel for $D_2$ and $D_3$. $D_1$ was however less similar. Resistivity generally decreased along the traverse from NW and SE toward the middle. This was more prominent in $D_1$. The resistivity across depth was inconsistent. A drop in resistivity over the borehole position was seen in only $D_1$.

Wenner, Schlumberger and dipole-dipole array profile patterns were similar for Traverse A. Traverse B profile patterns were only similar for $D_1$. $D_2$ and $D_3$ were different for all the arrays.

The boreholes were sited across a range of terrane with corresponding differences in the subsurface resistivity structure. This would best explain the variety of profile patterns observed in the surveys across them. No two patterns were ever the same, giving credence to the argument that though similarities in material composition, texture and structure exists, no two subsurface volume in a stricter sense would be the same. The factors determining the resistivity a certain subsurface volume would exhibit could still vary across location in spite of these similarities.

The difference in profile patterns exhibited by the various arrays over the same subsurface was confirmative of their varying imaging ability. Different arrays could respond differently in resolving the same subsurface. Similarities in the profile patterns exhibited by the various arrays over the same subsurface as observed in REN-06 – Traverse A plots, could also be confirmative of an established subsurface resistivity structure, such as is seen over contact between materials of different composition. It also could be indicative of the simplicity of this structure (distinct boundary), enabling the arrays to reproduce it fairly. Homogeneity in the subsurface can also yield similar patterns for the different arrays irrespective of their varying imaging ability, as seen in $D_3$ profiles of REN-02 (figure 4.1.2).

Differences observed in profiles of the same array for the different traverses (A and B) as seen in most of the plots, were also suggestive of the existence of lateral inhomogeneity in three-dimension. The extent of difference between the patterns could be a measure of the subsurface inhomogeneity. Conversely, the extent of similarity in profile patterns of the same array for both traverses could also be a measure of the subsurface homogeneity.

Similarities between profiles across depth ($D_1$, $D_2$, $D_3$) for the same array along the same traverse as seen in plots such as REN-11 – Traverse A (figure 4.1.11), was an indication of an established regular vertical electrical structure existing in the subsurface along that traverse bearing. The parallel nature of these profiles was also suggestive of lateral continuity and uniformity in width, and magnitude of gradient change of resistivity in the subsurface. This could be indicative of such feature as gradational change in the subsurface materials.

The position of various profiles in the plots relative to each other (vertical juxtaposition) was indicative of gradient of resistivity change between the depths represented by these profiles.

Where successive profiles ($D_1$-$D_2$, $D_2$-$D_3$) were closely spaced as seen in plots such as REN 11-Traverse A, resistivity variation across the two levels was small. Where profiles were widely apart, as seen in plots such as REN 02-Traverse A (figure 4.1.2), resistivity variation was correspondingly large.

Differences in vertical structure between traverses deduced from profiles of the same array, as seen in plots such as seen in plots for REN-05, were an indication of a three-dimensional subsurface complexity with respect to resistivity distribution. This could be attributed to a highly heterogeneous subsurface in terms of material composition, irregular material distribution and factors such as differential compaction, enhanced by anthropogenic activities. Inconsistencies in the vertical structure such as were seen in the profiles of the different arrays were an indication of the varying ability of the arrays to fully appreciate these complexities and resolve them. The extent of the difference in this vertical structure could also be a measure of the difference in the imaging ability of the arrays.

### 4.2 Anisotropy

Magnitude of resistivity over the borehole positions differed with traverse direction. There was no preferential association of the higher resistivity values with any of the traverse directions. Anisotropy was observed across all boreholes and reflected in all array profiles. The anisotropy coefficient ($\Lambda$) was determined for all three depths, for the different arrays, adopting equation from Mota et al. (2008).

$$\Lambda=\sqrt{(\rho_{max}/\rho_{min})} \qquad (16)$$

The equation was originally derived to address anisotropy related to structural heterogeneity. This type of anisotropy is characterized by consistency in the higher resistivity values ($\rho_{max}$) being associated with a particular direction. This is typical of investigation of greater depth, such as in fractured bedrock. However, this consistency was absent; a suggestion that the observed anisotropy was not structural-related, but most likely compositional. This is also typical of investigation of shallow depth, such as in the overburden where lateral heterogeneity is dominant. The range of anisotropy coefficients for the various arrays across depth have been summarized in table 1.

Table 1.Table showing Anisotropy coefficients for $D_1$, $D_2$ and $D_3$ for Wenner, Schlumberger and dipole-dipole array

| Depth | Wenner array (Λ) | Schlumberger array (Λ) | Dipole-Dipole array (Λ) |
|---|---|---|---|
| $D_1$ | 2.21 – 0.82 | 1.24 – 0.21 | 1.65 – 0.66 |
| $D_2$ | 2.28 – 0.79 | 1.46 – 0.67 | 1.82 – 0.65 |
| $D_3$ | 1.78 – 0.77 | 1.65 – 0.66 | 1.18 – 0.58 |

### 4.3 Dumpsite Model Sections

Pseudo- and inverse modeled sections of the dumpsite are shown and discussed below. Pseudo-sections have been maintained for qualitative inference of the general subsurface resistivity trend. Some features in the pseudo-sections appear to have been retained in the true resistivity sections.

The inversion process converged after 3 iterations with RMS (root-mean-squared) misfits between 3.5% – 35.6%. The general resistivity trends for sections of both traverses (A and B)

were similar vertically, but showed much difference horizontally. This was reflective of the lateral inhomogeneous character of the site. For similar inter-current electrode spacing, Wenner array sections had relatively less depth coverage of 3.16 m to Schlumberger array's 3.79 m. The dipole-dipole array had depth coverage of 3.14 m.

### 4.3.1 Traverse A

Pseudo-and Inverse model sections of Wenner, Schlumberger and dipole-dipole arrays obtained along the traverse have been shown in Figure 4.3.1a, b and c respectively.

i. Wenner Array Section

Resistivity sections for Wenner array for Traverse A, corresponding to the 'along strike' direction of the local geology, are shown in Figure 4.3.1a. The sections were in the NE-SW direction. The RMS misfit was 3.5%.

The section shows two distinct features with large resistivity contrast, juxtaposed and clearly defined. The first is a low resistivity zone beginning at the middle of the traverse and extending towards the northeastern end. The zone narrows in width with depth. Resistivity increases constantly with depth along the zone and varies across it.

The second feature is a high resistivity zone which is prominent at about 1 m and increases in resistivity with depth. This zone extends laterally at depth, from the middle towards the southwestern part of the section. Resistivity varies along the length of the feature, and also increases with depth. The upper part (depth of about 2 m) of the northeastern end of the section shows high but fairly uniform resistivity. Pockets of lateral variations of resistivity occurs more to the southwestern end.

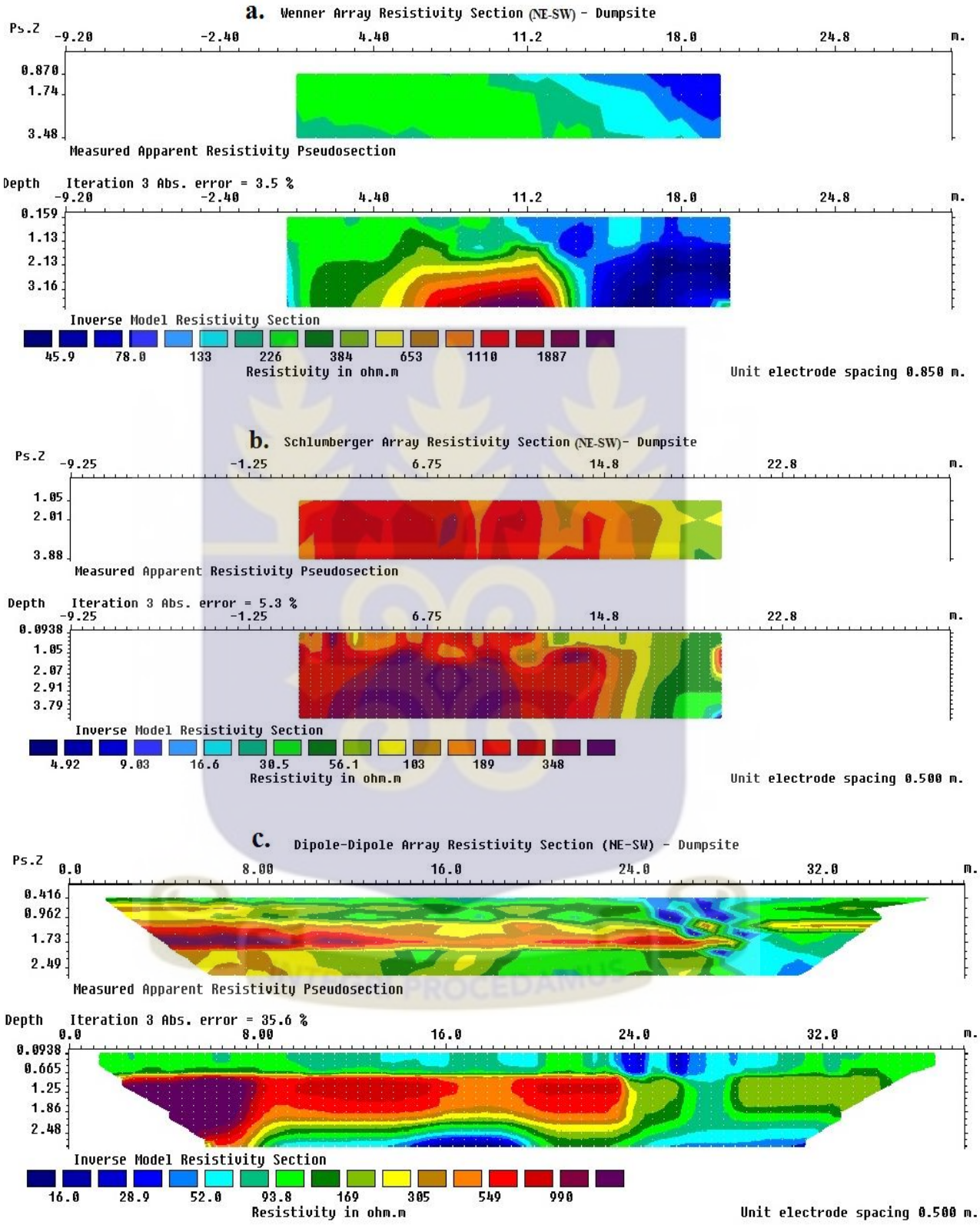


Figure 4.3.1a, b and c. Pseudo- and Inverse model sections for Traverse A

ii. Schlumberger Array Section

Resistivity sections for the Schlumberger array for Traverse A, corresponding to the 'along strike' direction of the local geology is shown in Figure 4.3.1b. The sections are in the NE-SW direction. The RMS misfit was 5.3%.

The section like the Wenner array's, shows two prominent features with large resistivity contrast, juxtaposed. The first feature has a higher resistivity, with well-defined geometry. It also occurs at about a depth of a metre at the middle of the section and extends towards the northeastern end of the section. Resistivity along the feature decreases gently from the middle towards the NE into a low resistivity zone. A thin high resistivity layer is also distinguishable. It is characterized by pockets of contrasting resistivity zones extending laterally towards the NE from the middle of the section. The layer had a thickness of about a metre from the surface and is clearly distinct in the NE half of the section, sitting atop the higher resistivity zone.

iii. Dipole-Dipole Array Section

The dipole-dipole array resistivity section for Traverse A is shown in Figure 4.3.1c. The RMS misfit was 35.6%.

The section shows three layers with distinct resistivity contrast. The first layer, thin, extends to a depth of about a metre from the surface and can be traced across the length of the section. Resistivity along the layer is not uniform. It is characterized by pockets of variations in resistivity as expected in near surface environment.

The second layer is of relatively high resistivity. The layer is intermediate in depth and extends to the SW for most part of the section. Resistivity along and across this layer varies. There are also three observed zones of exceptionally high resistivity along it. The second layer grades sharply into the third. The third layer has the lowest resistivity.

Laterally, the section was resolved into two zones, a high resistivity NE and a low resistivity SW. The low resistivity zone extended from the surface, narrowed mid-depth and widened laterally with increasing depth.

Both Wenner and Schlumberger array sections had good resolution, vertically and horizontally. The horizontal and vertical extents of the prominent features were well defined. Resistivity variation across and along the features were clearly distinguished, but more so in the Wenner array section. However, the Schlumberger array sections showed better resolution horizontally than the Wenner array. The lateral inhomogeneity from the near surface section was well represented and distinct as seen in the upper parts of the section (figure 4.3.1b). The Wenner array section did not show this (figure 4.3.1a).

The dipole-dipole array section (figure 4.3.1c) bore similarities with the other two array sections in imaging the two prominent resistivity zones. It also imaged the near surface lateral inhomogeneity better than the Wenner array section, but not as good as the Schlumberger array section. Its major strength was the resolution of the subsurface resistivity structure vertically into distinct layers with sharp boundaries, as well as still affording appreciable horizontal resolution.

### 4.3.2 Traverse B

Pseudo-and Inverse model sections of Wenner, Schlumberger and dipole-dipole arrays obtained along the orthogonal traverse have been shown in Figure 4.3.2a, b and c respectively.

i. Wenner Array Section

Resistivity sections for Wenner array for Traverse B, corresponding to the 'across strike' direction of the local geology, are shown in Figure 4.3.2a. The sections were in the NW-SE orientation. The RMS misfit was 14.2%.

The section also shows two distinct features juxtaposed laterally; a high resistivity zone to the NW, extending to more than half the section length and a low resistivity zone confined to the SE.

The higher resistivity feature occurs at a depth of about 1.2 m and extended some 2 m across depth. The feature had a distinct upper limit boundary but grades vertically into a lower resistivity layer at its lower limit. Resistivity increases across its width to the NW. The low resistivity zone occupying the southeastern end extends uniformly across depth.

Resistivity varies only across the width and is constant across depth. The horizontal extent of the zone grades gently into the high resistivity zone but with visible contrast. Horizontal variation of resistivity in the upper part of the section is almost non-existing, except for some few pockets

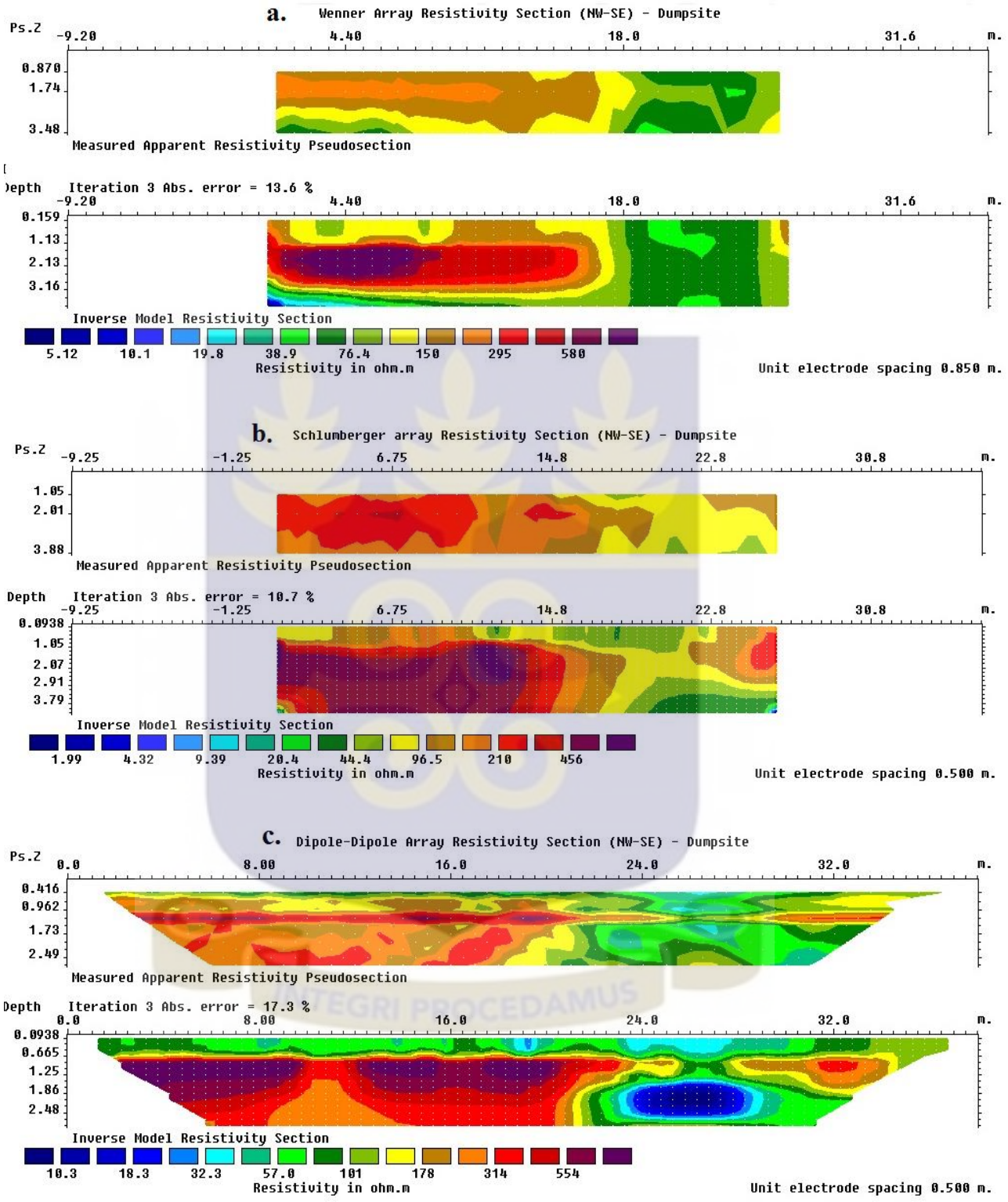


Figure 4.3.2a, b and c. Pseudo- and Inverse model sections for Traverse B

ii. Schlumberger Array Section

Resistivity sections for the Schlumberger array for Traverse B, corresponding to the 'across strike' direction of the local geology is shown in Figure 4.3.2b. The sections are in the NE-SW orientation. The RMS misfit was 10.7%.

The section shows two distinct features similar to the Wenner array; the high resistivity southeastern part and the low resistivity northwestern part. Unlike the Wenner array section, the resistivity contrast is large and the boundary sharper.

The high resistivity zone, beginning at a depth of about a metre also extends for about half the traverse length from the middle towards the SE and contacts the low resistivity zone rather sharply. It is also continuous vertically. Resistivity did not vary across and along the width of the feature. The low resistivity feature occupies much of the northwestern end of the section. It extends from the surface, narrows mid-depth and increases horizontally in size at depth. Resistivity varies along and across the width of the zone.

A thin, distinct layer characterized by small pockets of contrasting resistivity zones, mostly low, extends laterally across the section. The layer has a thickness of about a metre from the surface and is clearly distinct in the NW half as it contacts the higher resistivity zone sharply.

iii. Dipole-Dipole array Section

The Dipole-Dipole array resistivity section for Traverse B is shown in Figure 4.3.2c. The RMS misfit was 17.3%.

The section showed the subsurface as two main layers of contrasting resistivity vertically, and also two zones of contrasting resistivity horizontally. A thin layer of intermediate

resistivity which extends from the surface to a depth of 1 m can be observed across the section. The layer, as characteristic of the near surface environment has pockets of variations in resistivity. The layer is more distinct in the northwestern part of the section, where there is sharp contrast with the underlying layer.

The second layer is of considerably high resistivity, especially around the contact with the layer above. The layer extends horizontally about half the section towards the SE. The layer is continuous across depth in the NW, although with an accompanying gentle decrease in resistivity. Horizontally, the layer is seen to have three separate zones of high resistivity which evens out at depth.

The low resistivity zone occurs to the SE. This contacts areas of considerably high resistivity to the NW and SE. The zone extends from the surface and becomes more prominent at depth, in width and resistivity contrast. The vertical resistivity structure is not well defined in the SE, as seen in the NW, as a result of the similar resistivity. The section shows good resolution vertically and horizontally.

Resistivity sections of both the Wenner and Schlumberger arrays from Traverse B also had good resolution, with the latter being slightly better. Both arrays had imaged the prominent features with well-defined geometry. The Schlumberger array was once more better at resolving lateral variations in resistivity, especially in the near surface section. Variations in the thin distinct layer were examples. The Wenner array was better at imaging the resistivity variation across depth. The vertical resolution of resistivity across the high resistivity zone as imaged in the Wenner array section (figure 4.3.1a) is an example.

The dipole-dipole array section had the major features and trends in agreement with the other two arrays. However, the dipole-dipole array sections differed in the lateral extents of the features imaged. There appeared to be a sort of horizontal exaggeration of the features and a corresponding displacement of the boundary position, relative to the other two arrays. Hence, the array sections are more indicative of presence of the subsurface features than definitive in their extent, and consequently their location.

The general disposition of features imaged by both the Wenner and Schlumberger arrays in both Traverses A and B were similar, as shown by the sections. The low resistivity zones in both the Wenner and Schlumberger array sections from both Traverses A and B coincided with the part of the traverse lines running across the active portions of the dumpsite. The sharp resistivity contrast was a likely indication of leachate saturation and possible continual seepage. The high resistivity zones also coincided with the passive part of the site. The resistivity contrast resulting from the leachate is suspected to have further been increased by effects of heavy machinery being used in remedying exercises. This would have most likely increased near surface compaction considerably. As a result, a thin fluid-saturated layer had been created above this zone, which could be due to the inability of fluid to drain downwards. This layer and the sharp resistivity contrast have been well highlighted in the sections.

4.3.3 Buried Salt Unit

The 0.5 m-thick salt unit was emplaced between the depths 0.7-1.2 m. Results from vertical electrical sounding to determine array dimensions are shown in figure 4.3.3. After inversion, RMS misfits for the sections were 5.5%, 6.2% and 39.4% for Wenner, Schlumberger and

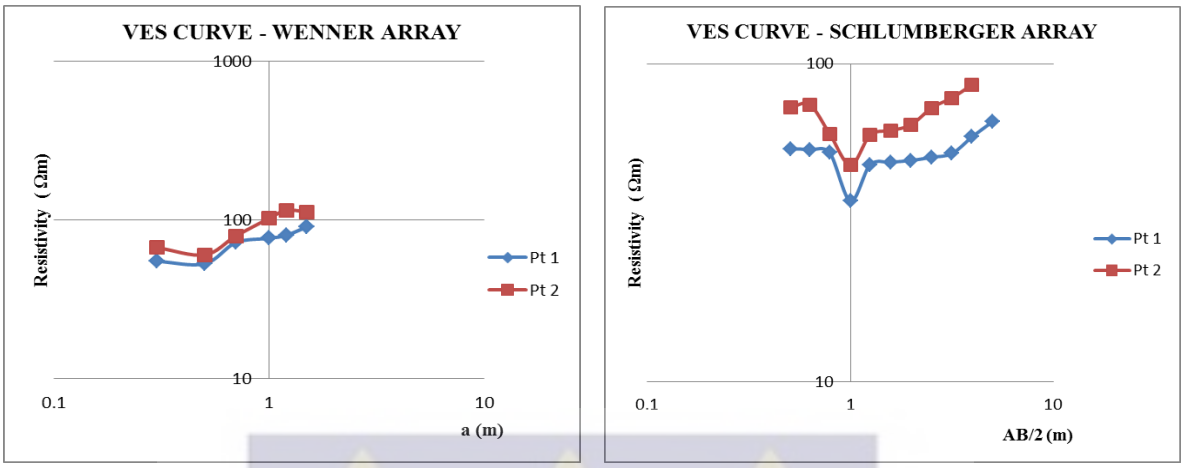


Figure 4.3.3. VES plots for to determine array dimensions corresponding to vertical position of buried salt

dipole-dipole arrays respectfully. Depth coverage of the sections was 1.52 m for the Wenner array and 2 m for the Schlumberger array and 1.53 m for dipole-dipole array. Pseudo-and Inverse model sections of Wenner, Schlumberger and dipole-dipole arrays obtained across the buried salt layer are shown in figure 4.3.4a, b and c respectively.

i. Wenner array Section

Resistivity sections for the Wenner array data set are shown in figure 4.3.4a.

The true section shows prominently the upper parts of the high resistivity feature imaged in figure 4.3.1a (appeared as two separate humps). Similarly, there are pockets of lateral variations of resistivity, mostly low, confined to the near surface parts of the section. These are now pronounced, as a result of the improved resolution and lesser depth coverage.

The part of the section coinciding horizontally with the position of the buried salt has a low resistivity pocket extending from the surface to a depth of about 1.2 m. This depth coincides with the lower limit of the vertical extent of the salt layer. The main low resistivity portion of the feature extends some 1.2 m in width but grades into relatively high resistivity towards the

NE. The extension of this feature beyond the upper limit of the salt layer could be explained by the existence of similar resistivity in the near surface environment creating insufficient contrast, hence the inability of the array to resolve it. Comparing that particular zone to that in figure 4.3.1a, this could likely be the case. The uniformity of the upward continuity of imaged near surface features also suggests this could be a processing artefact.

However difficult it would be to conclude this is the salt unit being imaged, it probably is, with the area above its upper limit coinciding with a low resistivity pocket. The pseudo-section clearly shows an anomalous feature coinciding with the vertical and horizontal position of the buried salt.

ii. Schlumberger array Section

Resistivity sections for the Schlumberger array data set are shown in figure 4.3.4b.

The true section also shows prominently pockets of lateral variations in resistivity. Most of these are low and similar in resistivity with no sharp boundaries horizontally. Resistivity is observed to increase with depth generally, and this is more evident in the southwestern part, as expected. The main feature of interest is a relatively low resistivity zone, more pronounced for its size than its contrast. It is of particular interest as it straddles the location of the buried salt vertically. Horizontally, resistivity across the feature is not uniform.

The horizontal extent of the more prominent part of the feature was about 2 m, same as the length of the salt unit. This is most likely the imaged salt unit. The vertical and horizontal dimensions which appear to have exceeded the limits of the unit could also be attributed to an environment of similar resistivity, and the consequent low contrast.

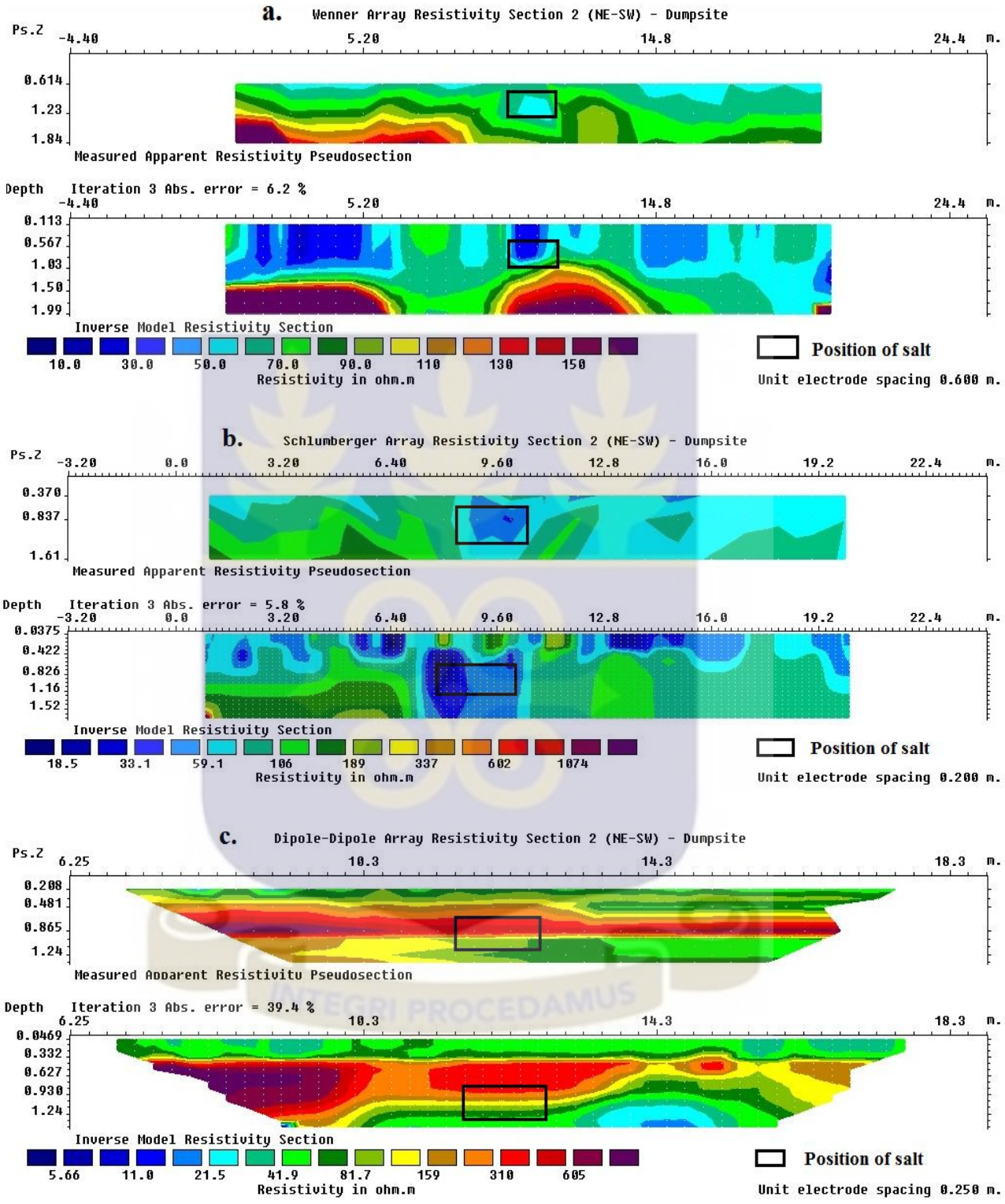


Figure 4.3.4a, b, c Pseudo- and Inverse model sections targeting the buried salt unit

The pseudo-section however shows an anomaly which is most likely the salt unit. The true section shows the feature position displaced horizontally to the SE.

iii. Dipole-Dipole array Section

The dipole-dipole array resistivity sections are shown in figure 4.3.4c. The RMS misfit was 39.4%.

The true section shows a thin intermediate resistivity first layer, a high resistivity second layer and a third intermediate-low resistivity layer. Resistivity is somewhat uniform along the layers horizontally. The section also shows a general decrease in resistivity with depth. Inhomogeneity seen as the pockets of variation in resistivity which characterized the near surface was conspicuously missing from the section, except for a few. These had been imaged in the initial section (figure 4.3.1c). The section also did not show any change in resistivity, be it sharp or subtle, which would be indicative of the buried salt unit. The vertical and horizontal position corresponding to the buried unit showed no such perturbation in resistivity. The position coincides with a part of the high resistivity second layer which is observed to be uniform before, at and after the location. The pseudo-section also did not show the salt unit.

The performance of each array, the similarities and differences in profiles and images as observed can be attributed collectively to the individual sensitivity, configuration and geometric factor, and profiling and or sampling technique.

Wenner and Schlumberger arrays are nested configurations. That is, the spatial arrangements of electrodes in these configurations are structured such that the potentials are sandwiched between the two current electrodes in a basic array unit. As a result, the propagation of

current and current path through the subsurface is expected to be similar for these two. This could be a contributing factor to the general similar nature of profiles and images of the two array types. The difference between these can also then be attributed to the geometric factor, K, which is the quantitative expression of the characteristic arrangement of current and potential electrodes in each basic unit. This would be responsible for the range of unique magnitudes of resistivity measured by both arrays, and all other arrays given the same subsurface volume. Over the same location using similar profiling technique, it would then be a logical conclusion that the observed difference in resistivity as reported by the various arrays would most likely be attributed to the only variable, the unique spatial positions and positioning of the electrodes. This holds great implication for the subsurface volume being sampled as per the distribution of equipotential generated, determined by the current electrodes location.

The measured parameter in the resistivity method is the potential difference across a certain subsurface volume, as a result of 'injected' current. The computed resistivity allotted to a particular location is therefore a weighted average of the current effects produced over the entire volume of material, with obvious contribution from nearby areas adjacent to that particular position. This weighted average factor is determined by the sampling volume, and the sampling volume is in turn determined by the potential electrode spacing.

In a laterally inhomogeneous setting, Schlumberger array often shows comparatively sharper variation in reported resistivity values as a result of the smaller sampling volume (inter-potential spacing). The values would be the nearest possible accurate representation of the 'true' resistivity of the sampling points because the small sampling volume would translate into minimal adjacent contribution and consequent 'adulteration' of the true resistivity. In

surveys (profiling and sounding), this volume is maintained along and across depth. The Wenner array has a larger sampling volume which must increase with increases in current electrode separation when probing deeper, in order to satisfy the array requirements. Such large sampling volumes would translate into increased 'neighbouring' effects (contribution from adjacent areas) on the reported resistivity value. With respect to sampling volume, analogies for Schlumberger and Wenner arrays would be discrete and bulk sampling respectively.

The profiling technique contributes to the observed difference and similarities in array resistivity trends. When an inter-sampling spacing is smaller than the inter-potential electrode spacing, a sampling process similar to a 'Moving Average' technique is established. For a given inter-current electrode distance corresponding to a similar effective depth of investigation, Wenner array would use this. The Schlumberger array configuration will not allow it. The 'Moving average' situation would occur as portions of a given subsurface stretch being sampled would overlap as the array unit progresses across it, due to the small constant separation. The values then reported at locations across the volume would be an average of subsequent overlapping volumes. This technique, in an inhomogeneous environment, has the potential to average out the sharp variations which would have otherwise been observed. The technique can level out distortions on profile patterns to both positive and negative ends.

The technique becomes positive when the feature of interest is of sufficient contrast but located in an inhomogeneous environment were resistivity vary sharply (noisy environment). The averaging technique could act as a sort of on-field suppression method, leveling out the noise (erraticism in the profiles) and making the anomalous trend more noticeable. The

technique could be negative in an environment of similar resistivity (low contrast between target and host) where the shape of the anomaly is of prime importance identifying it. The overlapping averaging process has the tendency to average out and reduce the already low contrast.

How well the geometry of an anomaly is imaged is a function of the inter-potential electrode spacing, inter-sampling distance and sampling density across the feature of interest. This is in situations where the features are of fixed known geometry. In any of the converse situation such as when information about the geometry is lacking, but a fixed geometry is anticipated, or the feature has an undefined geometry with time-varying migrating fronts (spillage, seepage and plume), the 'Moving Average' technique would be less desirable. Such features will show the magnitude of the resistivity contrast gradually reducing away from the source or centre of concentration. The technique and the bulk sampling process will most likely level out the decreasing resistivity contrast. Such migrating fronts and their precise location in space and time are usually crucial in surveys being carried out for evaluation and monitoring purposes. Arrays which would likely utilize these processes such as the Wenner would be best used cautiously in purely 'exploratory' surveys and surveys where high precision location of a feature in space is important. However, in mapping out vertical variation with little interest in horizontal variation, (such as mapping out vertical continuity of strata) this would be suitable. It is to be expected also that the resolving ability of the Wenner array would be less reliable at greater depth due to the increased sampling volume (inter-potential distance). The value would have greater percentage of 'neighbouring' effect.

The width of the inter-potential electrode spacing of the Schlumberger array allows it a relatively smaller sampling volume. A Schlumberger array profile can therefore be likened

crudely to a collection of 'discrete' values of subsurface resistivity fairly representative of the sampling positions along a given depth of investigation. This is important when horizontal variation of resistivity is of interest, such as when imaging the lateral continuity or discontinuity of lithology, structure or materials with unique similarities or contrasts. This will be more effective in surveys with small inter-sampling distance. In cases where the inter-sampling spacing is large, there is the tendency to miss out on a wealth of information between two subsequent sampling points, in the 'discrete' sampling process. This by-passed subsurface volume contributes minimally, if any at all, to the reported resistivity of the next or nearest sampling point. The Wenner array's larger sampling volume is more superior in reducing the loss of information in this phenomenon. Its 'Moving Average' sampling technique would accommodate this by-passed volume and consequently factor in its contribution to the final reported resistivity value. It is more superior in this sense.

The smaller width sampling could sometimes be inappropriate in a highly inhomogeneous environment with sharp resistivity variations. The collection of sharp contrasts along a profile possesses the ability of disrupting a characteristic pattern which would highlight the anomaly. The anomaly would have been imaged nevertheless, but the surrounding inhomogeneity and the resulting erratic nature of the profile can easily obscure it.

However, this small width technique presents the better option in defining the geometry and lateral extent of the anomaly when compared to the other two arrays, given equal sampling spacing. This technique would also be advantageous in imaging anomaly with minimal resistivity contrast laterally and would produce the best anomaly profile in a fairly homogeneous environment.

The dipole-dipole array setup has its potential electrodes outside and beside the current electrodes. This structure, along with the possible implication for current propagation could be the single largest contributing factor to the pronounced difference between the profiles and images of this array compared to the profiles and images of the other two arrays with the nested structure. As observed in the profiles, similarity is at its peak when there is a large contrast in the resistivity structure of the subsurface being imaged. Considering the produced profiles and images, there is the existence of a seeming likeness of the dipole-dipole array profiles and images with that of the other two arrays but these are most often than not characterized by an overwhelming exaggeration or under-statement of the observed general resistivity pattern with respect to the other two arrays. The result is a usual distortion of the finer aspects in the dipole-dipole array's reproduction of the general subsurface resistivity trends.

The dipole-dipole array has been touted to be the most sensitive of the three. Plots of the sensitivity function by Loke (2012) for the dipole-dipole array showed areas of highest sensitivity to be located between each electrode pair. This is twice as that of the nested arrays, whose highest sensitivity is located in the middle of the configuration. This, in addition to such small inter-potential spacing as used in the dumpsite surveys (1 m and 0.5 m), dipole-dipole array could reach hyper-sensitive proportions compared to the other two arrays. These observed ‘distortions’ most likely could be the better appreciation of the finer differences and resistivity ‘artefacts’ which had otherwise been ignored (due to lesser sensitivities), missed or leveled out (due to the sampling techniques) by the nested arrays, as a result of their inability to detect and resolve them. This could probably explain such observations as Seaton and Burbey (2002) that dipole-dipole array is very sensitive to even

very small structures. The cumulative effects of these finer differences on the final reported values could be that which is expressed in the resulting profiles and images produced from them. In a smaller more inhomogeneous area of investigation, such as the 'very' near subsurface, it is expected that this phenomenon be amplified. As such, dipole-dipole array profiles and images are expected to have an observed larger distortion of the general subsurface resistivity trend, relative to the other two arrays. This was a common observed pattern of dipole-dipole array data collected in the study. Dipole-Dipole profiles and images were pre-dominantly non-conforming with respect to trends observed in the images and profiles of the other two arrays.

Consequently, over a wider area, with wider sampling volume (inter-potential spacing), observed similarity with the general resistivity trends are expected to increase and imaged features will have a higher percentage of correlation.

Differences in resistivity values as reported by the various arrays are also likely to be influenced by time-varying natural stray currents in the sub-environment. The magnitude of the current and direction of flow are not constant, and cannot be predicted. As such, resistivity observed over the same subsurface will change even for the same array over time. Resulting patterns are likely to be different. Using different arrays at different times would only mean different results. However, these currents are often small in magnitude and their effects, though present are usually negligible. Some resistivity meters are also equipped to identify and isolate or average out these effects.

# CHAPTER FIVE

# CONCLUSION

From profiles of the borehole site surveys, resistivity values reported did not show much difference with respect to magnitude, regardless of the direction of traverse. There was also no association of the reported higher resistivity with a preferred direction. There was no observed consistency and trend. The magnitude of resistivity differed across location, and within location differed across depth with respect to traverse direction. The observed differences can be attributed to compositional inhomogeneity or variations in subsurface material composition and texture.

Summarily, the results show that investigations restricted to the 'very' near subsurface using the resistivity method, need not have their traverses oriented across the strike of the local geology (rocks) or the predominant fracture system as per convention. Traverse orientation should rather be constrained and determined by the dimensions (length) and disposition of the feature of interest. This should be, irrespective of the array choice.

The expected resistivity lows were not observed over the borehole position for some sites. This could have resulted from any of the following;

i. Boreholes were not originally sited at positions coinciding with resistivity lows. Other factors such as environmental, safety and developmental concerns could have played a larger role in the siting. In such cases, geophysics is not paramount.

ii. Boreholes were originally sited on resistivity lows. This resistivity lows were not observed because of a very likely difference in investigative depth and traverse bearing during profiling for possible sites, and that of this research. Traverse bearing

would come to play if the depth of original profiling was within the bedrock, and as such resistivity would be affected by anisotropy.

Profiles and images from traverses run across the dumpsite also suggest gradual infiltration of leachate into the 'very' near subsurface. The observed low resistivity zone coincided consistently with the section of the traverse which cut into the active parts of the dumpsite. The generally flat nature of the terrain would inhibit leachate run-off and as such aid downward movement.

Resistivity sections produced from the different arrays imaged the low resistivity zone. However, there were subtle differences in the general resistivity trends observed. Wenner and Schlumberger arrays, showed a high level of consistency in image and profile similarities. The dipole-dipole array profiles were for most part non-conformable with the Wenner and Schlumberger arrays' profiles and sections. All the sections produced showed the main resistivity features with similar general disposition, but with notable differences in the vertical and lateral extents.

Dipole-Dipole array sections showed lateral exaggeration of the imaged features. Schlumberger array sections had the best lateral resolution typified by imaging of pockets of variation in resistivity reflecting the laterally inhomogeneous nature of the upper sections of the dumpsite. The performance of the Wenner and dipole-dipole array in imaging this was not consistent. However, the dipole-dipole array was slightly better than the Wenner array.

The Wenner array section for the most part had the best vertical resolution of subsurface features, followed closely by the dipole-dipole and the Schlumberger arrays. The dipole-dipole and Schlumberger array sections showed better (sharp) resistivity contrast between

features with large differing resistivity. The Wenner and Schlumberger arrays had better images of zones with undefined geometry such as the suspected areas of contamination. Wenner array imaged better the gently grading resistivity boundaries associated with such features.

The Wenner array performed best in imaging the buried salt unit, as observed in the profiles and sections (pseudo- and true resistivity sections). The Schlumberger array section showed a feature whose vertical position coincided with that of the buried salt unit, and its resistivity contrast was that which was anticipated. However, its horizontal position, vertical and lateral extent was not in agreement. It cannot therefore be concluded if the feature was the salt unit. The Schlumberger pseudo-section nonetheless imaged the salt unit distinctly. The dipole-dipole array did not image the salt unit, in both the pseudo- and true resistivity section.

None of the true resistivity sections of the arrays could define the geometry of the salt unit. They were better represented by the pseudo-sections.

## RECOMMENDATION

Suggesting the use of a particular array over the others, in a relatively unknown terrane would defeat the fundamental assumption of this work. Resistivity results from a complex weighted contribution of a number of factors. No two subsurface are the same. It would be good practice therefore to test the performance of the different arrays in a particular terrane during orientation survey. It would be better still, if all of the arrays are used in the main work phase. This has been made easy by the introduction of intelligent automated multi-electrode resistivity imaging systems. In the least, these complementary data would be

confirmative of major features present; and also highlight areas of non-agreement as uncertainties.

# REFERENCES

Agramakova, Y. (2005). Time-Lapse Electrical Resistivity Tomography Applied to Cave Sustainability (Barbados) and Groundwater Exploration (Saint Lucia). (unpublished MSc. Thesis), Moscow State University.

Ahmad, N., Wan Abdullah, W.A.T., Samsudin, T. and Behrang, N. (2010). Comparison of Wenner and Dipole–Dipole arrays in the study of an underground three-dimensional cavity. Journal of Geophysics and Engineering, 7, 30–40.

Akankpo, A. O. and Igboekwe, M. U. (2011). Monitoring Groundwater Contamination Using Surface Electrical Resistivity and Geochemical Methods. Journal of Water Resource and Protection, 3, 318-324. doi:10.4236/jwarp.2011.35040

Alwan, K.I. (2013). Comparison between conventional arrays in 2D electrical resistivity imaging technique for shallow subsurface structure detection of the University of Technology. Eng. &Tech. Journal, 31(10), 1817-1824.

Andy, A.B., Saad, R. and Muztaza, M.M. (2012). Geophysical and Geotechnical Engineering Assessment of Slope Stability and Clayey Sand Soil's Behaviour Analysis. Advances in Biomedical Engineering, 6, 113-118.

Anokwa, Y., Martin, N. and Muff, R. (2005). Coastal Stability Map of Greater Accra Metropolitan Area. Environmental and Engineering Geology Map of Greater Accra Metropolitan Area. Accra, Ghana.

Apostolopoulos, G., Stamataki, S. and Amolochitis, G. (2012). Integrated geophysical investigation prior to excavation in a quarry of Milos Island, Greece. Near Surface Geoscience 2012 – 18th European meeting of environmental and engineering geophysics. Extended abstract P01.

Apostolopoulos, G., Leontarakis, K. and Orfanos, C. (2014). Geophysical investigation of the Temple of Poseidon at Cape Sounio, Attica, Greece. First Break, 32(8), 53-59.

Bauman, P. (2005). 2-D resistivity surveying for hydrocarbons—a primer. CSEG Recorder April 2005, 25–33.

Besson, A., Cousin, I., Samouelian, A., Boizard, H. and Richard, G. (2004). Structural heterogeneity of the soil tilled layer as characterized by 2D electrical resistivity surveying. Soil & Tillage Research, 79(2), 239–249.

Boadu, F.K., Owusu-Nimo, F. (2010). Influence of petrophysical and geotechnical engineering properties on the electrical response of unconsolidated earth materials. Geophysics, 75 (3), G21–G29.

Boadu, F.K., Owusu-Nimo, F. and Menyeh, A. (2008). Nitrate contamination in groundwater at farmlands in Nsawam, Ghana: the role of fractures from azimuthal resistivity surveys. Journal of Environmental and Engineering Geophysics, 13 (1), 27–37.

Butt, A.L. and Flis, M.F. (1997). The application of geophysics to iron ore mining in the Hamersley Basin, Western Australia. Exploration Geophysics, 28 (2), 195–198.

Cardimona, S. (2002). Electrical resistivity techniques for subsurface investigation. Paper presented at the 2nd Annual Conference on the Application of Geophysical and NDT Methodologies to Transportation Facilities and Infrastructure, Los Angeles, Carlifornia. Abstract Retrieved from on February 2, 2015 http://trid.trb.org/view.aspx?id=720488

Chambers, J.E., Wilkinson, P.B., Wardrop, D., Hameed, A., Hill, I., Jeffrey, C., Loke, M.H., Meldrum, P.I., Kuras, O., Cave, M. and Gunn, D.A. (2012). Bedrock detection beneath river terrace deposits using three-dimensional electrical resistivity tomography. Geomorphlogy, 177–178, 17–25. Retrieved on January 2, 2015 http://dx.doi.org/10.1016/j.geomorph.2012.05.034

Dahlin, T. (1996). 2D resistivity surveying for environmental and engineering applications. First Break, 14, 275-283.

Dahlin, T.and Loke, M.H. (1998). Resolution of 2D-Wenner resistivity imaging as assessed by numerical modelling, J. Appl. Geophys., 38, 237–249

Dey, A., Meyer, W.H., Morrison, H.F. and Dolan, W.M. (1975). Electric field response of two dimensional inhomogeneities to unipolar and bipolar electrode configurations, Geophysics, 40, 630–640..

Dickson, K.B., and Benneh, G. (1998). A new geography of Ghana. London, U.K: Longman Group.

Edwards, L.S. (1977). A modified pseudosection for resistivity and induced polarization.Geophysics 42 (5), 1020–1036.

Ehirim, C.N. and Essien, S.S. (2009). Comparative investigation of Offset Wenner, Square and Schlumberger arrays in electrical anisotropy studies. Scientia Africana, 8 (2), 53-60.

Eze, P. N. (2008). Characterization, Classification and Pedogenesis of soils on a Legon catena in the Accra plains, Ghana (Unpublished master's thesis). University of Ghana, Accra.

Ford, K., Keating, P., and Thomas, M.D. (2007). Overview of geophysical signatures associated with Canadian ore deposits, in Goodfellow, W.D., ed., Mineral deposits of Canada—A synthesis of major deposit-types, district metallogeny, the evolution of geological provinces, and exploration methods: Geological Association of Canada, Mineral Deposits Division, Special Publication 5, 939–970.

Guo, W., Dentith, M.C., Xu, J., Ren, F. (1999). Geophysical exploration for gold in Gansu Province, China. Exploration Geophysics, 30(2), 76–82.

Hallof, P. G. (1957). On the interpretation of resistivity and induced polarization measurements (Unpublished doctoral thesis). Massachusetts Institute of Technology, Cambridge.

Herman, R. (2001). An introduction to electrical resistivity in geophysics. American Journal of Physics, 69(9), 943-952. doi: 10.1119/1.1378013.

Jones, F. (2007). DC Resistivity surveys. Retrieved on February 3, 2015 from UBC Earth and Ocean Sciences website, http://eos.ubc.ca/../Seeing.pdf

Keller, G. V., and Frischknecht, F.C. (1966). Electrical methods in geophysical prospecting, Pergamon Press. Inc.

Kelly, B.F.J., Acworth, R.I. and Greve, A.K. (2011). Better placement of soil moisture point measurements guided by 2D resistivity tomography for improved irrigation scheduling. Soil Research, 49(6), 504–512.

Kese, G.O. (1985). Rock and Mineral Resources of Ghana. A.A. Balkema, Boston.

Koefoed, O. (1979). Geosounding principles 1: Resistivity sounding measurements. Amsterdam: Elsevier Science.

Loke, M. H., & Barker, R. D. (1996) .Practical Technique for 3D Resistivity Surveys and Data Inversion. Geophysical Prospecting, 44, 499-523.

Loke, M.H. (2000). Electrical imaging surveys for environmental and engineering studies: A practical guide to 2-D and 3-D surveys. Retrieved on March 9, 2015 from http://www.georentals.co.uk/Lokenote.pdf

Loke, M. H. (2010). Tutorial: 2-D and 3-D Electrical Imaging Surveys. Retrieved on March 9, 2015 from http://www.geoelectrical.com

Loke, M.H., Chambers, J.E., Rucker, D.F., Kuras O. and Wilkinson, P.B. (2013). Recent developments in the direct-current geoelectrical imaging method. Journal of Applied Geophysics, 95, 135–156.

Magnusson, M., Fernlund, J. and Dahlin, T. (2010). Geoelectrical imaging for interpretation of geological conditions affecting quarry operations. Bulletin of Engineering Geology and the Environment, 69(3), 465–486.

Mastrocicco, M., Vignoli, G., Colombani, N. and Zeid, N.A. (2010). Surface electrical resistivity tomography and hydrogeological characterization to constrain groundwater flow modeling in an agricultural field site near Ferrara (Italy). Environmental Earth Sciences 61 (2), 311–322.

Mota, R., Monteiro, S.F.A., Mateus, A., Marques, F.O., Conclaves, A., Figueiras, J. and Amaral, H. (2004). Granite fracturing and incipient pollution beneath a recent landfill facility as detected by geoelectrical surveys. J. Appl. Geophys., 57(1), 11-22.

Morgan, L.A. (2012). Geophysical characteristics of volcanogenic massive sulfide deposits in volcanogenic massive sulfide occurrence model. U.S. Geological Survey Scientific Investigations Report 2010–5070 –C, chap. 7, 16 p.

Muhammad A., Aamir S., Ijaz A. and Matloob, A. (2013). Hydraulic transmissivity determination for the groundwater exploration using vertical electric sounding method in comparison to the traditional methods. Pak. J. Agri. Sci., 50(3), 487-492.

Muskat, M. and Evinger, H. H. (1941). Current penetration in direct current prospecting. Geophysics, 6, 397–427.

Nijland, W., van der Meijde, M., Addink, E.A. and de Jong, S.M. (2010). Detection of soil moisture and vegetation water abstraction in a Mediterranean natural area using electrical resistivity tomography. Catena, 81(3), 209–216.

Oborie, E and Udom, G.J. (2014). Determination of aquifer transmissivity using geoelectrical sounding and pumping test in parts of Bayelsa State, Nigeria. Peak Journal of Physical and Environmental Science Research, 2 (2), 32-40.

Oldenburg, D.W. and Li, Y. (1999). Estimating the depth of investigation in dc resistivity and IP surveys, Geophysics, 64, 403–4.

Opkoli, C.C. (2013). Sensitivity and Resolution Capacity of Electrode Configurations. International Journal of Geophysics, 13, 1-12. http://dx.doi.org/10.1155/2013/608037.

Papadopoulos, N.G., Sarris, A., Salvi, M.C., Dederix, S., Soupios, P. and Dikmen, U. (2012). Rediscovering the small theatre and amphitheatre of ancient Leraptyna (SE Crete) by integrated geophysical methods. Journal of Archaeological Science, 39, 1960-1973.

Papadopoulou, M.P. Karatzas , G.P., Koukadaki, M.A. and Trichakis, Y. (2005). Modeling the saltwater intrusion phenomenon in coastal aquifers - A case study in the industrial zone of Herakleio in Crete. Global NEST Journal, 7(2), 197-203.

Park, J., You, Y.J. and Kim, H.J. (2009). Electrical resistivity surveys for gold-bearing veins in the Yongjang mine, Korea. Journal of Geophysics and Engineering, 6, 73-81.

Perren, L. J. (2005). Investigating the Performance of electrical resistivity arrays (Unpublished master's thesis). Virginia Polytechnic Institute and State University, Blacksburg, Virginia.

Reynolds, J.M. (2011). An Introduction to Applied and Environmental Geophysics (2nd Ed). John Wiley & Sons, England.

Rossi, R., Amato, M., Bitella, G., Bochicchio, R., Gomes, J.J.F., Lovelli, S., Martorella, E. and Favale, P. (2011). Electrical resistivity tomography as a non-destructive method for mapping root biomass in an orchard. European Journal of Soil Science, 62(2), 206 215.

Roy, A. (1972). Depth of investigation in Wenner, three-electrode and dipole-dipole DC resistivity methods. Geophys. Prospect., 20, 329–340.

Roy, A. and Apparao, A. (1971). Depth of investigation in direct current methods. Geophysics, 36, 943-959.

Satriani, A., Loperte, A. and Proto, M. (2011). Electrical resistivity tomography for coastal saltwater intrusion characterization along the Ionian coast of Basilicata region (southern Italy). Paper presented at Fifteenth International Water Technology Conference, IWTC-15 2011, Alexandria, Egypt.

Samouelian, A., Cousin, I., Tabbagh, A., Bruand, A. and Richard, G. (2005). Electrical resistivity survey in soil science: A review. Soil and Tillage Research, 83(2), 173-193. Retrieved from http://www.doi.org/10.1016/j.still.2004.10.004

Sauck, W.A., and Zabik (1992). Azimuthal resistivity techniques and the directional variations of hydraulic conductivity in glacial sediments. Symposium on the application of geophysics and environmental problems: Soc. Eng. Min. Expl. Geophys.,197-222.

Seaton, W.J. and Burbey, T.J. (2002). Evaluation of two-dimensional resistivity methods in a fractured crystalline-rock terrain. Journal of Applied Geophysics, 51, 21- 41.

Selley, R.C., Cocks, L.R.M. and Plimer, I.R. (Eds). (2005). Encyclopedia of Geology. Oxford, U.K: Elsevier.

Slater, L., Binley, A., Versteeg, R., Cassiani, G., Birken, R. and Sandberg, S. (2002). A 3D ERT study of solute transport in a large experimental tank. Journal of Applied Geophysics, 49 (4), 211–229.

Soupios, P., Papadopoulos, N., Papadopoulos, I., Kouli, M., Vallianatos, F., Sarris, A. and Manios, T. (2007). Application of integrated methods in mapping waste disposal areas. Environmental Geology, 53 (3), 661–675.

Spitzer, K. (1998). The three-dimensional dc sensitivity for surface and subsurface sources, Geophys. J. Int., 134, 736–764.

Stummer, P. (2003). New development in electrical resistivity imaging (Unpublished doctoral dissertation). Swiss Federal Institute of Technology, Zurich, Switzerland.

Sumner, J.S. (1976). Principles of induced polarization for geophysical exploration: Elsevier Publishing company.

Szalai, S. and Szarka, L. (2008). On the classification of surface geoelectric arrays. Geophysical Prospecting, 56 (2), 159–175.

Tabbagh, A., Dabas, M., Hesse, A. and Panissod, C. (2000). Soil resistivity: a non-invasive tool to map soil structure horizonation. Geoderma, 97, 393–404.

Tamssar, A.H. (2013). An evaluation of the suitability of different electrode arrays for geohydrological studies in karoo rocks using electrical resistivity tomography (Unpublished master's thesis). University of Free State, South Africa.

Telford, W.M., Geldart, L.P., and Sheriff, R.E. (1990). Applied Geophysics, 522-577. Cambridge, UK: Cambridge University Press.

Tsourlos, P., Vargemezis, G.N., Fikos, I., Tsokas, G.N. (2014). DC geoelectrical methods applied to landfill investigation: case studies from Greece. First Break, 32(8), 81-89.

van Nostrand, R.G. (1953). Limitations on resistivity methods as inferred from the buried sphere problem, Geophysics, 18, 423–433.

Ward, S. H. (1990). Resistivity and IP Methods in Geotechnical and Environmental Geophysics, 1. Society of Exploration Geophysicists, Investigations in Geophysics.

Watson K.A. and Barker, R.D. (1999). Differentiating anisotropy and lateral effects using azimuthal resistivity offset Wenner soundings. Geophysics, 64(3), 739-745.

# APPENDIX A

Coordinates of survey stations and bearing of Traverses

| STATION | LONG (W) | LAT (N) | BEARING | |
|---|---|---|---|---|
| | | | A | B |
| REN 01 | 0°11'17.3723" | 5 °39'53.8987" | 038 | 308 |
| REN 02 | 0 °10'59.1028" | 5 °39'38.0662" | 040 | 315 |
| REN 03 | 0 °11'36.0861" | 5 °39'4.6762" | 035 | 305 |
| REN 04 | 0 °11'31.8855" | 5 °39'0.3946" | 040 | 310 |
| REN 05 | 0 °11'15.5873" | 5 °38'39.7903" | 030 | 300 |
| REN 06 | 0 °11'12.2989" | 5 °38'28.1617" | 030 | 300 |
| REN 07 | 0 °11'6.1061" | 5°38'19.5768" | 030 | 300 |
| REN 08 | 0 °11'5.7182" | 5 °38'19.2171" | 038 | 310 |
| REN 09 | 0 °11'12.7355" | 5 °38'18.4378" | 030 | 300 |
| REN 10 | 0 °11'11.2061" | 5 °38'19.1135" | 030 | 300 |
| REN 11 | 0 °11'5.2527" | 5 °39'8.5604" | 030 | 300 |
| REN 12 | 0 °11'20.4319" | 5 °38'18.2148" | 040 | 310 |
| REN 13 | 0 °11'8.4183" | 5 °38'18.1567" | 030 | 300 |
| REN 14 | 0 °11'18.8643" | 5 °39'7.2276" | 040 | 310 |
| REN 15 | 0 °11'26.6936" | 5 °39'13.1532" | 030 | 300 |
| DUMPSITE | 0 °11'7.368" | 5 °38'7.2564" | 026 | 300 |

# APPENDIX B

Anisotropy coefficients (λ) the for various arrays across the borehole positions

| STATION | WENNER ARRAY | | | SCHLUMBERGER ARRAY | | | DIPOLE-DIPOLE ARRAY | | |
|---|---|---|---|---|---|---|---|---|---|
| | λ (D1) | λ (D2) | λ (D3) | λ (D1) | λ (D2) | λ (D3) | λ (D1) | λ (D2) | λ (D3) |
| REN 01 | 1.13 | 1.17 | 1.34 | 0.67 | 1.00 | 1.03 | 0.66 | 1.82 | 1.15 |
| REN 02 | 1.27 | 1.27 | 1.25 | 1.10 | 1.07 | 1.04 | 1.22 | 0.49 | 1.19 |
| REN 03 | 1.29 | 0.79 | 0.99 | 1.16 | 0.94 | 1.08 | 0.36 | 0.65 | 0.53 |
| REN 04 | 1.05 | 1.14 | 1.05 | 1.24 | 1.33 | 1.09 | 1.04 | 1.65 | 1.10 |
| REN 05 | 1.11 | 1.48 | 1.01 | 1.02 | 1.13 | 1.08 | 0.99 | 1.07 | 1.05 |
| REN 06 | 0.82 | 0.85 | 0.77 | 0.99 | 0.99 | 0.83 | 1.01 | 1.41 | 1.13 |
| REN 07 | 1.15 | 1.10 | 1.00 | 1.10 | 1.14 | 1.20 | 1.13 | 1.59 | 1.22 |
| REN 08 | 2.21 | 2.29 | 1.78 | 1.10 | 0.99 | 0.98 | 1.01 | 0.82 | 0.99 |
| REN 09 | 0.86 | 0.93 | 1.03 | 1.00 | 0.89 | 0.83 | 1.02 | 1.23 | 1.04 |
| REN 10 | 0.96 | 0.99 | 1.03 | 0.99 | 0.90 | 0.84 | 1.65 | 0.84 | 0.74 |
| REN 11 | 1.53 | 1.22 | 1.03 | 1.15 | 1.46 | 1.11 | 1.11 | 0.61 | 0.72 |
| REN 12 | 0.96 | 0.99 | 1.05 | 1.00 | 1.24 | 1.21 | 0.97 | 0.90 | 0.91 |
| REN 13 | 0.83 | 0.70 | 1.19 | 0.76 | 0.88 | 0.99 | 0.74 | 1.16 | 0.81 |
| REN 14 | 1.28 | 1.26 | 1.53 | 0.21 | 0.68 | 0.20 | 0.92 | 1.05 | 0.99 |
| REN 15 | 1.20 | 1.22 | 1.23 | 1.20 | 1.40 | 0.87 | 1.22 | 0.98 | 1.03 |